EUROPEAN ORGANIZATION FOR NUCLEAR RESEARCH (CERN)

CERN-SHiP-NOTE-2015-006
SHiP-TP-2015-A4
9 April 2015

Conceptual design of the SHiP Target and Target Complex

M. Calviani, M. Battistin, R. Betemps, J.-L. Grenard, D. Horvath, P. Pacholek, A. Perez, A. Perillo Marcone, A. Rakai, R. Rinaldesi, S. Sgobba, C. Strabel, V. Venturi, H. Vincke
CERN

Abstract

This document describes the conceptual design of the SHiP facility production target and of the associated target complex.

HISTORY OF CHANGES

REV. NO.	DATE	PAGES	DESCRIPTIONS OF THE CHANGES
0.1	2015-02-27	88	Final draft version including all contributions
0.2	2015-03-03	91	Further comments and revision included
0.3	2015-03-05	92	Manpower and cost estimate update and minor modifications
0.4	2015-03-10	93	English revision
0.5	2015-03-13	93	Version for approval, final reference modification
0.6	2015-03-13	93	Version under approval and circulated to checkers and appr.
1.0	2015-04-09	94	Final released version

TABLE OF CONTENTS

1. Design of the SHiP target

1.1 Introduction

The chapter will present the conceptual design of the Search for Hidden Particles (SHiP) [1] production target. It describes the general considerations associated to its design, including experimental requirements, beam parameters and dilution as well as the configuration, material and sizes of the target plates.

A description of the conceptual design of the target assembly will then be presented, starting from detailed energy deposition maps, radiation damage, gas production, thermo-mechanical analysis of the assembly taking into account baseline and accident conditions and a fluid-dynamics evaluation of the cooling circuit.

In the last part, we discuss the material challenges faced by the design, with a review of compressive and tensile stresses, thermal fatigue, corrosion resistance considerations as well as evolution of the material properties as a function of radiation damage as compared to the available literature data.

1.2 Target design optimisation

1.2.1 Target and beam parameters

The SHiP production target is one of the most challenging aspects of the proposed installation, due to the very high energy and power density that will be reached during operation. The target is effectively to be considered as a beam dump, as it will contain most of the cascade generated by the primary beam interaction.

In terms of average beam power delivered on target during the spill, the installation will be in a similar operational regime as of the Spallation Neutron Source at ORNL (US) or to the Material Life Sciences spallation source at J-PARC (Japan), despite both of them operating with a liquid mercury target.

Contrary to other spallation sources, where for most of the cases the beam is CW, the SPS operational parameters dictate an extremely high pulse intensity, followed by a cooling down of several seconds (see Table 1). In the SHiP case, the cycle-averaged beam power delivered on target is around 355 kW. However, when averaged over the pulse duration of 1 second, this power increases up to 2.56 MW (see Table 1).

Table 1: The table shows the SPS beam parameters considered for the evaluation of the target design [2].

	Baseline characteristics
Proton momentum [GeV/c]	400
Beam intensity [10^{13} p/cycle]	4.0
Cycle length [s]	7.2

Spill duration [s]	1.0
Expected r.m.s. spot size (H/V) [mm]	6/6
Sweep radius (min/max) [mm]	6/35
Average beam power on target [kW]	355
Average beam power on target during spill [kW]	2560

1.2.2 Production target material choice

For the SHiP target case, we have proposed a hybrid solution composed of (solid) molybdenum alloy and pure tungsten, for a total target length of 116 cm. The material selection is based on the requirement of having a high-Z material with a short interaction length, in order to increase as much as possible the reabsorption of pions and kaons produced in the spallation process that would otherwise generate a background for the experiment.

The core plates are 30x30 cm^2 in transverse size, with a variable length according to the longitudinal direction. The first 58 cm – divided in 13 layers – are made out of TZM ((0.08%)titanium-(0.50%)zirconium-molybdenum alloy) for a total nuclear inelastic scattering length (λ) of 4λ, while the remaining 58 cm are composed by 4 blocks of pure tungsten (yielding 6λ), for a total of almost 10λ. TZM is chosen as it is stronger than pure molybdenum and possesses a higher recrystallization temperature and better creep resistance than pure molybdenum; it is especially suited for high-temperature applications, involving demanding mechanical loads. Pure W is on the contrary selected for the second half of the target due to its superior performances with irradiation as compared to alloys such as Inermet or Densimet. Due to the high energy deposition (see section 1.2.4.1) and due to the high temperature reached during steady state operation (see section 1.2.5), the target will have to be actively cooled.

A comparison of the beam characteristics of SHiP with respect to facilities constructed in the past for a similar physics case at CERN (CHARM) or at Fermilab (DONUT) are reported in Figure 1. For both CHARM and DONUT the significant lower super-cycle averaged power on target is evident with respect to what it is proposed for SHiP. In addition, the expected POT on target for SHiP is between 2 and 3 orders of magnitude larger than for past experiments, entering into a running regime where significant variations of material mechanical properties with irradiation will be expected during the operation of the target. Contrary to DONUT and SHiP, CHARM operated with a fast extracted beam: as reported in [3] this generated problems with water cooling circuit due to pressure waves generated inside the CHARM copper target.

	DONUT [1)]	CHARM [2)]	SHiP
Target material	W-alloy	Cu (variable ρ)	TZM + pure W
Momentum (GeV/c)	800	400	400
Intensity	$0.8*10^{13}$	$1.3*10^{13}$	**$4*10^{13}$**
Pulse length (s)	20	$23*10^{-6}$	1
Rep. rate (s)	60	~10	7.2
Beam energy (kJ)	1020	830	2560
Avg. beam power (spill) (kW)	51	$3.4*10^{7}$ (fast)	2560
Avg. beam power (SC) (kW)	17	69	355
POT	Few 10^{17}	Few 10^{18}	**$2*10^{20}$**

Figure 1: The table shows a comparison of the beam parameters for old experiments such as DONUT (* http://www-donut.fnal.gov/) and CHARM (** http://cds.cern.ch/record/205527/files/CM-P00068733.pdf?version=1) as compared to SHiP.

1.2.3 Beam dilution on target

For the evaluation of the response of the target, as proposed by B. Goddard in Ref. [4] the beam extracted from the SPS is assumed to have a momentum of 400 GeV/c, with a 1σ of 6 mm Gaussian shape. The beam is then diluted through an Archimedean spiral, with a starting radius of 5 mm and a 6 mm increment in the radius per each turn. The maximum radius is 35 mm, for a total of 5 turns in 1000 ms and constant sweep speed in mm/ms [5]. The dilution shape is represented in Figure 2.

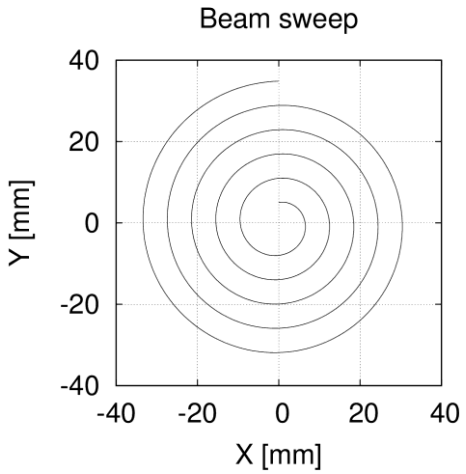

Figure 2: The figure shows the assumed beam sweep footprint at the longitudinal position corresponding to the SHiP target [5].

1.2.4 FLUKA simulations – energy deposition and radiation damage

FLUKA Monte Carlo simulations [6] [7] have been performed in order to evaluate the energy deposited on the target blocks as well as in the shielding around the target.

The proposed targets core is built out 30 x 30 cm^2 rectangular blocks, with variable thicknesses, made of TZM[1] and pure W[2]. The block thicknesses have been iteratively adjusted to have the most uniform possible energy deposition in each of the blocks. Table 2 summarizes the target core material and the blocks longitudinal thickness.

Table 2: The table summarizes the target core material and the blocks longitudinal thickness. Their transverse size is 30 x 30 cm^2.

Layer	Material	Thickness	Layer	Material	Thickness
1.	TZM	8 cm	10.	TZM	5 cm
2.	TZM	2.5 cm	11.	TZM	6.5 cm
3.	TZM	2.5 cm	12.	TZM	8 cm
4.	TZM	2.5 cm	13.	TZM	8 cm
5.	TZM	2.5 cm	14.	W	5 cm
6.	TZM	2.5 cm	15.	W	8 cm
7.	TZM	2.5 cm	16.	W	10 cm
8.	TZM	2.5 cm	17.	W	35 cm
9.	TZM	5 cm			

The blocks are separated by a 5 mm gap, in which water flows to cool the target plates (see section 1.2.5). The blocks are enclosed in a stainless steel container, with 2 cm thick walls.

A dedicated FLUKA source routine has been developed in order to reproduce the beam dilution sweep shape assumed in Figure 2. At the same time, FLUKA simulations have been performed also assuming a single pulse of 6 mm 1 sigma Gaussian shape, in order to evaluate accident scenarios as well as to dynamically reproduce the thermomechanical behaviour of the beam sweep (see 1.2.5 and reference therein). The special "beam dilution" routine has been used to evaluate aspects including energy distribution, radiation damage and gas production. Due to the beam sigma being equal to the increment at each turn, the transversal energy distribution does not clearly show

[1] The chemical composition of TZM is the following (in weight%): Mo (99.273%), Ti (0.55%), Zr (0.12%), C (0.03%), Si (0.01%), O (0.003%), Ni (0.002%), N (0.002%), Fe (0.01%), with a density of 10.22 g/cm^3.

[2] The assumed density of pure W is assumed to be 19.3 g/cm^3.

the beam sweep as in Figure 2. Figure 3 shows that the energy deposition is essentially constant from the centre spot up to approximately 2.5 cm in radius.

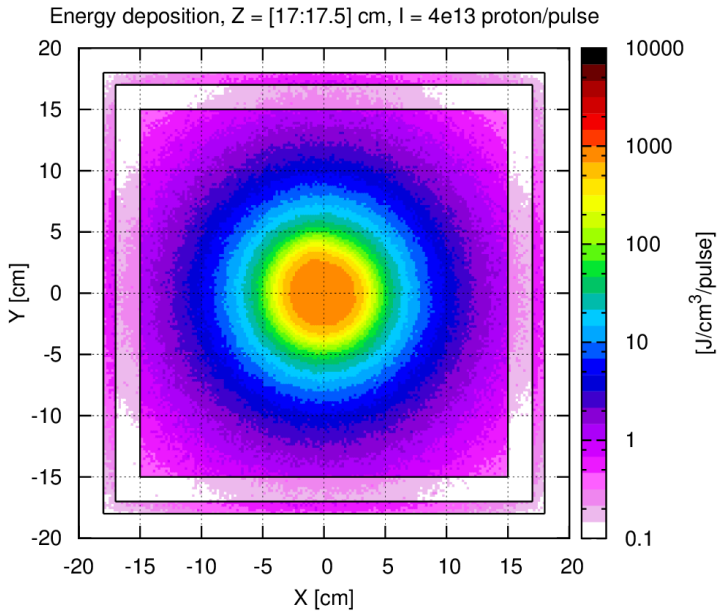

Figure 3: The figure shows the energy deposition averaged between a longitudinal (Z) depth of 17.0 and 17.5 cm (i.e. in the TZM core).

1.2.4.1 Energy deposition

Figure 4 shows the energy density along the Z direction but averaged around the beam centre, assuming the baseline intensity of $4*10^{13}$ p/pulse. The transition point between TZM and pure W is evident (i.e. a peak in the energy density due to the higher density for tungsten with respect to TZM) occurring at a longitudinal position of roughly 65 cm.

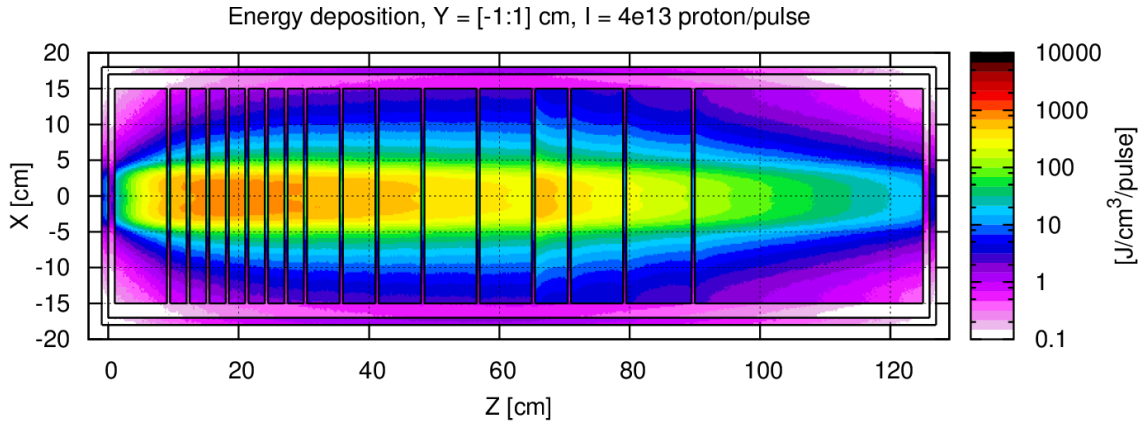

Figure 4: The figure shows the energy density along the Z direction but averaged along the horizontal direction 2 cm around the beam centre.

Similarly, Figure 5 shows the maximum deposition in the longitudinal direction. The peak value is approximately 844 J/cm^3/pulse, occurring at the level of the 4th TZM block. The peak value at the first W block (~5 cm thick) corresponds to ~600 J/cm^3/pulse.

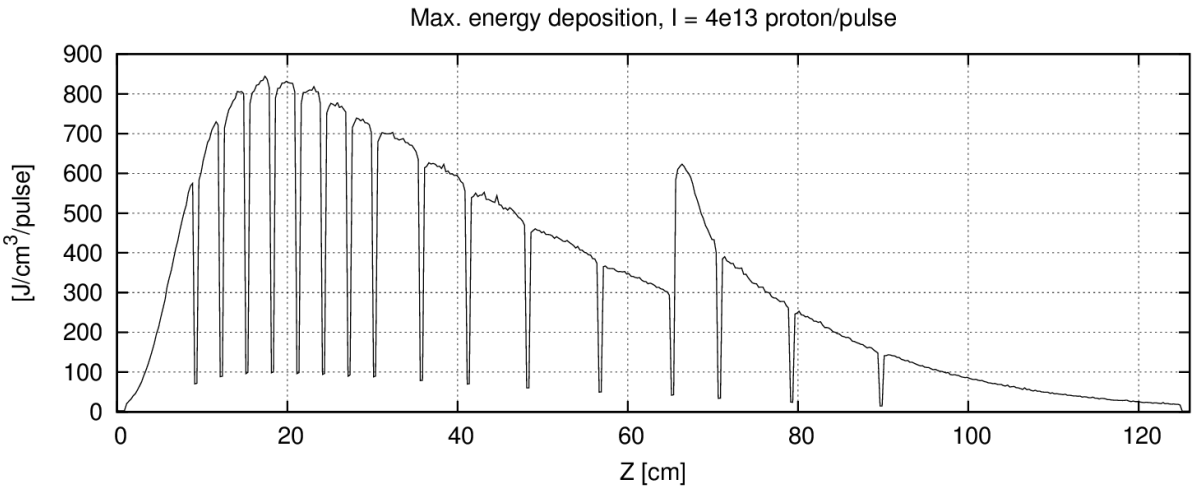

Figure 5: Maximum energy deposition (in J/cm^3/pulse) in the longitudinal direction.

Figure 6 indicates the total energy deposited per target block as a function of the plate number. The maximum-deposited energy for the TZM part is 95 kJ/pulse (5th TZM block), while the maximum value is roughly 200 kJ/pulse (12th TZM block, 8 cm thick). A transition point appears at the 9th TZM plate, due to the thickness increase from 2.5 cm to 5 cm. The total energy deposited in the whole target plates is 2.2 MJ/pulse, corresponding to 85% of the primary beam energy (~2.56 MJ).

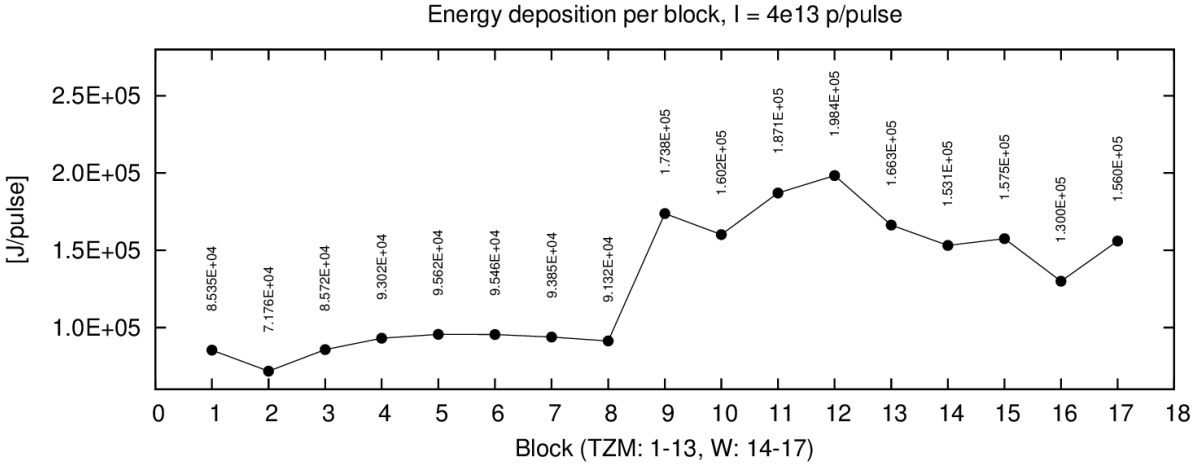

Figure 6: The figure schematically represents the total energy deposited in each target plates.

1.2.4.2 Radiation damage considerations

Due to the very high number of protons expected during the lifetime of the SHiP target (2*10^{20} POT), we expect a significant variation of the target core material mechanical properties. In order to guide these estimations, the FLUKA Monte Carlo code has been employed to evaluate the Displacement per Atom (DPA) as well as the hydrogen and helium gas production. The latter contribute to the swelling of the target material and therefore in the embrittlement of the material properties. The damage energy threshold

(i.e. energy required to permanently displace an atom) for TZM has been assumed equal to the one for pure molybdenum (i.e. 60 eV), while 90 eV have been assumed for pure tungsten.

Figure 7 shows the DPA distribution along the longitudinal direction at the end of the irradiation period corresponding to $2*10^{20}$ POT. Most of the damage (>0.5 DPA) is concentrated around the beam line in a volume of roughly 1000 cm^3. Significant bulk damage is therefore to be expected in this area, with yield strength change, possible cracks formation, embrittlement, etc.

Figure 8 summarizes the maximum DPA to be expected along the longitudinal direction for $2*10^{20}$ POT. The maximum value is around 0.9 DPA, located in the TZM section of the SHiP target. Please note that if the beam would not have been diluted the reached DPA would have been significantly larger.

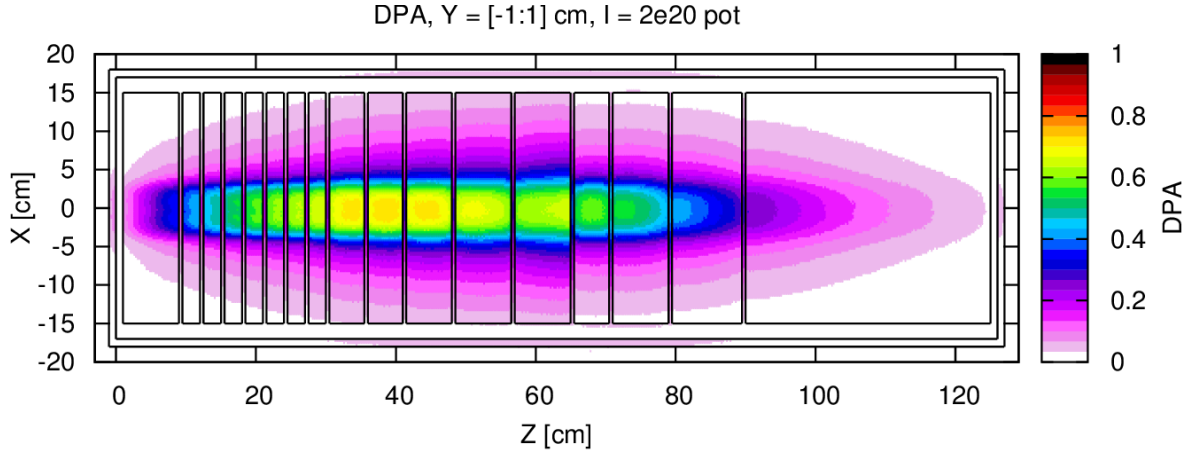

Figure 7: The figure shows the DPA distribution along the longitudinal (Z) direction, averaged around the beam centre (±1 cm).

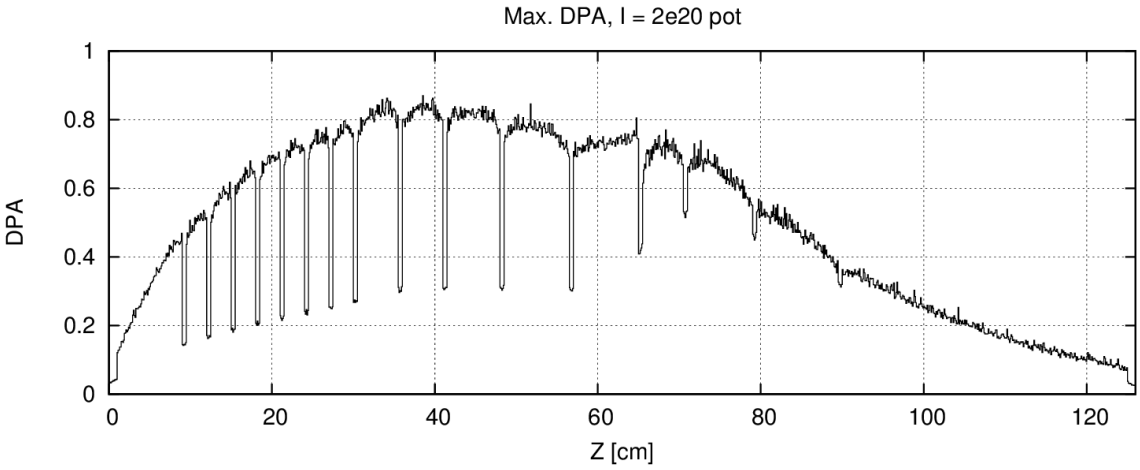

Figure 8: The figure shows the maximum DPA along the longitudinal (Z) direction.

Considering the fact that high-Z materials are employed, coupled with relatively high POTs and high primary beam energies, it is also important to have an idea of hydrogen and helium production in the metals employed as target material. Even at relatively low

concentrations, gas particles can have severe life-limiting consequences for materials: this is particularly true for helium gas since – due to its low solubility in the crystal lattice – it forms clusters and accumulates defects, dislocations and grain boundaries, possibly leading to swelling and/or grain-boundary embrittlement.

The values corresponding to the expected lifetime of the experiment ($2*10^{20}$ POT) are shown in Figure 9 and Figure 10. Neglecting any gas migration, a maximum of ~430 appm of H and ~150 appm of He gas are expected in the central core of the plates, corresponding to a volume roughly representing the maximum radial width of the diluted beam (i.e. within a radius of 35 mm). We note that – as expected – the yield of hydrogen gas is up to 3 times higher than the helium gas.

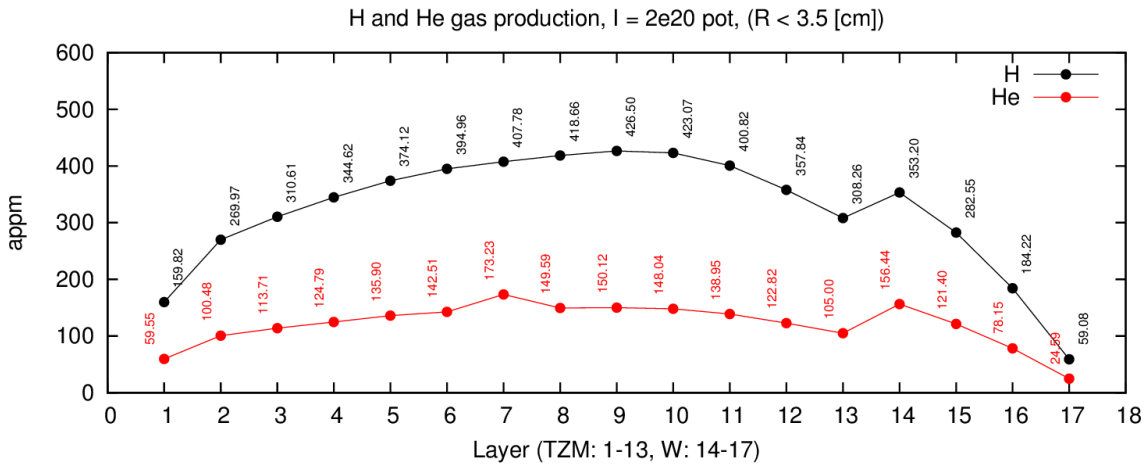

Figure 9: Yield of hydrogen (black dots) and helium (red dots) produced inside the target plates as a function of the blocks number. Results are reported in appm (atomic parts per million) averaged over the volume of the target plates corresponding to the maximum radius of the diluted beam.

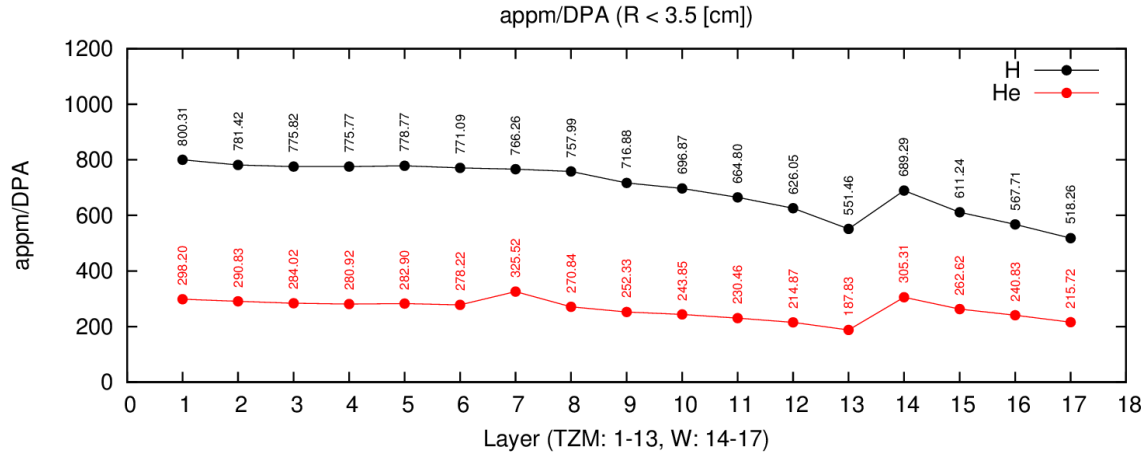

Figure 10: The figure shows the ratio between hydrogen and helium yield and the averaged displacement per atom in the target plates as a function of the blocks, evaluated over a volume corresponding to the maximum radius of the diluted beam.

Ref. [8] reports conservative estimates for critical helium gas densities that could lead to grain-boundary destabilisation giving rise to helium embrittlement. The reported value for (pure) molybdenum (753.2 appm) is well within the limits that we would reach in the SHiP target; a more critical situation is expected for pure tungsten, for which the quoted value in [8] (87.2 appm) is significantly higher than the value expected in the last four pure W plates of the SHiP target. Further R&D activities would be required to understand the impact of these values.

As some of the sources reporting mechanical data variations as a function of radiation are reporting results as a function of total proton and neutron fluence, we have also evaluated the proton and neutron (total and E_n>100 keV) fluence during the target lifetime. Proton fluences reach up to 3.5*10^{19} p/cm^2 (Figure 11 and Figure 12), while high-energy neutrons (above 100 keV) reach up to 1.5*10^{21} n/cm^2 in the central part of the core (Figure 13, Figure 14 and Figure 15).

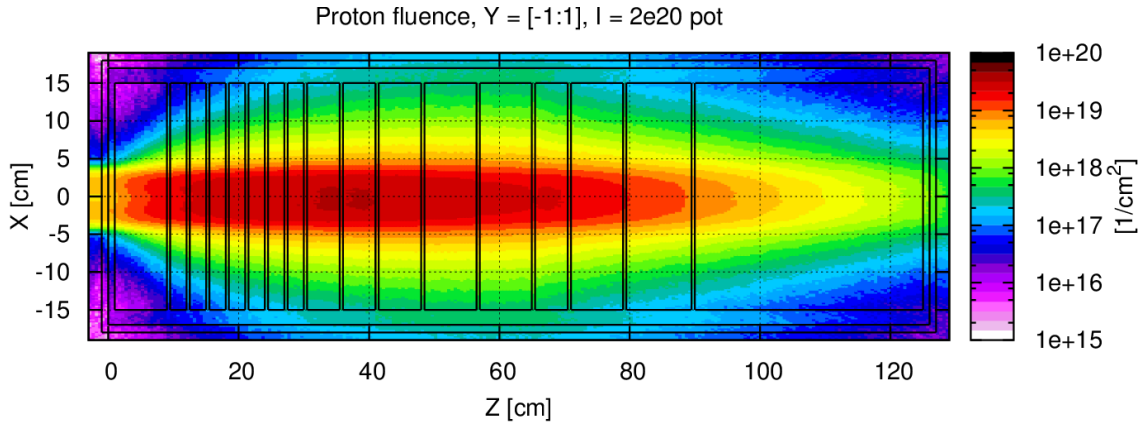

Figure 11: The figure shows the proton density (p/cm^2) along the longitudinal direction averaged around the beam axis (±1 cm).

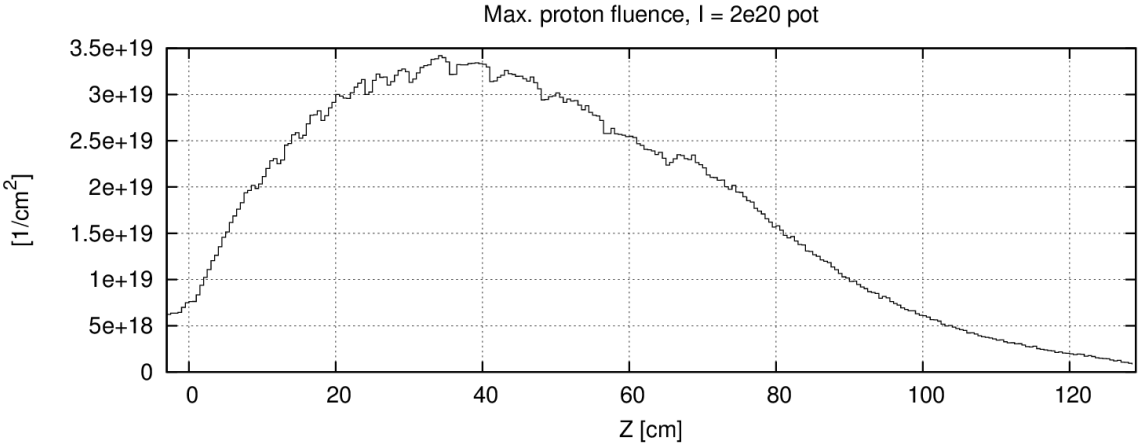

Figure 12: The figure shows the maximum proton density (p/cm^2) along the longitudinal direction.

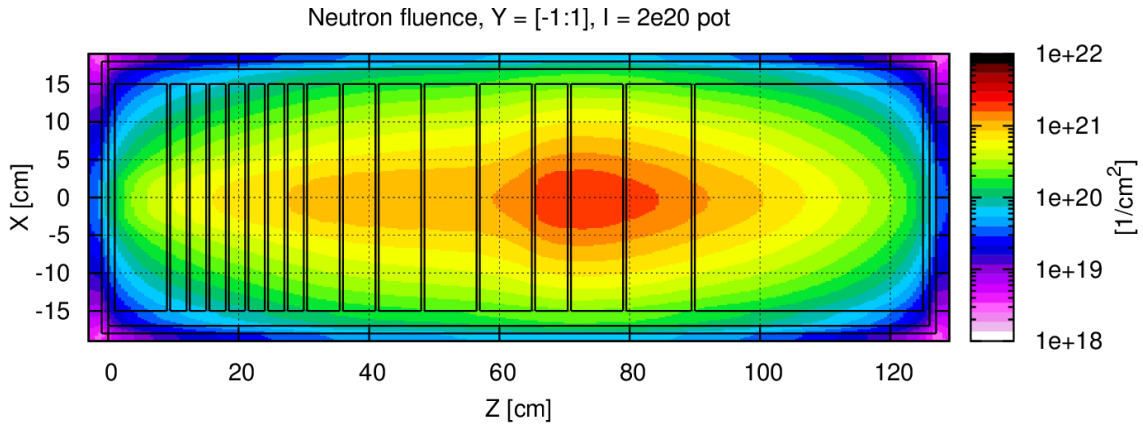

Figure 13: The figure shows the total neutron density (integrated over all energies) (n/cm^2) along the longitudinal direction averaged around the beam axis (±1 cm).

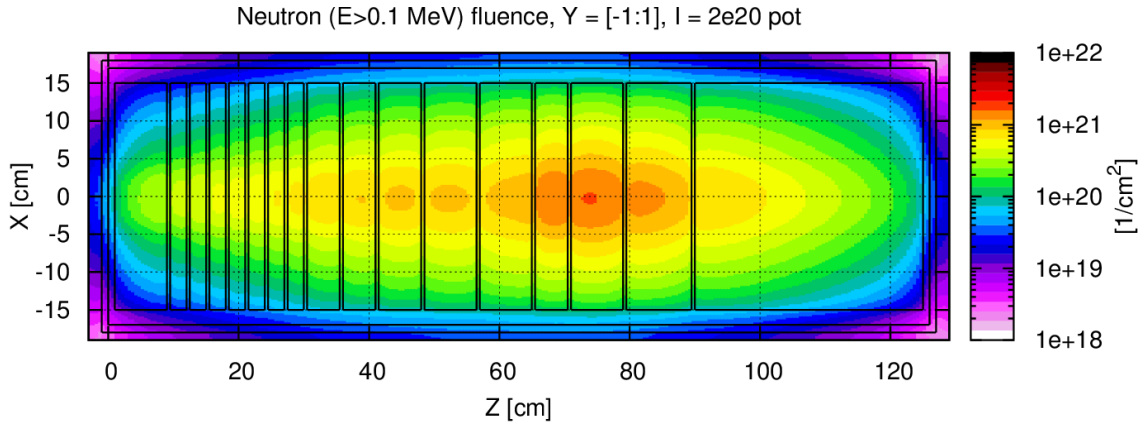

Figure 14: The figure shows the neutron density (neutrons above 100 keV) (n/cm^2) along the longitudinal direction averaged around the beam axis (±1 cm).

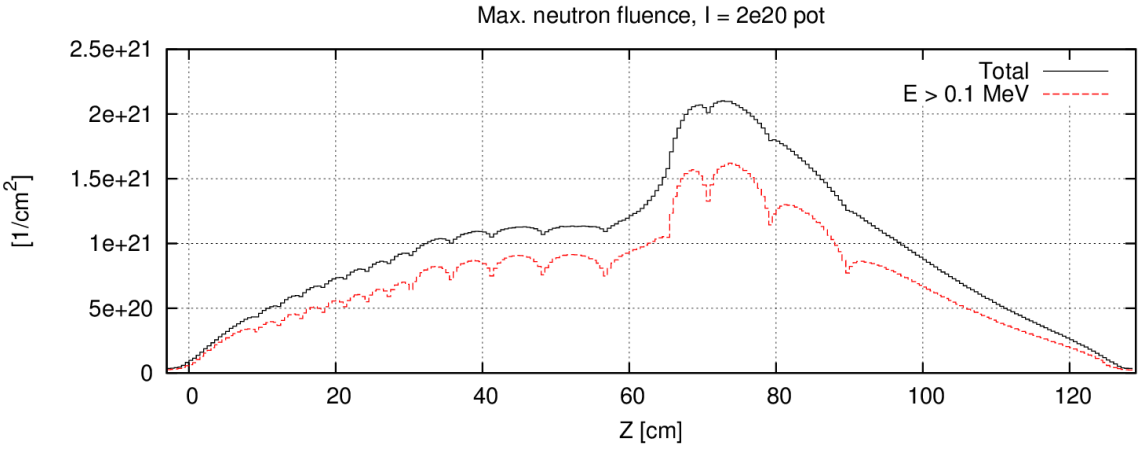

Figure 15: The figure shows the maximum neutron density (n/cm2) along the longitudinal direction, integrated over all energies (black line) and for neutrons above 100 keV (red dashed line).

1.2.4.3 Dose around the SHiP production target

An estimation of the cumulative dose expected in the surroundings of the SHiP spallation target over the whole expected lifetime is presented in Figure 16 and Figure 17. The knowledge of this quantity is important – for instance – to determine the radiation hardness of the target and proximity shielding water-cooling plugin system (see Section 1.3) as well as to foresee the possibility to install a passive material irradiation slot on the side of the spallation target.

Assuming an experiment duration of 5 years, the yearly dose at roughly 10 cm around the target is expected to be in the order of 400 MGy/y.

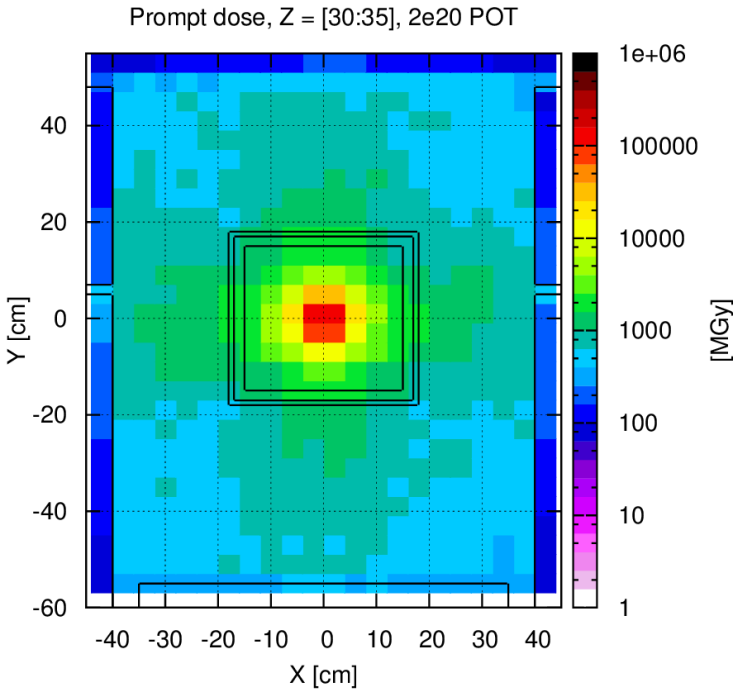

Figure 16: The figure shows the cumulated dose – as a transversal cut averaged between 30 and 35 cm in the longitudinal direction - around the SHiP production target for the whole lifetime of the experiment corresponding to $2*10^{20}$ POT.

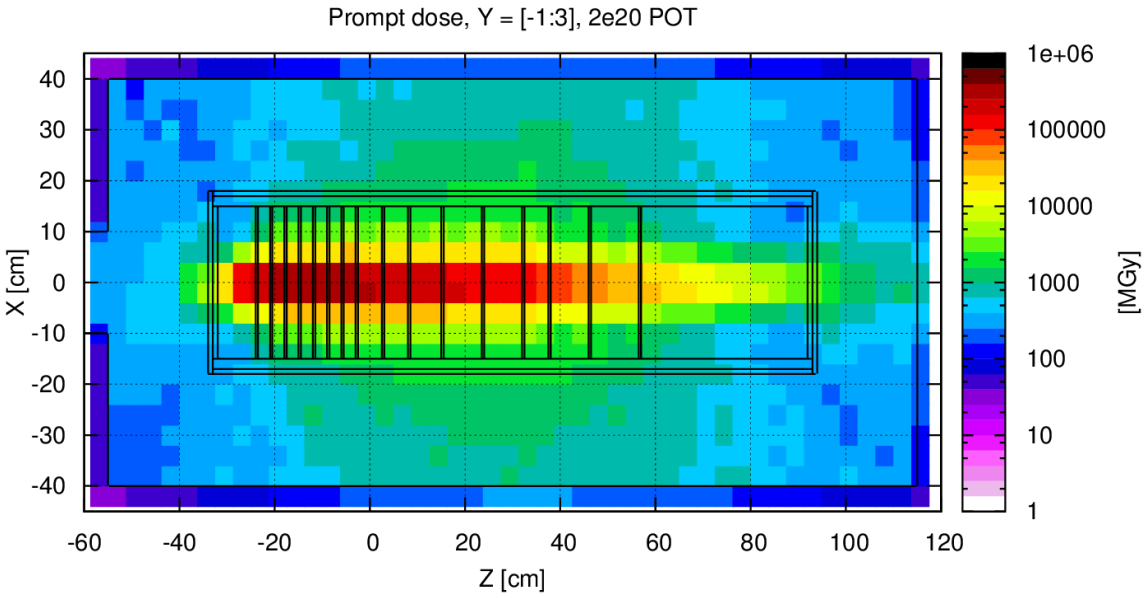

Figure 17: The figure shows the cumulated dose – as a vertical cut averaged around the centre beam line – around the SHiP production target for the whole lifetime of the experiment corresponding to $2*10^{20}$ POT.

1.2.5 SHiP target thermo-mechanical simulations

Being the target subjected to an extreme high-energy deposition per pulse, the necessity of "painting" the beam during the slow extraction arose from the first temperature estimations and a sweep with an Archimedean spiral – as described in 1.2.3 – was simulated in the design process.

Splitting the target into various slices with the objective of increasing the exchange surfaces was also needed to keep core temperature at acceptable levels.

No particular constraints were given in matter of target shape. After some first consideration and simulations on a full block of pure tungsten – as originally proposed by the experiment [9] – cooled externally by water, the target design was considered as an assembly of several slices that could be cooled down also perpendicularly to the beam axis.

Even with such a configuration though, the temperatures of the refractory metal blocks were too high and a less dense material was then selected for the first blocks in order to spread the energy along the length: molybdenum (and in alternative its alloy TZM (titanium-zirconium-molybdenum)) was the best compromise in terms of density and resistance at high temperatures and stresses.

This section describes in detail the thermo-mechanical simulations performed on the proposed design of the SHiP production target.

1.2.5.1 Material properties

A significant part of the work has also been devoted to a literature review on the available properties for the various materials analysed in this conceptual design. The evolution of the properties as a function of temperature is also very important, as the blocks reach very high temperature, at the limit of the service values.

The material properties of Molybdenum, TZM and Tungsten at room temperature are shown in Table 3, while Table 4 reports the sources for the properties as a function of temperature.

Figure 18 summarizes the mechanical properties or pure W, pure Mo and TZM as a function of temperature. Those values have been used for the thermo-mechanical evaluation of the SHiP production target behaviour subject to the proton beam impact.

Table 3: Mechanical properties at room temperature (20 °C) of pure molybdenum, TZM and pure tungsten.

Properties	**Molybdenum**	**TZM**	**W**
Density [kg m^{-3}]	10220	10200	19250
Coefficient of thermal expansion [K^{-1}]	5.16*10^{-6}	4.99*10^{-6}	4.43*10^{-6}
Thermal conductivity [W m^{-1} K^{-1}]	139	118	173
Specific heat [J kg^{-1} K^{-1}]	246	267	132
Young modulus [GPa]	327	310	400

Table 4: The table summarizes the sources for the material properties employed in this study.

	Molybdenum	**TZM**	**Tungsten**
Main Source	MPDB	IAEA	MPDB

Thermal conductivity	C.Y. Ho, R.W. Powell and P.E. Liley, J. Phys. Chem. Ref. Data, v1, p279 (1972)	International Atomic Energy Agency Iter Blanket, Shield And Material Data Base IAEA, Vienna, 1991 IAEA/ITER/DS/29 Part B Material database: D.Smith, I.V.Altovsky, V.R.Barabash, J.Beeston, M.Billone, J.L.Boutard, T.Burchell, J.Davis, S.A.Fabritsiev, Mgrossbeck, A.Hassanein, G.M.Kalinin, P.Lorenzetto, R.Mattas, K.Noda, R.Nygren, N.V.Odintsov, V.V.Rybyn, H.Takatsu, V.P.Vinokurov, R.Watson, C.Wu	C.Y. Ho, R.W. Powell and P.E. Liley, J. Phys. Chem. Ref. Data, v1, p279 (1972)
Coefficient of thermal expansion	F.C. Nix, D. MacNair, Physical Review, v61, p74 (1942) and A.G. Worthing, Physical Review, v28, p190 (1926) and H.L. Laquer, Low Temperature Thermal Expansion of Various Materials, Dec. 9, 1952, ADA307613		G.K. White, R.B. Roberts, High Temperatures-High Pressures, v15, p321 (1983) and R.R. Kirby, High Temperatures-High Pressures, v4, p459 (1972) and F.C. Nix, D. MacNair, Physical Review, v61, p74 (1942)
Specific heat	P.D. Desai, J. Phys. Chem. Ref. Data, v16(1), p91 (1987)		G.K. White and S.J. Collocott, J. Phys. Chem. Ref. Data, vol 13, no 4, p1251 (1984) and A. Cezairliyan, J.L. McClure, J. Research National Bureau Standards, v75A, p283 (1971)
Young modulus	ASM Handbook, vol 2, 10th edition, ASM International (1992) and W. Koester, Z. Metallkde., v39(1), p1 (1948) (in German)		Lowrie R. and Gonas A.M., J. Applied Physics, v.38, p.4505, (1967) and W. Koester, Z. Metallkde., v39(1), p1 (1948) (in German) and P.E. Armstrong and H.L. Brown, Trans. AIME, v230, p962 (1964)

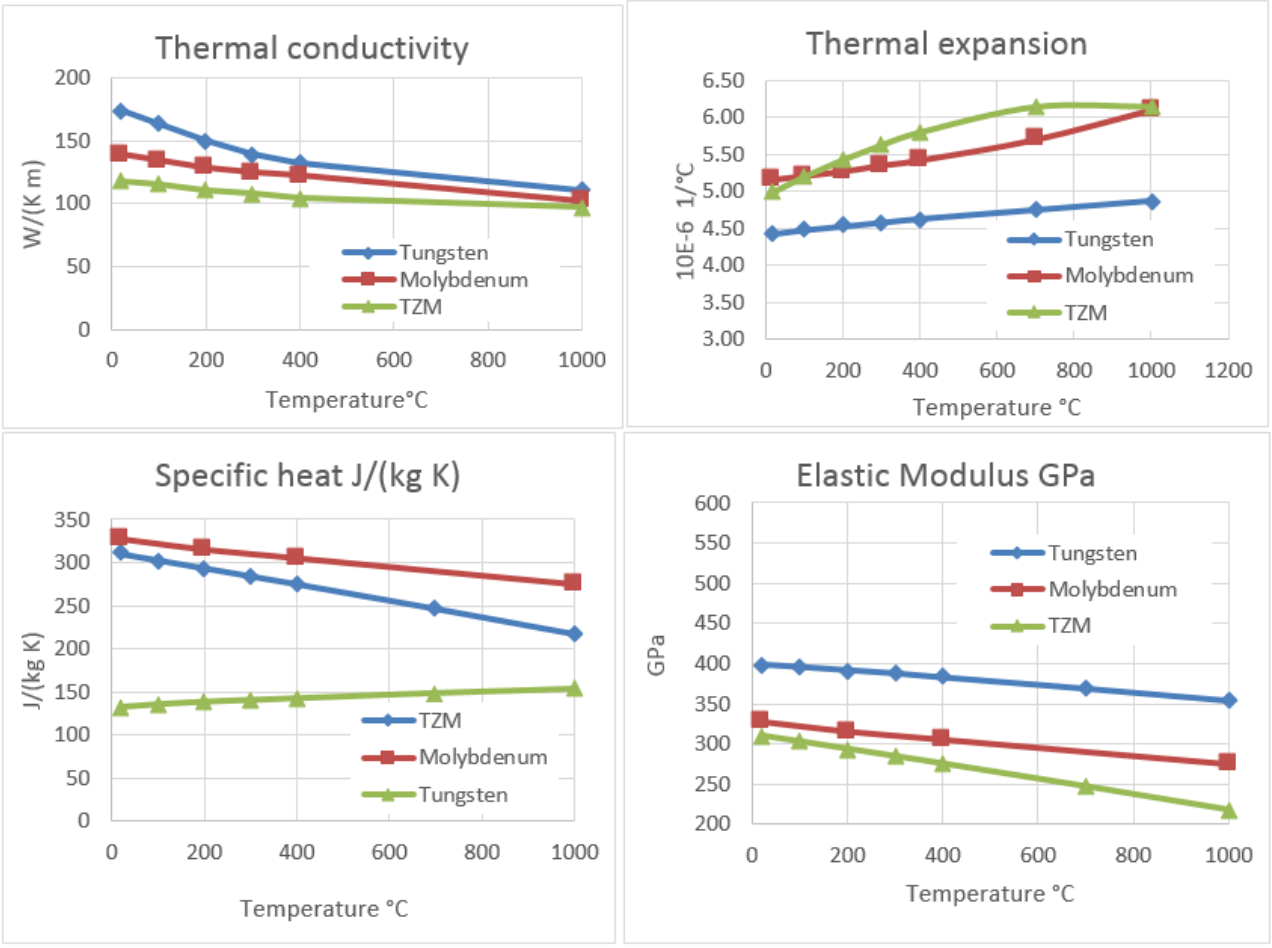

Figure 18: The figure reports the evolution of critical mechanical properties as a function of temperature, as extracted from the sources indicated in Table 4.

1.2.5.2 SHiP production target proposed design

The target proposed solution is the result of many iterations in order to distribute the energy in the most even way possible on the various slices along the beam axis (see section 1.2.4). Figure 19 shows the final version of the target configuration, represented as ¼ of the entire model. All the blocks have the same cross section (30 x 30 cm^2) but different thicknesses, as reported in Table 2.

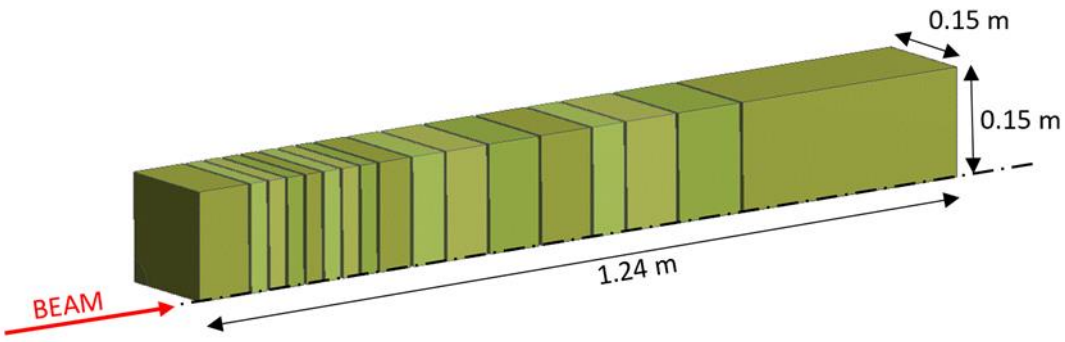

Figure 19: SHiP target design proposal: squared cross section slices of different thicknesses and material (1/4 model)

At the present level of conceptual design, the target is water-cooled, with the cooling inlets are placed on the top of a vessel containing the target (see Section 1.3 for more details on the detail of the conceptual design).

Water is assumed to be injected with a flow rate of 50 liters/s (180 m^3/h) at a pressure of 15 bar in order to increase its boiling point at a temperature of roughly 200 °C and avoid vapour formation when in contact with the target plates (see Section 1.2.6 for more details on the target CFD analysis). The coolant is allowed to flow through the 5-mm gaps between the various slices and not on the lateral sides, to be then recollected on the bottom of the vessel.

This system allows for the most effective heat exchange, since water flows through the hottest parts of the target while the circulation on the sides can be avoided, simplifying the design of the assembly.

The vessel containing the target and the water system is made of stainless steel with a wall thickness of 2 cm and is included in a second external containment tank where a closed helium gas circulation ensures a dry and controlled environment (to reduce corrosion) as well as the possibility of monitoring a possible water leak from the internal containment.

The target cooling circuit is schematically represented in Figure 20. A more detailed target drawing is available in Section 1.3.

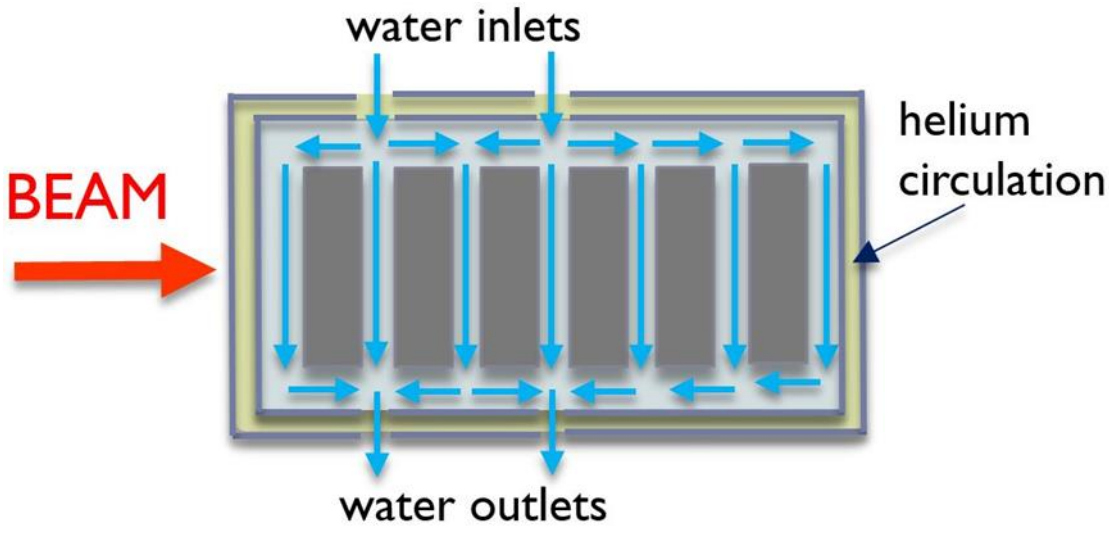

Figure 20: Schematic representation of the target assembly with the double containment system as well as the water and the helium gas circulation. The drawing is not in scale.

1.2.5.3 Simulation approach description

Thermo-mechanical simulations have been performed by means of the ANSYS proprietary code.

For a realistic simulation of the slowly extracted beam diluted on the target, a dedicated APDL (ANSYS Parametric Design Language) code was developed. The code allows moving – in space and time – the heat source provided by the FLUKA simulation over the spiral shape chosen for the painting (see Figure 2).

The classical methodology used to import energy for a non-swept beam, starts from a 3D FLUKA energy deposition file where the binning could be in Cartesian or cylindrical coordinates. The file contains the energy density per primary interacting particle generated inside a certain material by the beam interaction. This heat source is applied over a certain time according to a fixed coordinate system, usually with origin on the beam axis.

In order to verify the new code, two configurations of FLUKA energy deposition were produced. The former models the energy coming from a beam that has a spiral shape, as described in Section 1.2.4. In this case, the total energy per pulse is applied simultaneously on the entire spiral profile, over the pulse time with an average power over the pulse duration. In other words, this method assumes that the beam has the shape of a spiral (instead of having the usual shape and being painted over a spiral profile). The method used for this approach is the classic method in which the energy is applied once, in the centre of the target. Such an approach will be referred to as "approximated method" of the real sweep, as its computational time is in the order of 10 minutes per pulse considering a simulation on all the slices of the target and ¼ of the geometry (mesh around 300000 nodes).

The second version of the FLUKA energy deposition is the energy coming from a beam with no sweep (with the nominal beam sigma of 6 mm) and the energy is applied with a discretization in time and space. In each of the discretization points there is a fraction of the total power. This method will be referred to as "full sweep method". The computational time in this case, is in the order of 1 day for a single slice of the target (with a mesh refined at 300000 nodes per slice).

With the same mesh size, the full sweep method with 1000 discretization points is 144 times slower than the approximated method.

The two methodologies are schematically shown in Figure 21.

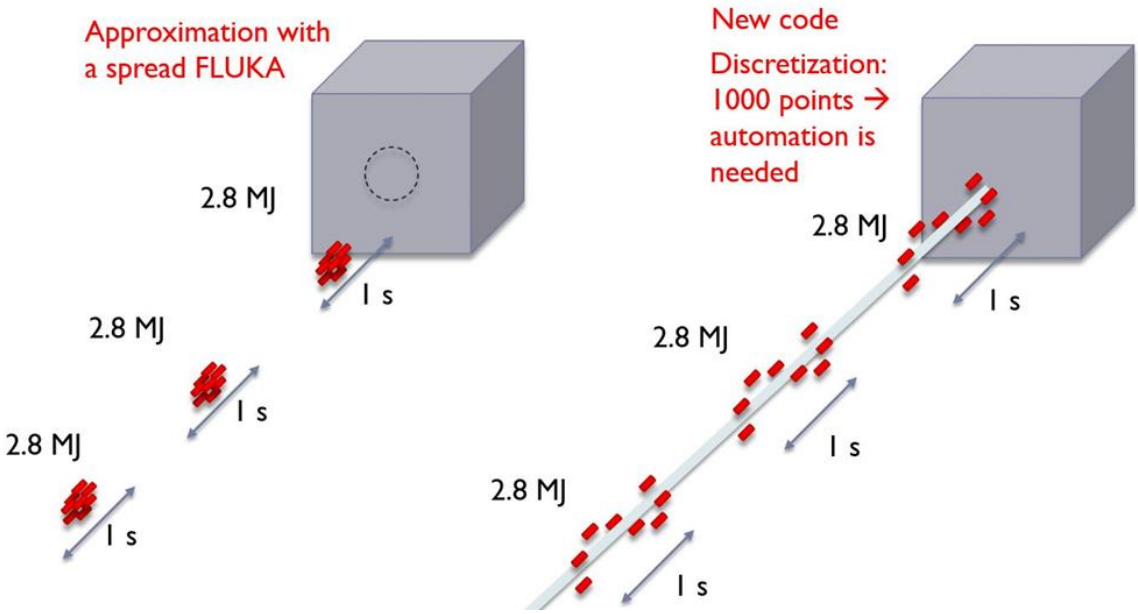

Figure 21: Schematic representation of the two methodologies used to model the energy deposited by the beam: average power over the spiral with approximated method (left) and full sweep beam simulation (right)

Thanks to the code specifically developed for SHiP, it is possible to apply in an automatic way the heat source and move it along the spiral independently of the mesh used. The code creates in ANSYS 1000 coordinates systems based on the discretisation of the spiral shape. Then 1000 different "load tables" (each containing the information about the energy deposited in the volume by a fraction of the total particles and according to one particular coordinates system) are created and applied one by one at different time intervals.

Figure 22 and Figure 23 compare the simplified (approximated) procedure and the full sweep method, with particular attention to the way ANSYS imports the load.

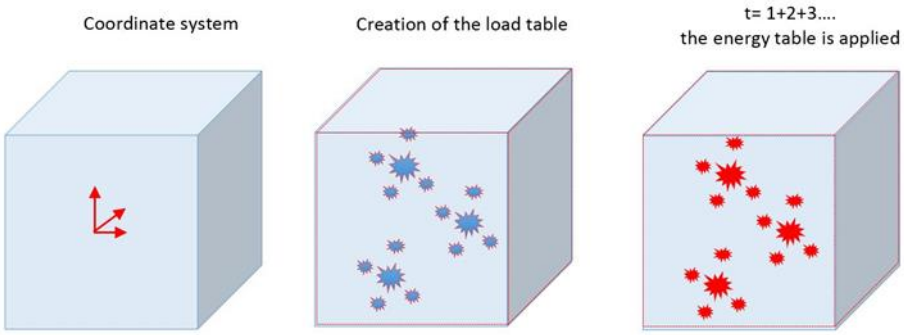

Figure 22: Heat generation approximated method in ANSYS: one single energy distribution (spread on a spiral shape) is applied at once during the pulse time (where 1, 2, 3 ... are fractions of the pulse time).

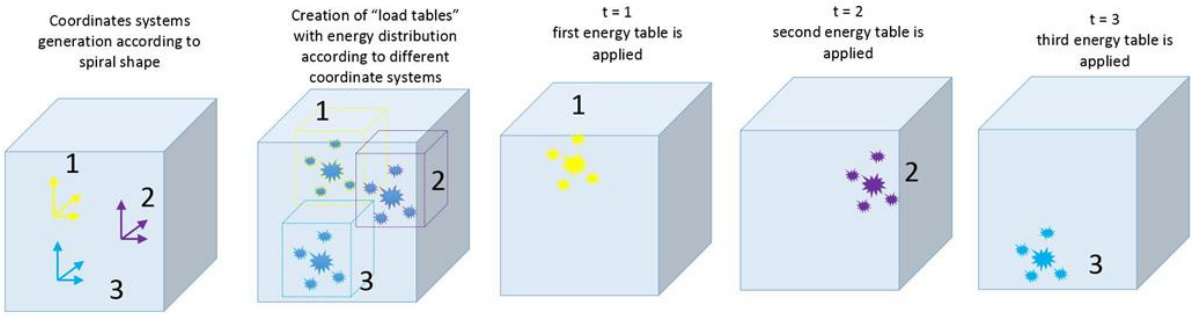

Figure 23: Heat generation with the new method in ANSYS: discretization in time and space, the energy is applied progressively along the spiral path.

The results obtained by applying the full spiral method in terms of reached temperature are expected to be more optimistic than the results obtained by applying the load with the approximated method. Applying the beam all at once during one second, even if with the same total power would in fact accumulate heat in the central part of the target with a resulting higher peak temperature at the end of each pulse. On the contrary, the sweep beam simulation would allow for a better dilution of heat during the pulse (as expected to happen in reality).

As boundary condition, a conservative heat transfer coefficient of 10000 W/(m^2*K) with water temperature of 25 °C has been applied on the surfaces in direct contact with the beam, according to the CFD simulation results (see Section 1.2.6). The general methodology for the thermo-mechanical simulations includes a first approach to the temperature estimation with the approximated method to check which ones are the most critical slices to be considered for a full detailed analysis. Then the full sweep method is applied just to the critical components and compared with the previous results.

1.2.5.4 Temperature simulations

The structure of the proton beam coming from the SPS, with its very high energy per pulse and long time period, combined with a high cooling rate, generates oscillating temperature fields on the target with a significant ΔT between the cycles. The simulations show that the maximum temperature is reached after 5 SPS pulses on target.

The approximated method for the pure material configuration shows that the maximum temperatures are reached in the slice #9 for what concerns the TZM part, and #14 for the pure tungsten part (i.e. the first W block). The maximum temperature depends not only on the integral energy deposited per piece but also on its thickness.

Results are shown in Figure 24:

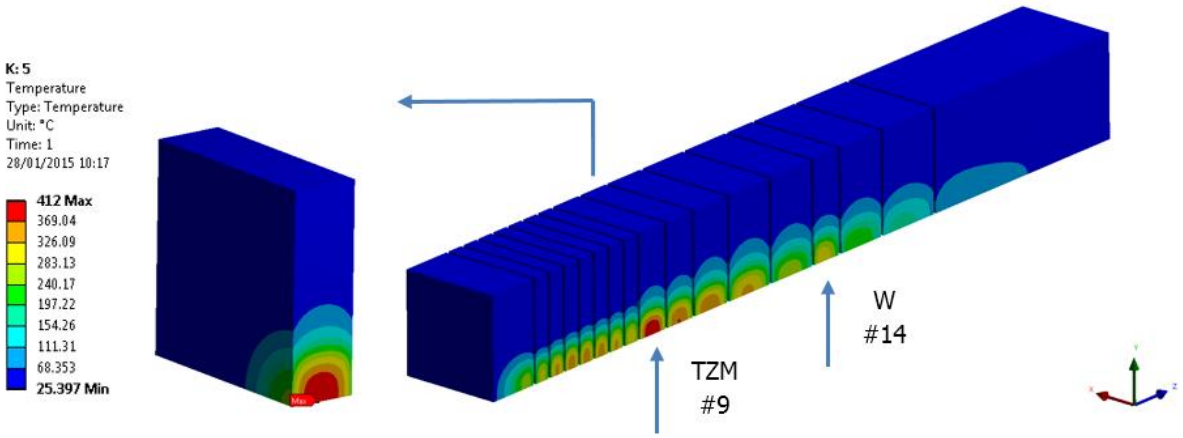

Figure 24: The figure shows the TZM and tungsten maximum temperatures after 5 pulses calculated with the approximated method. The insert shows a more detailed view on the #9 TZM block.

The two most critical slices were then studied also with the full sweep method. No significant difference was found in the peak temperature of tungsten because the diluted proton beam goes through many blocks and spreads significantly before reaching them. For TZM, being the beam impacting still very focused, the full sweep calculation indicates lower operational temperature. The sequence showing the temperature field evolution on 9th block during the first pulse is shown in Figure 25. The temperature evolution on the most heated node after 5 pulses is shown in Figure 26: it is evident the thermal cycling on the blocks during the 6.2 seconds interval between 2 consecutive pulses. Similarly Figure 27 shows the temperature evolution for the first 5 pulses for the hottest blocks of each material (#9 for TZM/Mo, #14 for W).

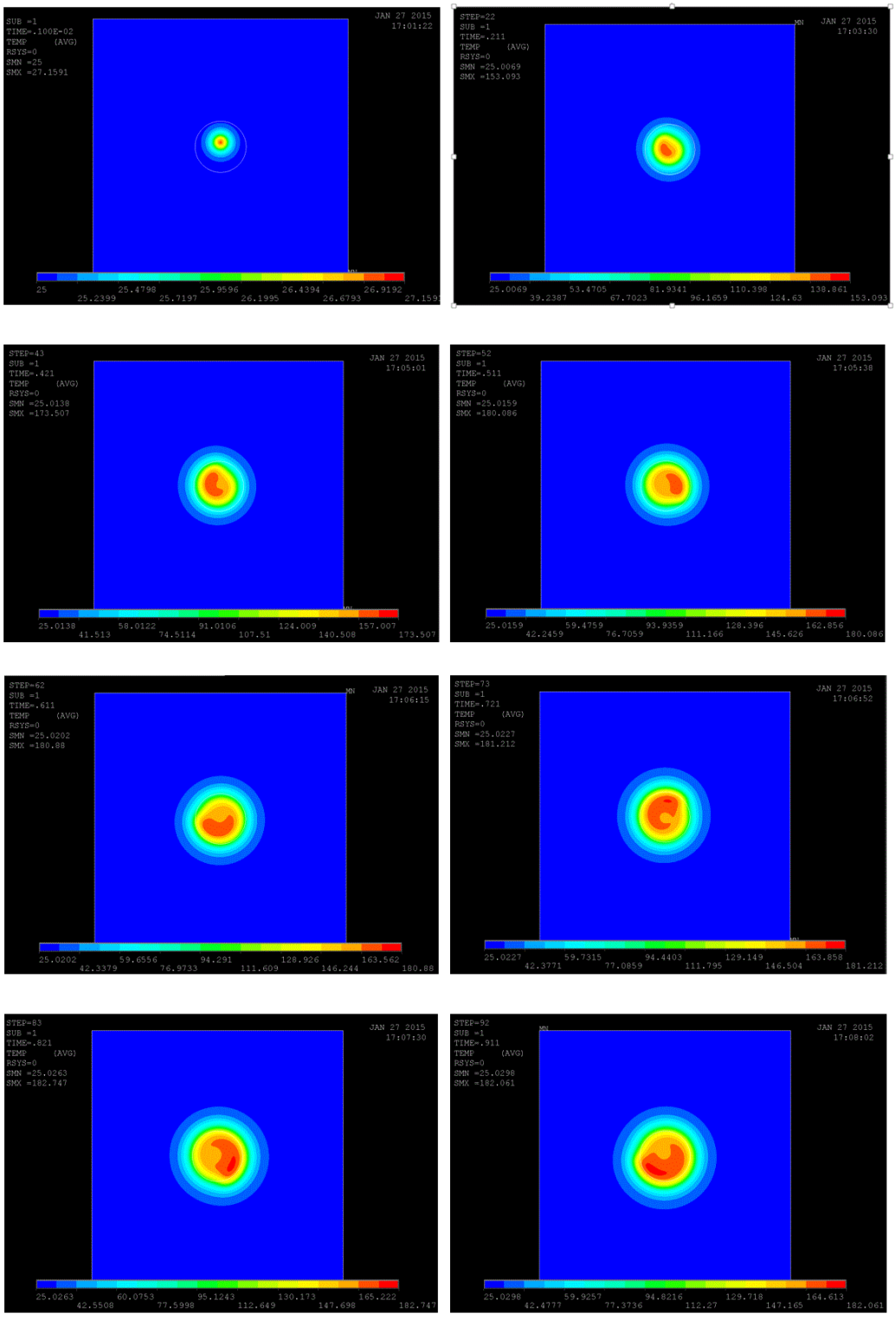

Figure 25: Temperatures evolution on the surface of TZM during the first second, calculated with the full sweep method. Each figure represents 1/8 of the total duration of the pulse (1000 ms).

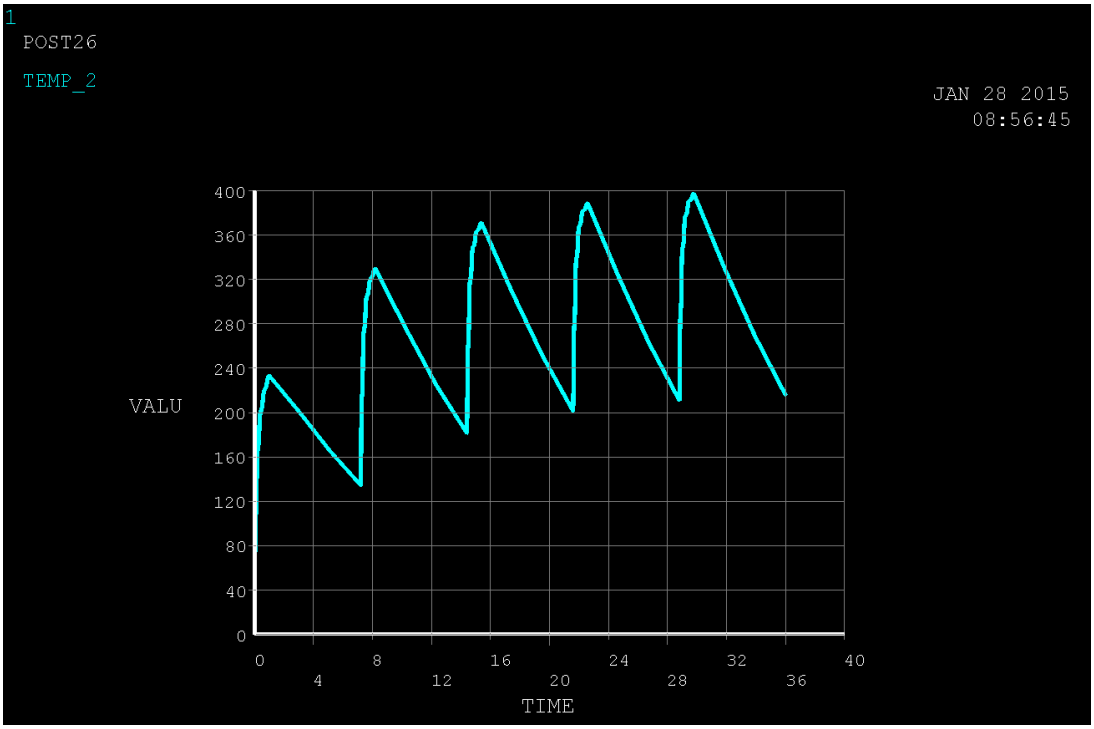

Figure 26: TZM temperature evolution of the hottest node after 5 pulses, produced with the full sweep method (temperatures are reported in °C on the Y-axis and time in seconds on the X-axis).

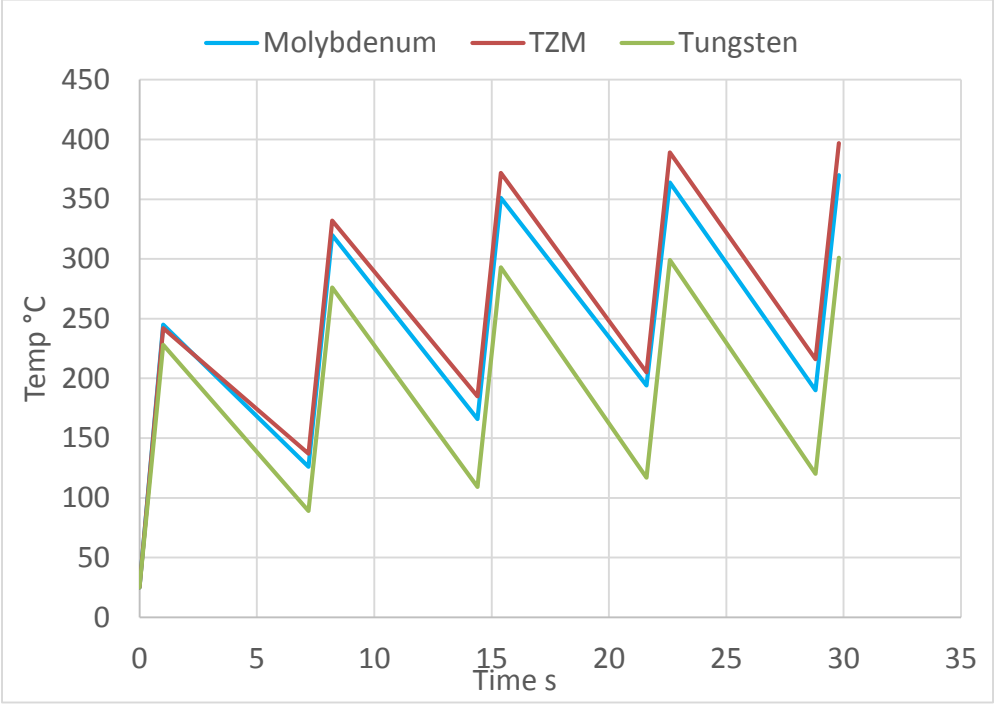

Figure 27: The figure shows the temperature evolution observed in the blocks for various refractory metals during 5 consecutive pulses starting from ambient temperature (pure molybdenum and TZM are given for comparison for the first half of the target).

Maximum temperatures are ranging between 216 and 397 °C for TZM and between 106 and 312 °C for Tungsten.

The maximum temperatures are admissible for the considered materials, which present very high service temperatures, but would create considerable stress that will be analysed in details in the following section. Those stresses will get the same cyclic trend of the peak temperatures so fatigue will also have to be considered.

1.2.5.5 SHiP target structural simulation

The temperature field on the target is such as to generate mainly compressive stresses in the inner part of the blocks and tensile stresses on the external surfaces.

The typical maximum and minimum principal stresses after 5 pulses are shown in Figure 28.

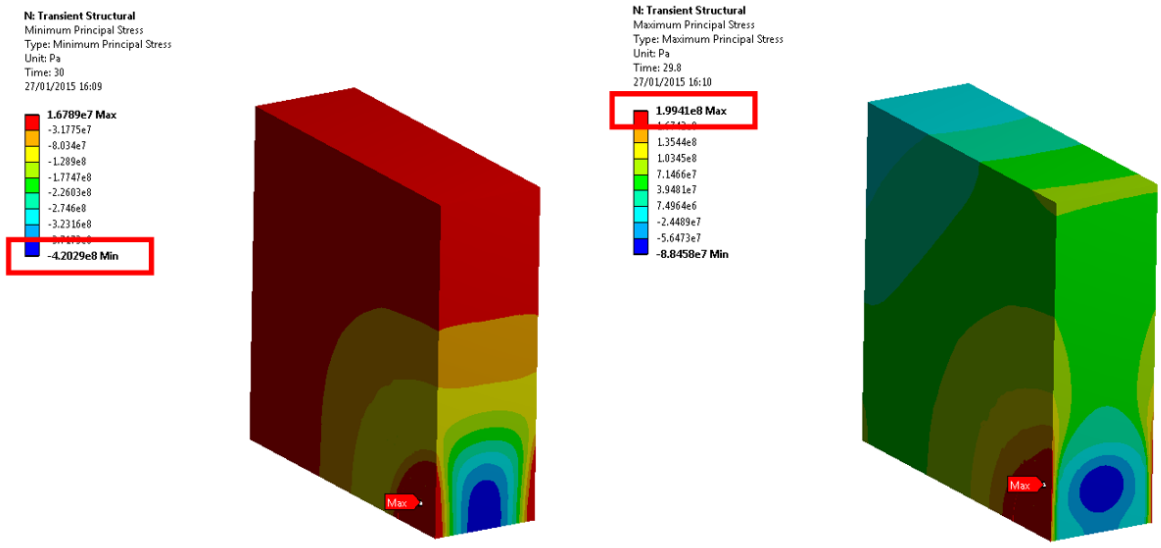

Figure 28: Typical location of maximum (compressive, left figure) and minimum (tensile, right figure) principal stresses after 5 pulses for a pure tungsten block, evaluated with the approximated method.

After each pulse, the stresses will decrease both in tension and in compression before the next pulse.

The cycles of tension and compression assuming pure molybdenum and TZM are reported in Figure 29. The compressive stresses oscillate between 173 and 365 MPa for pure Molybdenum and between 185 and 376 MPa for TZM, while the tensile stresses oscillate between 133 and 210 MPa for pure Molybdenum and between 136 and 219 MPa for TZM.

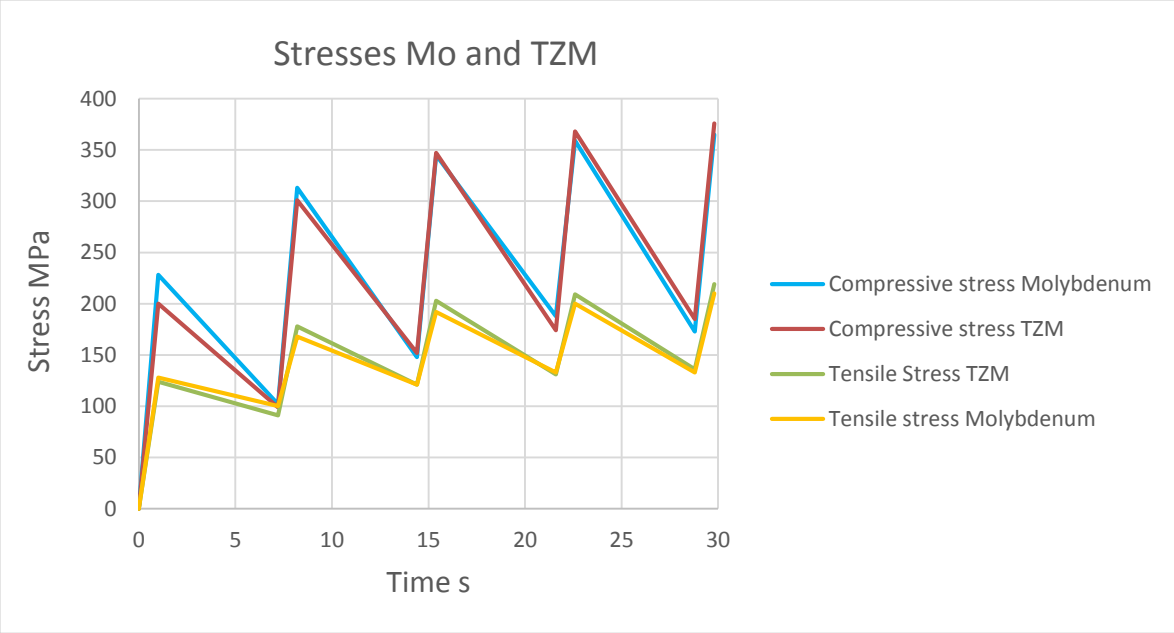

Figure 29: Evolution of stresses in tension and compression for the most critical block, assuming pure molybdenum and TZM as material.

Figure 30 reports the yield strength curves as a function of temperature for both TZM and pure Mo, the TZM yield in compression (single point) as well as the operational stresses (both tensile and compressive) expected for the SHiP target as a function of the temperature. The data show that the resulting stresses are below the yield for the two materials – both in tension and compression – assuming to consider a stress relieved version of the materials (see Section 1.4 for more details on the material properties).

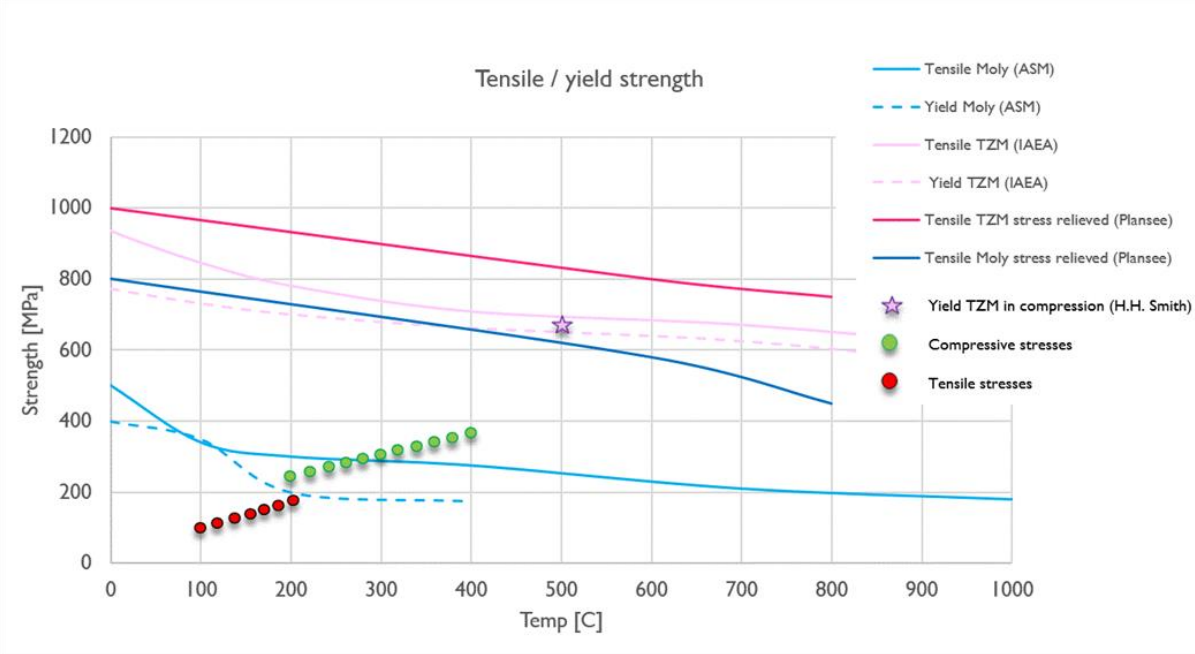

Figure 30: TZM yield and tensile (compressive) strength, as compared to the operational stresses expected for the SHiP target assuming TZM blocks. Data for pure Mo are reported for comparison.

Fatigue at the various temperatures for compression and tension with a stress ratio different from R=-1 are not available in literature. The irradiation effects on TZM is in general leading to an increase in the yield strength of the material and improving the fatigue for compression-tension cycles. Minimum compressive stresses might damage the material inside the block but small defects should not propagate outside the centre. Tensile stresses should be kept under control because they appear on the surface where cladding will be applied and delamination with the cladding material could potentially occur.

Similar plots have been performed for the most critical pure tungsten block (Figure 31).

For pure W the stresses are ranging between 106 and 312 MPa in compression and 34 and 25 MPa in tension. Even though stresses (tensile especially) are lower than the Molybdenum/TZM case, also for this material a dedicated study on the interface with cladding is recommended.

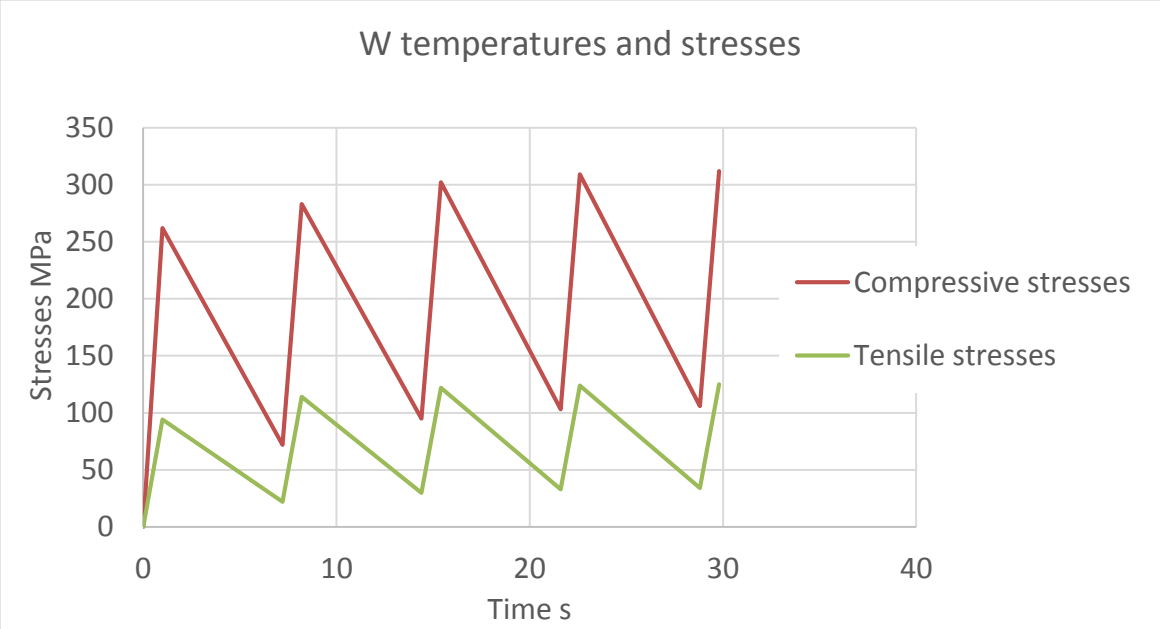

Figure 31: Evolution of stresses in tension and compression for the most critical pure tungsten block.

Figure 32 shows a comparison between the SHiP target tungsten operational maximum stresses and the material resistance in tension and its yield stress as a function of temperature.

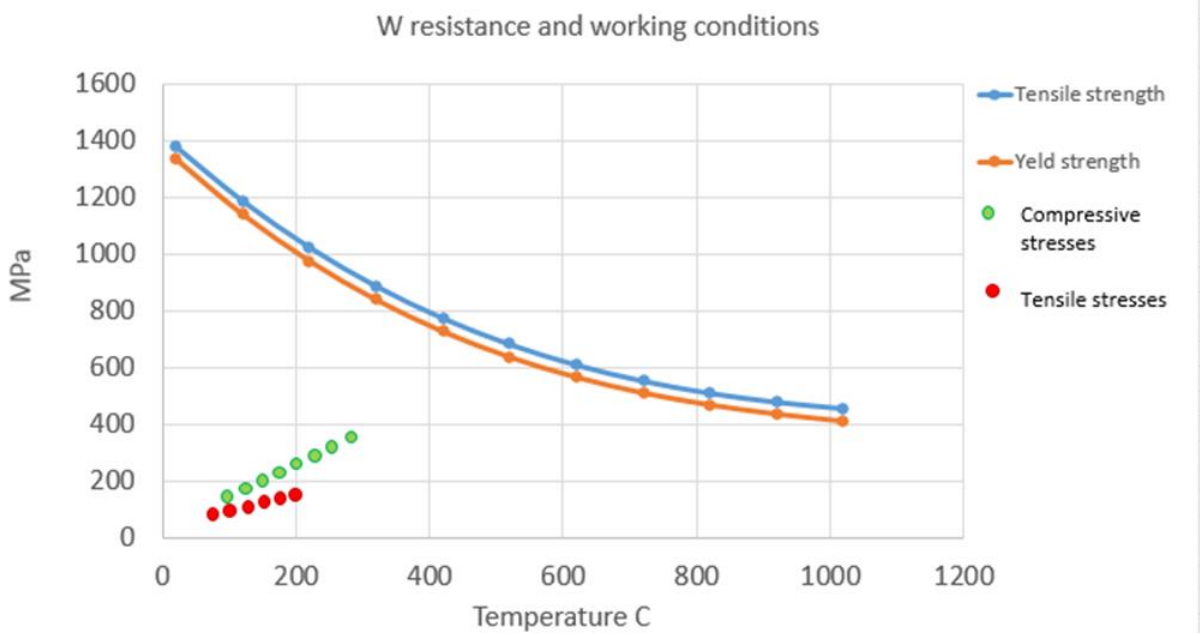

Figure 32: The figure shows pure tungsten yield and tensile (compressive) strength curves, as compared to the operational stresses expected for the SHiP target assuming the most critical tungsten block. The data show that the resulting stresses are below the yield for the two materials – both in tension and compression.

As a final crosscheck, we have performed a comparison between the structural calculations on the most critical TZM block assuming the approximated method and the detailed full sweep analysis. The results (see Figure 33) indicate that the maximum compressive stresses obtained by the approximated method are overestimated by 50 MPa, i.e. by roughly 10%.

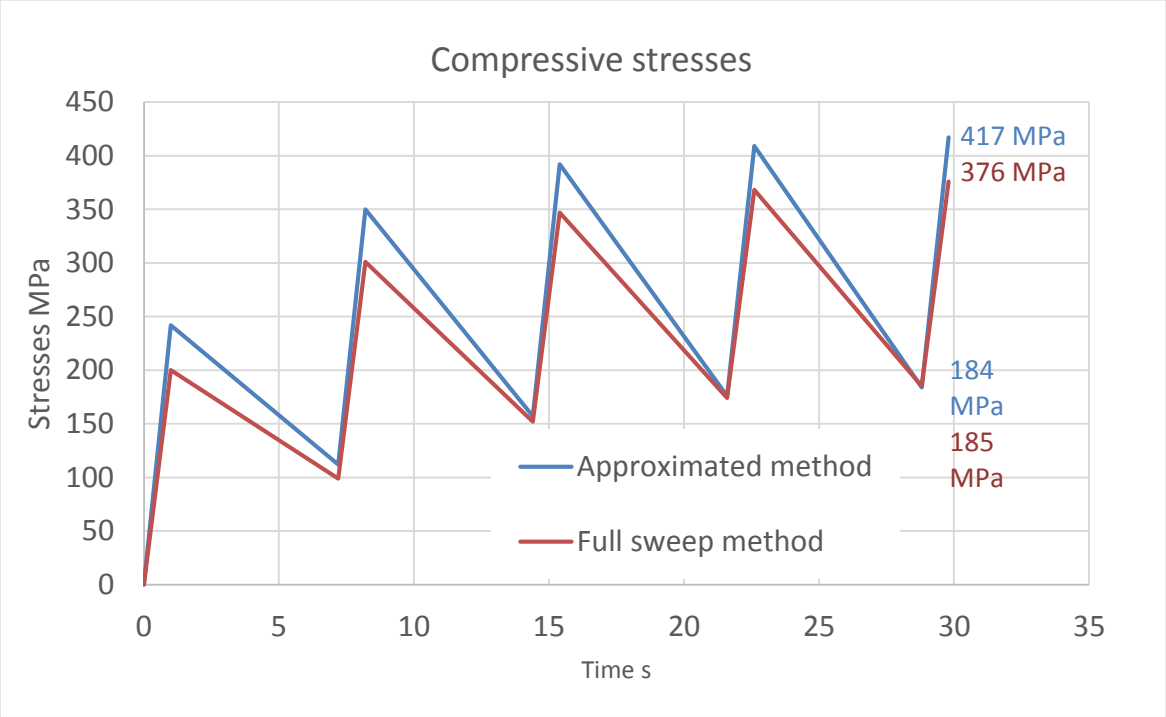

Figure 33: The figure shows a comparison between the compressive stresses on the most critical TZM block by using the approximated method temperature fields for the calculation of stresses and the full sweep method.

The present analysis has shown that with the present SHiP target design the compressive stresses reached in the core of the materials seems not to be too severe assuming a stress relieved version for TZM. The pure tungsten blocks present more safety margins with the present working conditions.

More detailed material considerations for what concerns aspects such as thermal fatigue, creep and mechanical evolution as a function of radiation are discussed in Section 1.4.

1.2.5.6 Accidental scenario

In case of failure of the dilution elements producing the beam sweep in the extraction line, we assume that the full intensity ($4*10^{13}$ protons/pulse) primary beam hits the target in one concentrated area with a 1σ of 6 mm (undiluted primary beam). No interlocking system nor protection devices are presently assumed here, in order to provide an assessment of the target behaviour in the most pessimistic scenario.

The temperature distribution and stress maps for the most critical TZM and tungsten blocks are shown in Figure 34 and Figure 35, respectively.

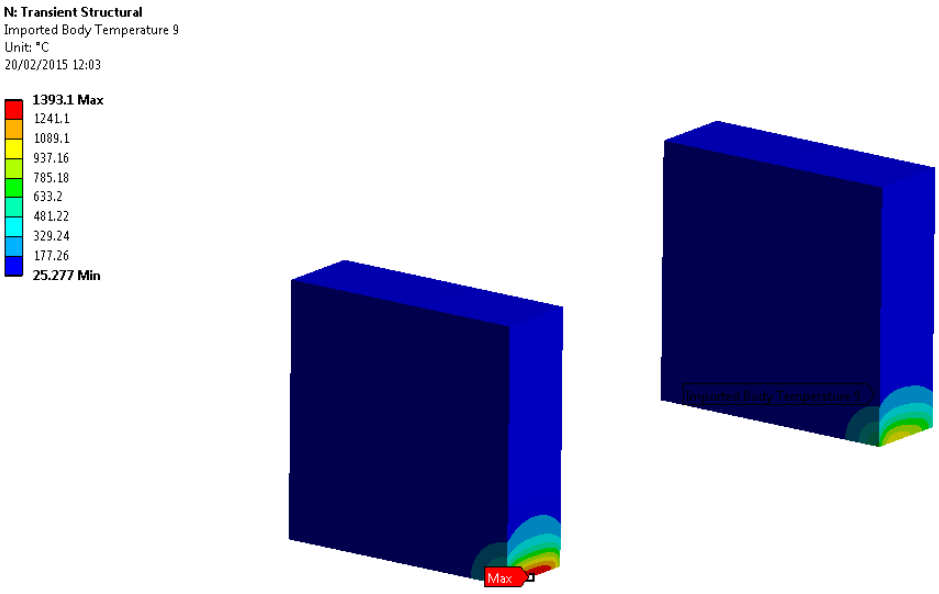

Figure 34: The figure shows the maximum temperature for the most critical TZM block (left figure) and pure tungsten block (right) in case of full sweep failure.

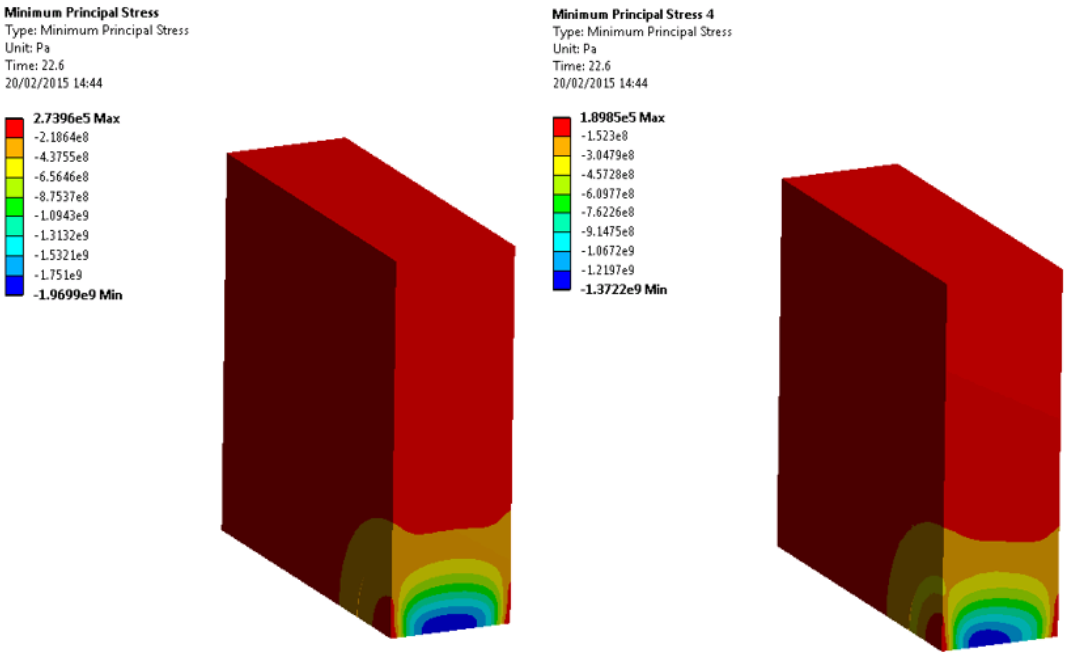

Figure 35: The figure shows the respective maximum compressive stresses for TZM (left) and pure tungsten (right) most critical blocks.

The maximum temperatures at the end of the accidental pulse are around 1400 °C for TZM and around 1000 °C for pure tungsten. Temperatures are close to the maximum service temperatures of both materials and well below the material melting points, but stresses in compression are much higher than the maximum admissible for both materials at these temperature ranges. The highest compressive stresses are around 2 GPa for TZM and 1.3 GPa for pure tungsten.

Given the conditions, during an accident scenario of this sort the SHiP target blocks would not melt but will certainly permanently fracture under the effect of the internal compressive stresses.

1.2.5.7 Target containment study

The target is contained in a double walled shroud. The inner tank will contain the water-cooling loop pressurized up to 15-20 bars, while the external part will be used for the helium circulation between the two layers.

The inner containment is the one subjected to the highest load due to the water pressure and has therefore been verified through a structural analysis. The part is composed by two shells of stainless steel of 20 mm thickness welded together around the target. The shells are symmetric according to a vertical plane passing through the beam line.

Reinforcements on the lateral sides have been foreseen to hold the target blocks, while vertical elements are used as spacers in order to maintain the gap between the slices.

Steady state thermal analyses, performed by loading the energy deposition from the FLUKA studies and a conservative heat transfer coefficient of 10000 W/(m^2*K) indicate a maximum temperature of ~50 °C.

Structural simulations indicate that for a pressure of 10 bar the maximum stress found is in the order of 100 MPa (see Figure 36). For a 20 bar pressure circuit the value increases to roughly 170 MPa (see Figure 37). The latter value is also below the 0.2% offset yield strength of the SS316LN, which is in the order of 205 MPa.

The structure is therefore expected to remain in the elastic regime. The design of the containment structure could be further improved, relaxing even further the stresses of the inner shroud. The maximum deformation expected for a 20 bar circuit and 20 mm thick containment is 0.5 mm.

It should be noted that this design will have to be further developed in order to comply with pressure vessel standards applicable at CERN [10]. This will probably result in an increase of the wall thickness or the addition of stiffeners on the outside of the inner tank.

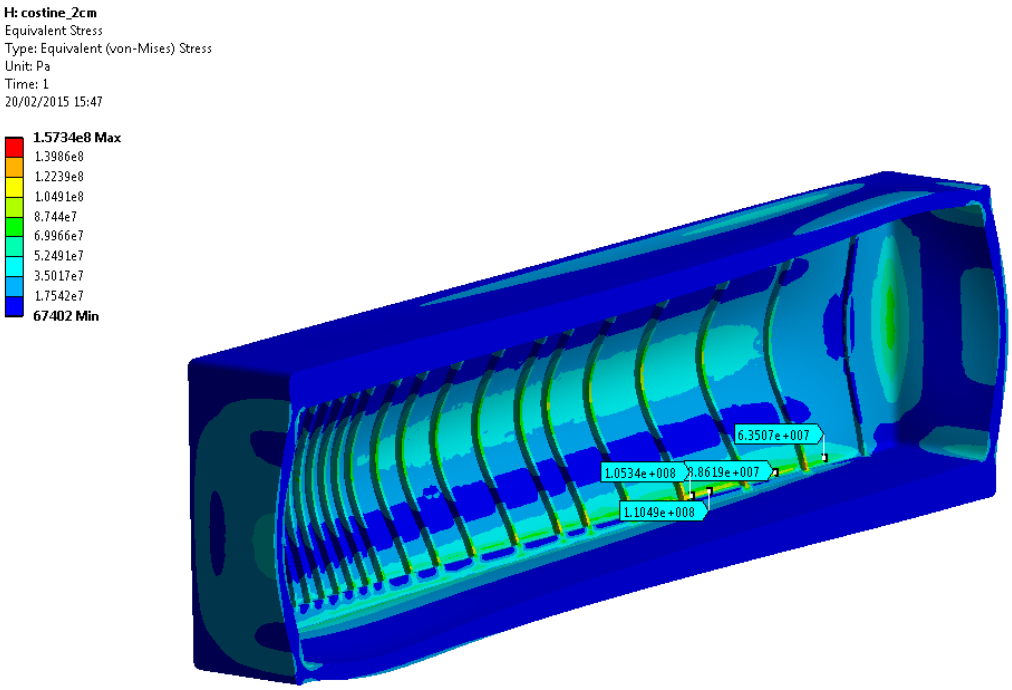

Figure 36: Resulting Von-Mises stresses for 10 bar pressure and a 20 mm thick inner containment. A numerical singularity occurs in the lower part of one rib.

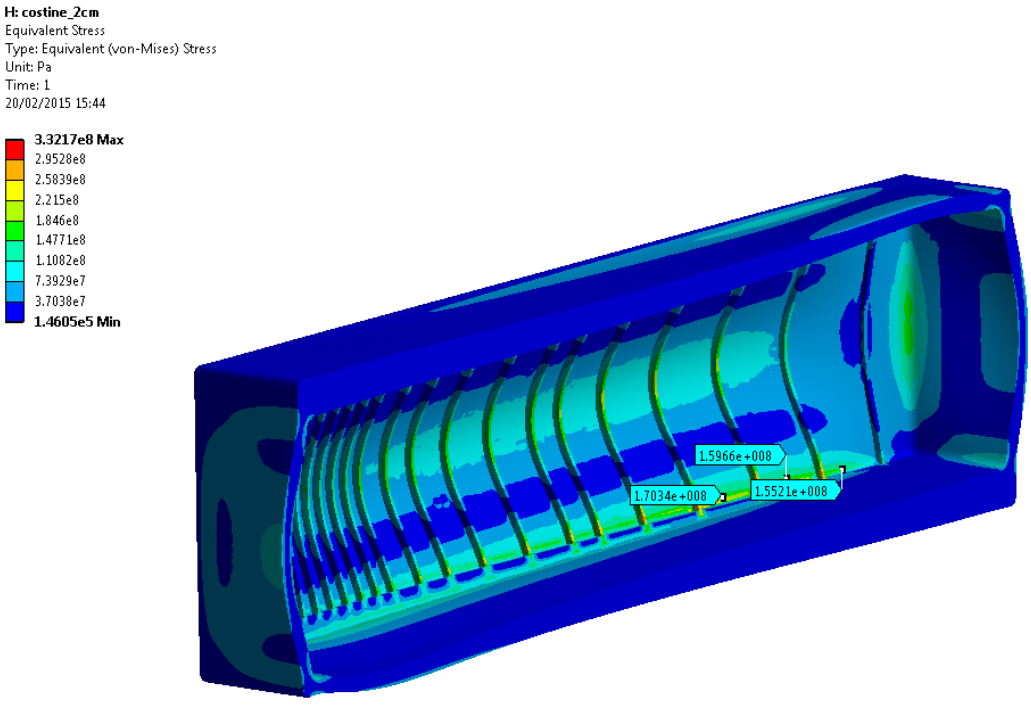

Figure 37: Resulting Von-Mises stresses with water pressure of 20 bar and a 20 mm thick inner containment. A numerical singularity occurs in the lower part of one rib.

An additional check was performed on the upstream window, which separates the helium of the bunker from the helium gas inside the target's external containment. This

is particularly critical due to the lack of active water cooling, contrary to the inner window separating the internal and the external shrouds.

Two materials were simulated, SS316L and ferritic steel T91 (which seems to behave better in radiation environments). The latter presents the advantages of higher thermal conductivity and heat capacity. The boundary conditions employed for the calculations are a low heat transfer coefficient for the side in contact with helium (10 W/(m^2*K)) and insulation for the upstream side (a very conservative assumption).

The results are reported in Figure 38, indicating a maximum temperature of 95 °C in case of T91 and 135 °C in case of SS316L.

The respective compressive stresses are shown in Figure 39, roughly 130 MPa for SS316L and 52 MPa for T91. In both cases the stresses are lower that the yield strength of the materials and can be considered safe from the point of view of operation.

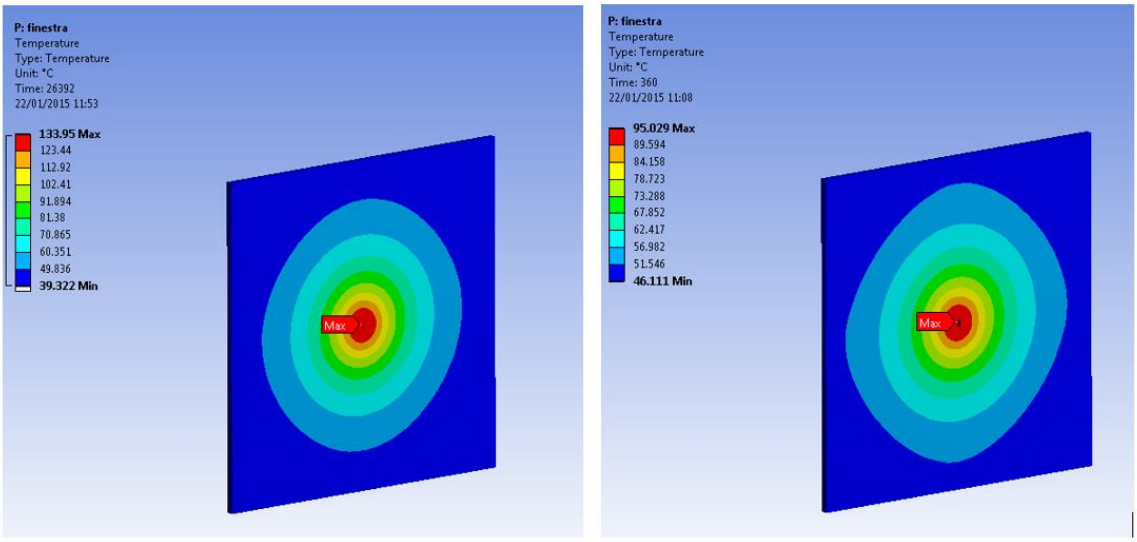

Figure 38: The figure shows the resulting temperatures for the upstream window in case of SS316L (left figure) and for ferritic steel T91 (right figure).

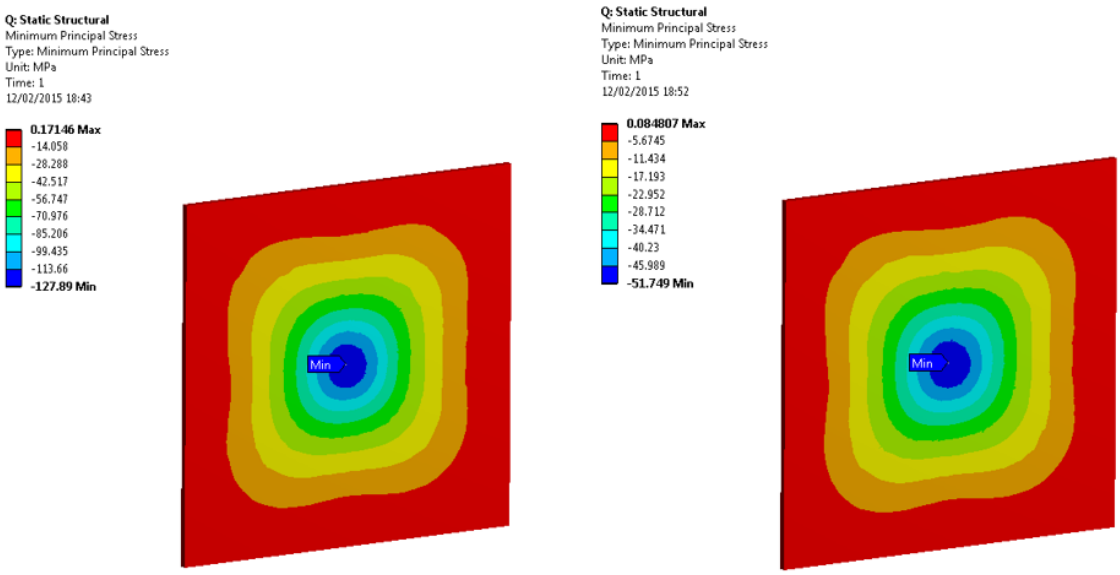

Figure 39: The figure reports the resulting compressive stresses for the upstream window in case of SS316L (left figure) and ferritic steel T91 (right figure).

1.2.6 SHiP target CFD simulations

1.2.6.1 Introduction

Pressurized water at 10 bar was initially selected as coolant for the system, with a boiling point of around 180 °C. Due to the extreme conditions reached in the target, CFD calculations of the cooling medium behavior are required to assess the feasibility of the whole system and to provide a reliable estimation of the heat transfer coefficient to be employed in the mechanical calculations.

As a first approximation, assuming that all of the water is uniformly heated up by 50 degrees in all of its volume, the required mass flow rate can be calculated as follows:

$$Q = mC_p dT \Rightarrow m = \frac{Q}{C_p dT} = \frac{2 \times 10^6}{4.2 \times 10^3 \times 50} = 9.5 \frac{kg}{s} \approx 10 \frac{l}{s}$$

This approach, however, is completely theoretical and does not take into consideration real local phenomena related to heat transfer, i.e. the fact that the heat is transmitted gradually from the wall to the centers of the gaps. Therefore, due to the complexity of the system, one needs to do a CFD simulation to evaluate the effects taking place in the boundary layers between the water and the target blocks.

All simulations described in this section have been conducted using the proprietary ANSYS FLUENT software package.

1.2.6.2 Boundary layer and y+ considerations

In general, heat transfer conditions for the entire system are governed by 3 parameters: the contact area between the hot block walls and the coolant; the absolute temperature difference between them and the heat transfer coefficient, which depends significantly

on coolant velocity and; its temperature-varying properties. Considering the present design of the cooling system, water will heat up locally in the vertical wall to relatively high temperatures and phase change need to be avoided (occurring at 180 °C for water at 10 bar pressure, as mentioned before).

In turbulent problems such as the one in question, it is extremely important to appropriately account for boundary layer effects in order to correctly simulate the heat transfer conditions in the direct vicinity of the wall – i.e., the viscous sublayer, buffer layer, as well as the log-law region.

The problem that arises here is the spatial discretization: essentially, the main condition that needs to be satisfied is that the dimensionless wall distance for the first cell of the mesh, y+, is around 1. This condition defines the number of cells in the gap and, as a result, the size of the mesh.

The width of the first cell (the one closest to the wall) can be calculated using the following formula:

$$\Delta y = D_h \cdot y_+ \cdot \sqrt{74} \cdot Re^{-\frac{13}{14}} = 0.01 \times 1 \times \sqrt{74} \times 27000^{-\frac{13}{14}} = 6 \times 10^{-6}\, m = 6\, \mu m$$

Assuming that the gap width is fixed at 0.5 cm and complying with the smooth cell size transition criteria, so that the size of the next cells grows by 1.2, one sees that around 50 cells are required in order to appropriately simulate the boundary layer for the problem.

While the aspect ratio in the boundary layer is not a big issue, as flow in the viscous layer is mostly one-dimensional, it provides a significant numerical issue in the manifolds, where the flow is distributed to the gaps. A mesh of 100 million cells (which would take a significant amount of time to simulate using CERN workstation clusters) was created but the aspect ratio in the manifolds was still a concern. Therefore another approach had to be taken in order to be able to simulate the problem.

1.2.6.3 CFD methodology

Due to the reasons described above, the problem had to be split in two.

First, a steady-state simulation was conducted, with heat deposition averaged over 7.2 s of pulse period, i.e. constant heat load of around 300 kW. The mesh created for that simulation consisted of 20 cells across each gap and totalling 4.5 million cells, resulting in y+ on the order of 3-10 in the gaps (see Figure 40).

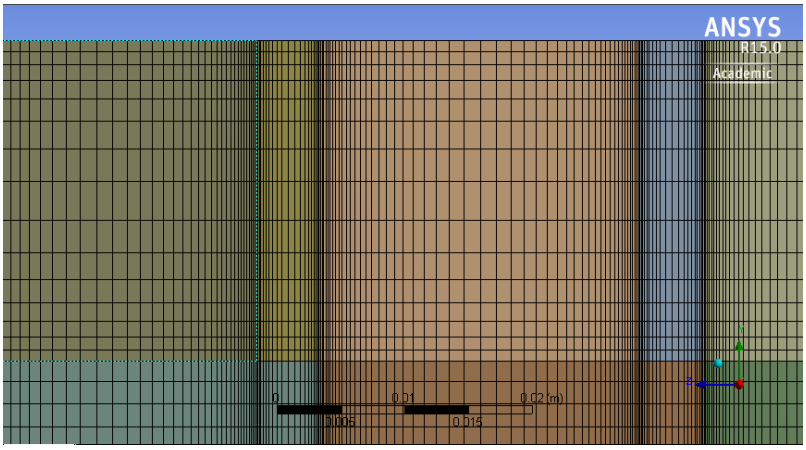

Figure 40: ANSYS FLUENT mesh with manifolds, close-up view at the top of the target.

After the simulations had converged, the velocity and turbulence conditions at the gap inlets as well as the pressure and turbulence conditions at the gap outlets were exported.

Then, the exported data was imported into a second simulation, for which a separate mesh without top and bottom manifolds (see Figure 41) and y+ around 1 (which translates to 40 cells across gap), totalling also 4.5 million cells, was generated.

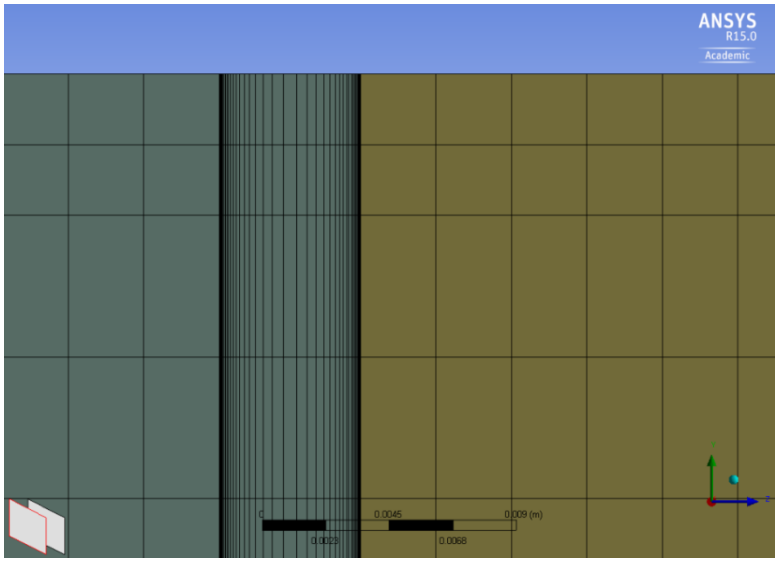

Figure 41: ANSYS FLUENT mesh without manifolds, close-up view at the top of the target.

1.2.6.4 Gap width optimization – analytical approach

For the optimization of the gap width an analytical approach was followed, i.e. by minimizing the standard deviation of temperature drop (along the length), implying that heat transfer conditions are the same in all channels.

In general, to calculate the temperature drop in the channel one can use the following equation.

$$Q_y = hA(T_s - T_\infty)$$

and solve for T_s. However, the heat transfer coefficient (HTC), h, bulk fluid temperature, T_∞ and dissipated power, Q, have to be explicitly known. As Q and T_∞ can be considered given for our problem, only HTC has to be calculated. HTC is in general a function of dimensionless Nusselt number:

$$h = \frac{k}{D} Nu$$

Nu number in turn depends on Reynolds and Prandtl numbers. The empirical correlation used for calculation of Nu number for flows in ducts was given by Dittus and Boelter and is as follows:

$$Nu = 0.023 Re^{0.8} Pr^n \text{ , where } Re = \frac{\rho v_s D}{\mu}$$

Altogether, this shows that the heat transfer coefficient is a function of the hydraulic diameter (thus of the gap size as well).

$$h = \frac{k}{D} 0.023 Re^{0.8} Pr^n = f(D^{-0.2}) => T = f(D^{0.2})$$

The problem is that $f(D^{0.2})$ is an increasing function, thus when the gap size increases, the heat transfer coefficient goes down and the surface temperature increases. Therefore for the stated optimization problem, in spots where heat load is the highest, the gap size should be chosen as small as possible, while in spots where heat load is the lowest, the „ideal" gap size would be as high as possible.

In order to solve the optimization problem, one has to solve a set of 18 non-linear equations. The Non-linear solver used (NOMAD) cannot guarantee an optimal solution but it confirmed what was discussed above. Therefore, an analytical solution to the problem was deemed infeasible.

1.2.6.5 Flow distribution in the gaps

The issue that occurred beginning with the very first simulation was that the flow was not distributed equally in the gaps. In some of the gaps there was 20% of all flow, while in others almost 0%. Adjusting pressure drop by changing gap widths could be seen as a solution. However the simulations have shown that the main problem was the proper balancing of the momentum and gravity forces.

Several inlet and outlet pipe arrangements were simulated, including cases with flow obstacles (orifices) introduced to equalize the flow for all gaps. One arrangement was chosen as superior to the others. It consists of 4 inlet and 4 outlet pipes of approximately 9 cm diameter. It should be underlined, however, that in order to simplify the mesh generation process, all the pipes were considered to have rectangular cross-section. Nevertheless, the total inlet and outlet area in the simulation corresponds to pipes of 9 cm diameter.

1.2.6.6 FLUKA energy deposition data import

When energy deposition data from FLUKA is imported to FLUENT, the software interpolates the data points for all the nodes of the mesh generated for the CFD simulation. Therefore, unless the discretization for FLUKA and FLUENT simulations is the same, there will always be differences in local energy deposition, which result in a slightly different total energy deposition as a starting point of FLUENT.

Table 5 compares the total energy deposition for the blocks as calculated in FLUKA and as interpolated by FLUENT for the flow simulations.

Table 5: The table shows the difference in energy deposition between the one generated by FLUKA and the one imported in FLUENT.

Layer	Material	FLUKA	FLUENT	Δ (%)
1	Mo	85479.32	85691.50	0.25
2	Mo	71841.59	71657.77	0.26
3	Mo	85716.44	85521.50	0.23
4	Mo	92868.56	92732.57	0.15
5	Mo	95496.13	95340.43	0.16
6	Mo	95444.86	91838.41	3.78
7	Mo	93823.45	92844.69	1.04
8	Mo	91311.24	91224.87	0.09
9	Mo	173906.64	173615.59	0.17
10	Mo	160063.84	159850.69	0.13
11	Mo	186877.86	186993.19	0.06
12	Mo	198291.77	197988.24	0.15
13	Mo	166389.23	166197.85	0.12
14	W	153924.30	153714.92	0.14
15	W	159032.04	159066.58	0.02
16	W	130891.41	130812.74	0.06
17	W	155789.23	154586.96	0.77
	Total	2197147.90	2189678.49	0.34

In total, energy deposition in FLUENT is 0.34% lower than the FLUKA deposition data, corresponding to a different of 7.5 kJ of energy.

1.2.6.7 FLUENT – simulation setup and description of simulated cases

The most important input parameters of the simulation setup are listed below:

- Turbulence model: realizable k-ε with enhanced wall functions
- Energy model enabled
- Transient simulation time stepping: up to 0.2 s of each beam – time-steps of 0.01, 0.02 and 0.05s, after 0.2 s of each beam – 0.1 s.
- Material properties:

- Water – taken from REFPROP database, linearly interpolated between 16 data points, inlet temperature of 27 °C;
- Molybdenum and tungsten – taken from MPDB database, linearly interpolated between 6 to 7 points;

The following cases were simulated, assuming a different cooling flow rate and a variation in the water pressure:

- Inlet velocity of 0.5 m/s (~45 m^3/h flow) – case V0.5
- Inlet velocity of 1 m/s (~90 m^3/h flow) – case V1
- Inlet velocity of 2 m/s (~180 m^3/h flow) – case V2
- Inlet velocity of 3.2 m/s (~290 m^3/h flow) – case V3.2
- Inlet velocity of 2 m/s (~180 m^3/h flow) with water at 20 bar instead of 10 bar – case V2P20
- Inlet velocity of 2 m/s (~180 m^3/h flow) with imposed constant, uniform heat flux conditions from the blocks to the manifolds (in other cases it is assumed that there is no heat transfer to the manifolds, which makes them conservative in that aspect) – case V2HT

The average velocity in the gaps in transient simulation is essentially the same for the same inlet velocities, regardless of water pressure and if heat is transferred to manifolds. As reported in Figure 42, the velocity varies more or less linearly with the flow rate. An example of a contour plot for 180 m3/h is represented in Figure 43.

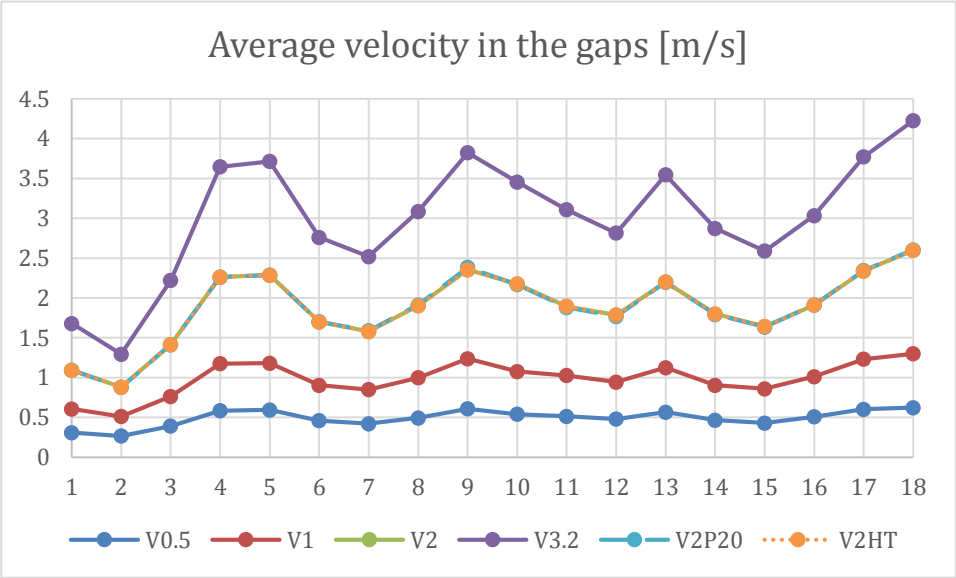

Figure 42: The figure shows the average velocities in the gaps as a function of the gap number and for the various simulated cases.

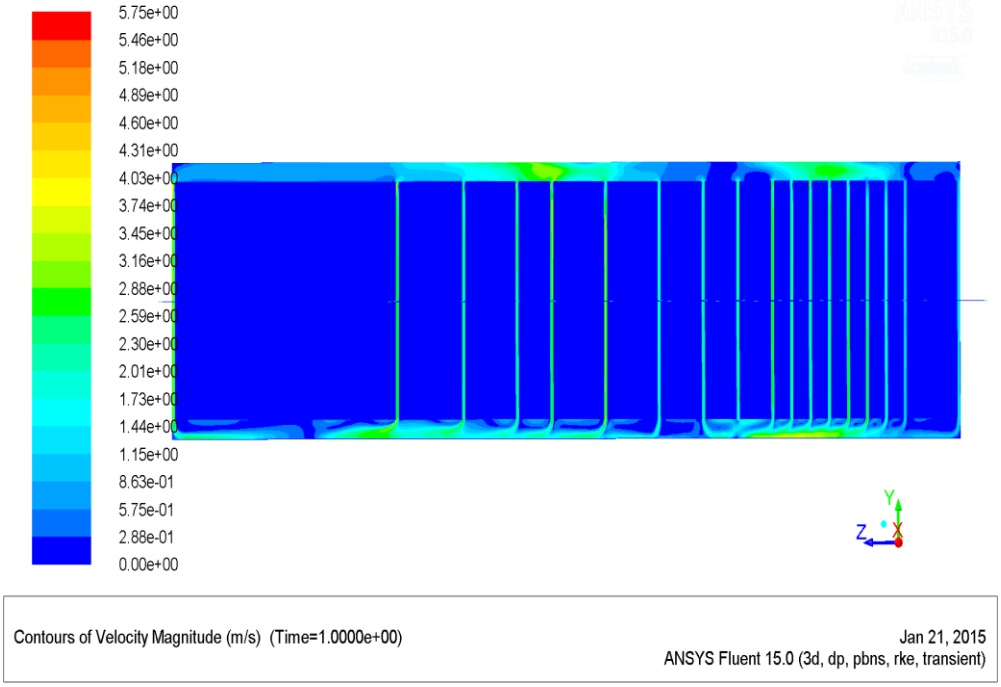

Figure 43: The figure shows the velocity contours plots for a water flow of 180 m^3/h.

1.2.6.8 Results

Table 6 presents the total pressure drop in the system and the total heat-up of water for all described cases, calculated as a difference between inlet and outlet properties. As the proper simulation with 1.0 s of pulse and 6.2 seconds of subsequent cooling does not include the manifolds, the results are taken from a steady-state simulation with constant energy deposition of ca. 300 kW.

Table 6: The table reports the final simulation results for the various cases including the pressure and temperature drops.

Case	Inlet velocity (m/s)	Δp (mbar)	ΔT (°C)	ΔT_B (°C) during the beam (ΔT x 7.2)
V0.5	0.5	11	5.7	41.0
V1	1	43	2.9	20.9
V2	2	165	1.2	8.6
V3.2	3.2	412	0.7	5.0
V2P20	2	166	1.2	8.6
V2HT	2	16	1.2	8.6

Table 7 presents the dependence of the maximum temperature difference as a function of the wall y+. As y+ values well below 1 lead to capturing the laminar sublayer to an excessive detail, meshes of 40-45 cells were deemed most appropriate for this problem. Little increase in max temperature is observed when meshes over 45 cells are used.

Table 7: The table reports the mesh dependence on y+. The highlighted columns are those representing the number of cells judged adapted to the problem.

Cells across gap	20	30	40	45	50
Average y+	6.95	2.57	0.97	0.58	0.39
Maximum y+	8.68	3.2	1.22	0.73	0.49
Minimum y+	3.64	1.33	0.5	0.32	0.19
Maximum temperature (°C) for 2m/s flow	101.4	176.3	188.3	200.1	203.3

Plots presented in Figure 44, Figure 45 and Figure 46 show the temperature evolution in the blocks over 5 pulse periods for case V1, V2 and V3.2 respectively. Obviously, for lower flows the maximum observed temperature is higher: in case of 90 m^3/h the maximum temperature 410 °C, 380 °C for a 180 m^3/h flow (comparable with the results shown in Section 1.2.5.4) and 360 °C for 290 m^3/h. Note that the plots are in absolute (Kelvin) scale.

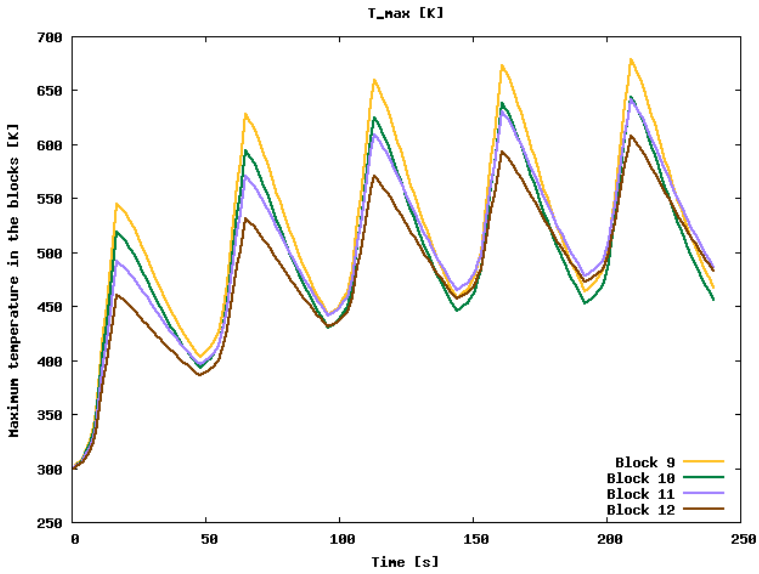

Figure 44: The figure shows the maximum temperature variation in the blocks as a function of time – case V1

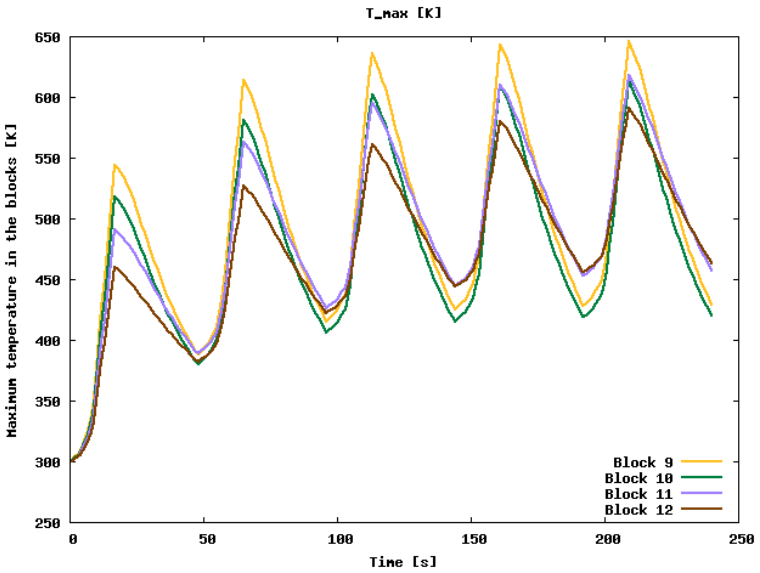

Figure 45: The figure shows the maximum temperature variation in the blocks as a function of time – case V2

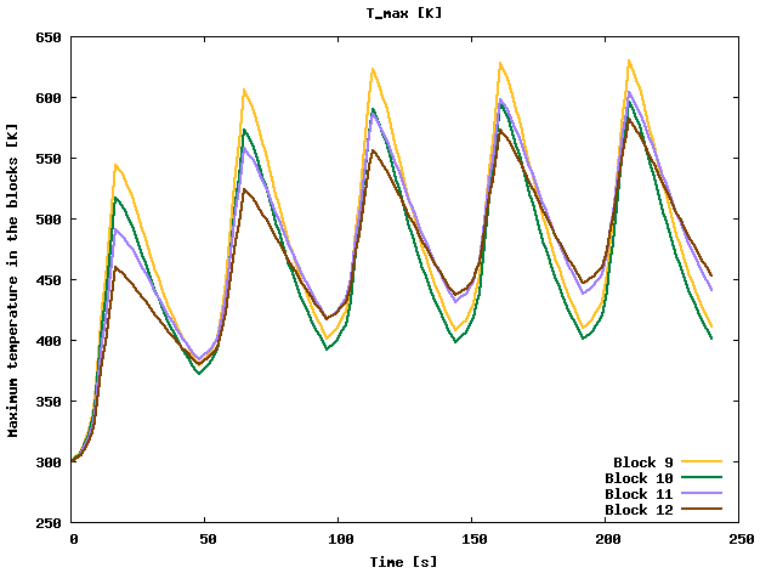

Figure 46: The figure shows the maximum temperature variation in the blocks as a function of time – case V3.2

Figure 47, Figure 48 and Figure 49 show the maximum temperature in the gaps, for case V1, V2 and V3.2 respectively. A similar trend as for the maximum temperature is observed. A temperature of 240 °C is obtained for 90 m^3/h flow, 200 °C for 180 m^3/h and 175 °C for 290 m^3/h. Again the plots are in absolute (Kelvin) scale.

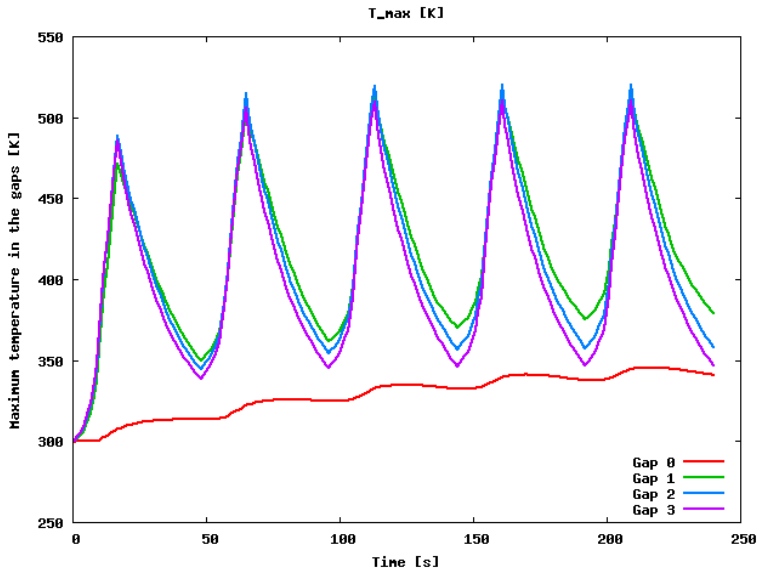

Figure 47: The plot shows the maximum temperature in the gaps (observed in boundary layer) - case V1

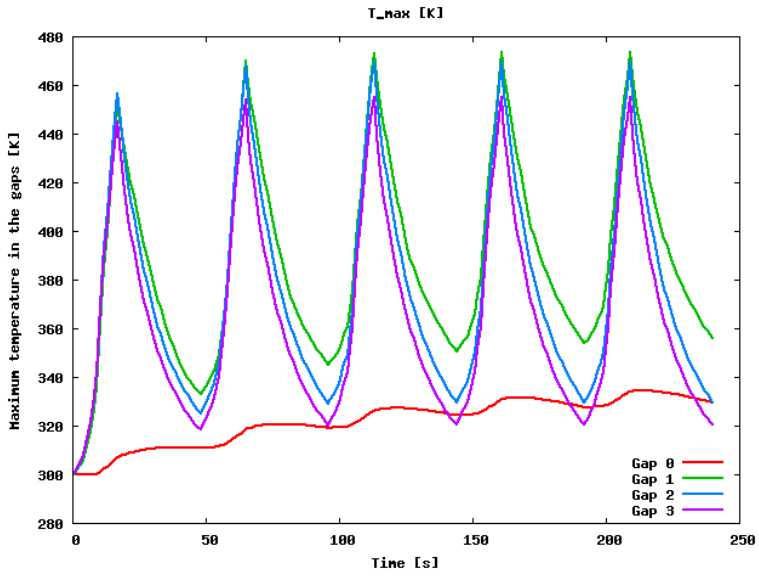

Figure 48: The plot shows the maximum temperature in the gaps (observed in boundary layer) - case V2

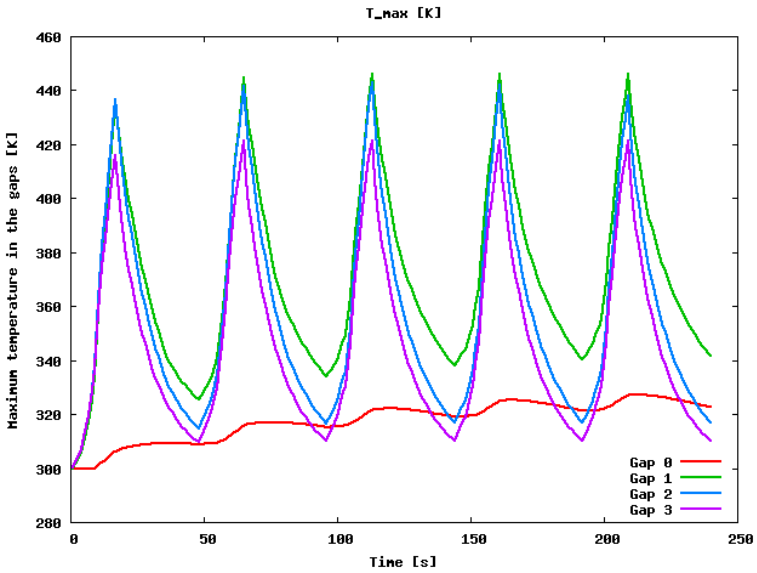

Figure 49: The plot shows the maximum temperature in the gaps (observed in boundary layer) - case V3.2

As the phase-change temperature of water at 10 bar is 180 °C, for the lower flows it would be necessary to pressurize the coolant to higher levels (evaporation temperature at 20 bar: 210°C, at 50 bar: 260°C, at 100 bar: 310°C).

Table 8 summarizes the values of the heat transfer coefficient (HTC), h, on the gap walls, obtained considering that a constant heat load of 300 kW is applied. The following formula was used in order to determine the values:

$$q'' = h(T_{wall} - T_{bulk}) => h = \frac{q''}{T_{wall} - T_{bulk}}$$

where q'' denotes the heat flux on a specific wall and T_{bulk} is the average temperature of water in the adjacent gap.

Table 8 confirms that the value of 10000 W/(m^2*K) which was assumed in Section 1.2.5 is quite conservative.

Table 8: Heat transfer coefficients calculated for case of 300 kW heat load

Block	1	2	3	4	5	6	7	8	
HTC [W/m^2]	6626	7668	11518	13839	12737	11130	11894	14134	
Block	9	10	11	12	13	14	15	16	17
HTC [W/m^2]	13755	12771	11784	12597	12634	11528	11744	14261	17085

1.2.6.9 Conclusions on the CFD part

Based on the simulation results it appears that pressurizing the water up to 10 bar may not be enough if one wants to avoid local evaporation while using a coolant flow of 180 m^3/h as reference value. It will be necessary to use pressurized water at 20 bar, or employ higher flow rates. The design of the water inlets and distribution could be improved even further with the objective of reducing the required flow rate and control the water laminar velocity, thus reducing risks of erosion.

1.3 Conceptual design of the SHiP target assembly

1.3.1 Introduction

The present section describes the conceptual design of the SHiP water-cooled production target prepared for the SHiP Technical Proposal. The design is based on all inputs coming from the thermo-mechanical and CFD analysis and includes the requirements of the SHiP experiment in terms of target length and transversal size (pion and kaon reabsoption). Preliminary handling and support fittings have been included as well.

1.3.2 Design

The target core is contained in a double walled container of stainless steel 316LN (see Figure 50).

The external shroud has 10 mm thickness for a total length of 1360 mm. The first containment will be filled with circulating helium gas at a purity of >99% in order to create an inert environment and avoid corrosion of the steel parts; an oxygen detectors in the helium circulation loop will also allow early detection of potential leakages from the internal water-containing vessel. Stiffeners and reinforcing structures are embedded in the external containment to allow handling of the entire target structure (i.e. for the fittings of the handling mushroom), which has a total (core material and structure) weight of 2.1 tons.

The inner shroud contains the pressurized water cooling circuit and the TZM and pure W blocks. The thickness of the vessel is 20 mm, in order to withstand the 20 bar pressure requested by the cooling circuit (see Sections 1.2.5 and 1.2.6). Spacers are located between the plates in order to maintain the 5 mm gaps between the plates and act as stiffeners for the inner shroud.

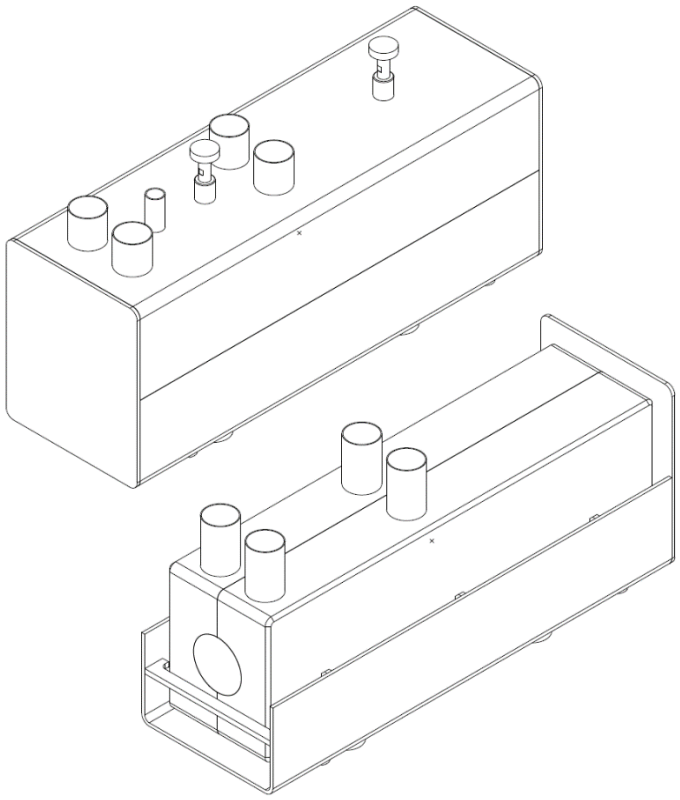

Figure 50: Isometric view of the SHiP target assembly. The top figure shows the target external containment with handling fittings and the water and helium gas fittings, while the bottom one shows a cut-view of the assembly, with a view on the inner pressurized shroud.

Figure 51 shows a transversal view of the target assembly, clearly showing the external shroud (10 mm thick) and the thicker (20 mm) inner one. The TZM and tungsten blocks are fitted in the inner shroud, which is composed by two halves electron beam welded together.

As shown in Figure 52 (and also in Figure 50) the upstream beam window has a round shape of 160 mm diameter in order to avoid having the primary proton beam painted onto the electron beam welded part. As discussed in Section 1.2.5.7, this beam window could be made by SS316LN or by ferritic T91.

We have also take into account the feasibility of the target core plates. Both TZM and tungsten blocks are therefore constituted by an inner fully forged cylinder of 150 mm diameter with a varying length, according to Table 2, and by two halves made by sintered material. Being roughly 100 mm the longest piece feasible by double forging, the last tungsten block of 350 mm is constituted in fact by 4 blocks of 87.5 mm and assembled without gaps, with a special shape to accommodate the stiffeners embedded in the inner shroud.

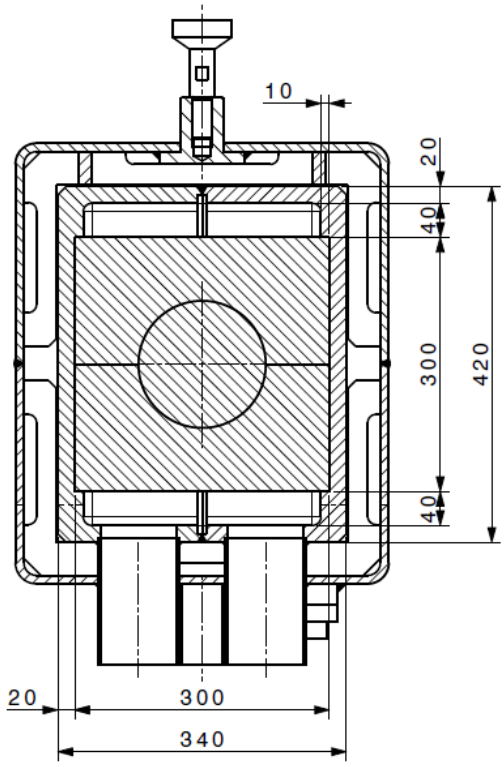

Figure 51: Transversal view of the SHiP target assembly.

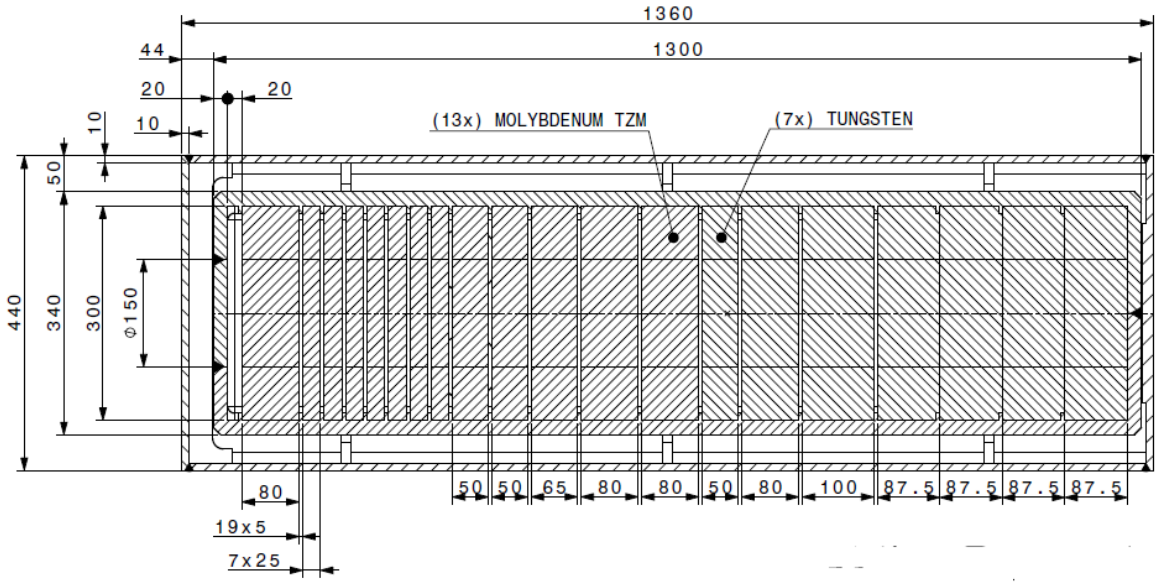

Figure 52: Top view of the SHiP target assembly cut at the level of the beam axis.

Mushroom-type (CNGS-type) handling fittings have been included, taking into account the position of the centre of gravity of the whole assembly. Three supporting feet have also been added to the bottom of the target assembly, in order to allow for a precise alignment of the target on the supporting plate (see Figure 53 and Figure 54, and Section 2.4.2 for handling specifications). All the connections (water and helium gas) of

the SHiP target shall be of plugin type and done one the bottom of the target. A pre-guiding system will be implemented in order to pre-position the target on the supporting table during the handling phase. This pre-guiding system shall be compatible with the water and helium gas plugin system.

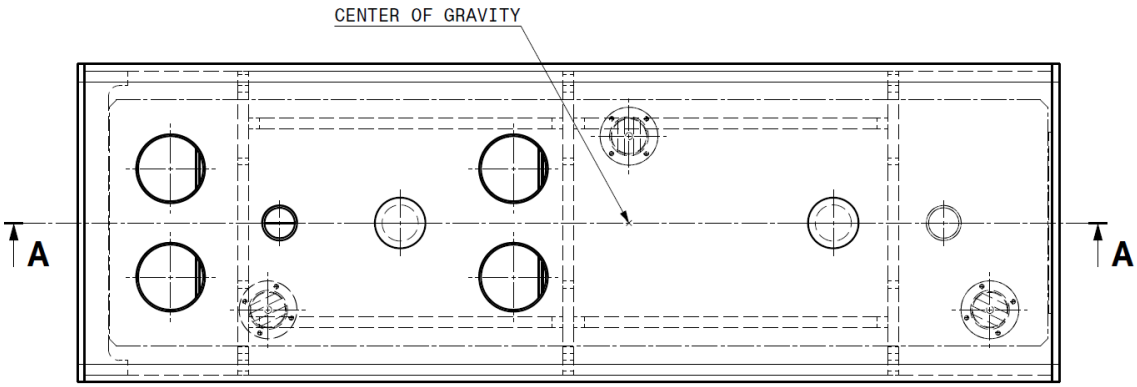

Figure 53: Top view of the SHiP target assembly.

The overall view of the target assembly is shown in Figure 54. A 6 mm gap between the inner and outer containment is left in the downstream part, in order to minimize the area without high-density material.

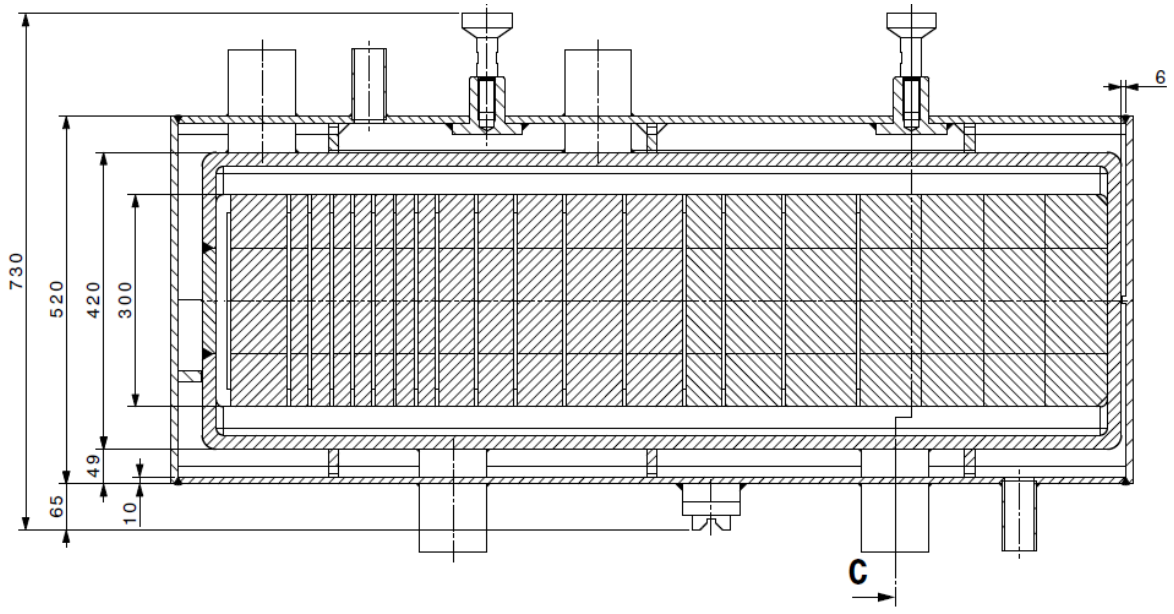

Figure 54: Overall Lateral view of the SHiP target assembly, showing the inner core, the internal containment, the external one, the inlet (top) and outlet (bottom) water and helium pipes, the handling mushroom fittings and the support feet.

It is worth mentioning that pressurized helium could be considered as a possible coolant as well: at this phase of the CDR it was discarded due to time limitations and the higher amount of experience in the cooling and ventilation group with water cooling solutions. Using helium would have the advantage of having a lower viscosity resulting in low probability of pipe erosion, which could be an issue for water under high velocities,

considering the very small pipes. A helium-cooled target will be preferable also from a radiation protection point of view, as it would avoid reducing the risk of circuit pollution with spallation products and avoid the formation of higher mass products such as ^{7}Be and short lived carbon and nitrogen isotopes.

1.3.3 Instrumentation

The SHiP target assembly will be equipped with thermocouples for each of the target plates – interlocked with the primary beam – in order to detect any abnormal operating conditions. "Halo thermocouples" (see Ref. [11]) could also be foreseen to detect any abnormal halo condition of the primary proton beam impact on the target front face.

In order to continuously monitor the beam shape on target, we can foresee the possibility to implement a target imaging system with a luminescent Al_2O_3:Cr coating, on the external containment, similar to what is used for the Spallation Neutron Source at Oak Ridge National Laboratory [12] and for the LHC beam dump [13]. Considering the extremely high prompt and cumulated dose expected for SHiP, a solution similar to [12] should be considered. The photons generated by the protons impacting on the coating will be reflected upward from a convex mirror to a less radioactive area, where fiber bundles made by radiation hard optical fibers transfers the image to the target hall where a CCD camera collected the image.

1.4 Spallation material issues and R&D

Based on preliminary simulations involving a spallation target split into a Mo based and a W based portion, respectively, the suitability of these metals and of their alloys has been considered. Starting from the available physical and mechanical properties, it has been checked whether the above materials can guarantee sufficient strength (the most severe stresses are in compression, up to ~380 MPa for Mo and ~315 MPa for W, respectively) in the temperature ranges experienced by the target (up to 400 °C for Mo and ~300 °C for W). The above figures arise from the results of the simulations summarised in Section 1.2.5.

It is worth to be mentioned that the spallation materials will experience several million cycles of thermo-mechanical fatigue, hence fatigue strength also has to be considered.

1.4.1 Mo and Mo-alloys

Pure Mo, independent of its temper state, has limited high T yield/tensile strength at or above 350 °C [14]. Moreover, its fatigue strength is only 70 % of its tensile strength at 400 °C, which in turn is under 400 MPa at this temperature [14]. Data on yield strength in compression are scarcely available. From data on creep strength at 540 °C, usually measured in compression, static creep strength of recrystallized Mo might be limited to some 300 MPa at 540 °C for short time exposures [14]. Pure Mo in specific tempers features higher yield/tensile strength; namely stress-relieved Mo features much higher strength than recrystallized Mo (yield and tensile strength at 400 °C are in the order of 450 MPa and 500 MPa, respectively for the first temper [15]). The stress-relieved temper should be preferred for Mo as well as for its alloys.

The effect of neutron irradiation on pure Mo (integrated fluence of 10^{21} n/cm^2 – of the same order of magnitude of the SHiP case (see Section 1.2.4.2) – to 10^{22} n/cm^2, irradiation temperature between 400 °C and 450 °C, test T = 300 °C) is a general loss of tensile ductility compared to the unirradiated state [16], with embrittlement occurring particularly for the highest 10^{22} n/cm^2 exposure for the tempers tested.

Among the Mo-alloys, one of the most available commercially and largely tested is TZM (Titanium-Zirconium-Molybdenum). In the unirradiated state, TZM features higher strength and ductility than pure Mo for both stress-relieved and recrystallized tempers in a wide T range up to 1600 °C [15].

Figure 55 shows that for irradiated TZM at 500 °C with an integrated neutron fluence of 1.2*10^{22} n/cm^2, the yield strength is further increased for a wide range of strain rates. The blue dashed line corresponds to the strain rate expected for the SHiP operating conditions, evaluated to be around 10^{-3} s^{-1}.

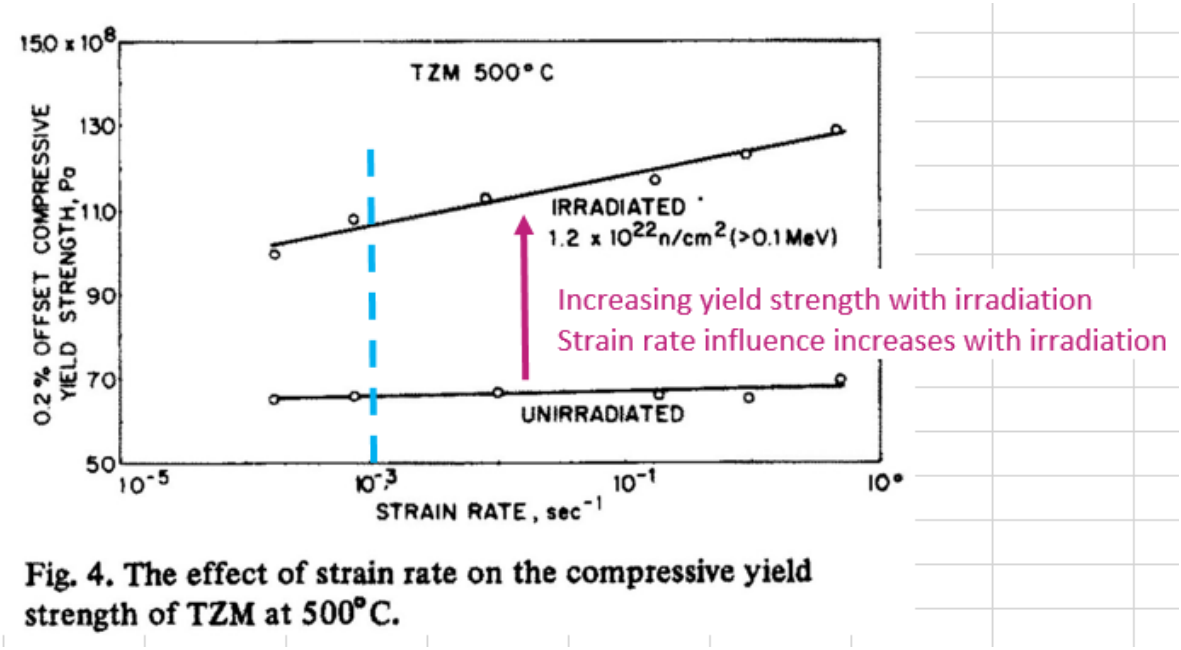

Figure 55: The figure shows the yield strength of TZM at 500 C, which increase with irradiation for a wide range of strain rates (SHiP target operates with a strain rate of around 10^{-3} s^{-1}, indicated by the vertical blue dashed line).

Isothermal fatigue of TZM, measured in the range 350 °C - 500 °C, shows a fatigue life of 10^4 cycles, for a symmetric tensile/compressive stress range above 700 MPa [17]. Stress relieved temper is also to be preferred for TZM. Combined thermo-mechanical fatigue tests would lead to lower strength. Irradiation increases strength and reduces ductility in a wide T range, but above 200 °C some residual ductility is featured [18].

TZM shows also improved fatigue strength when irradiated in a vacuum compared to the unirradiated condition [19]. Based on data from tests at 427 °C for a neutron irradiation of 10^{22} n/cm^2 measured up to some 10^6 cycles, this alloy could be a candidate

to check its strength in the several million fatigue cycles ranges and conditions representative of the SHiP experiment (see Figure 56).

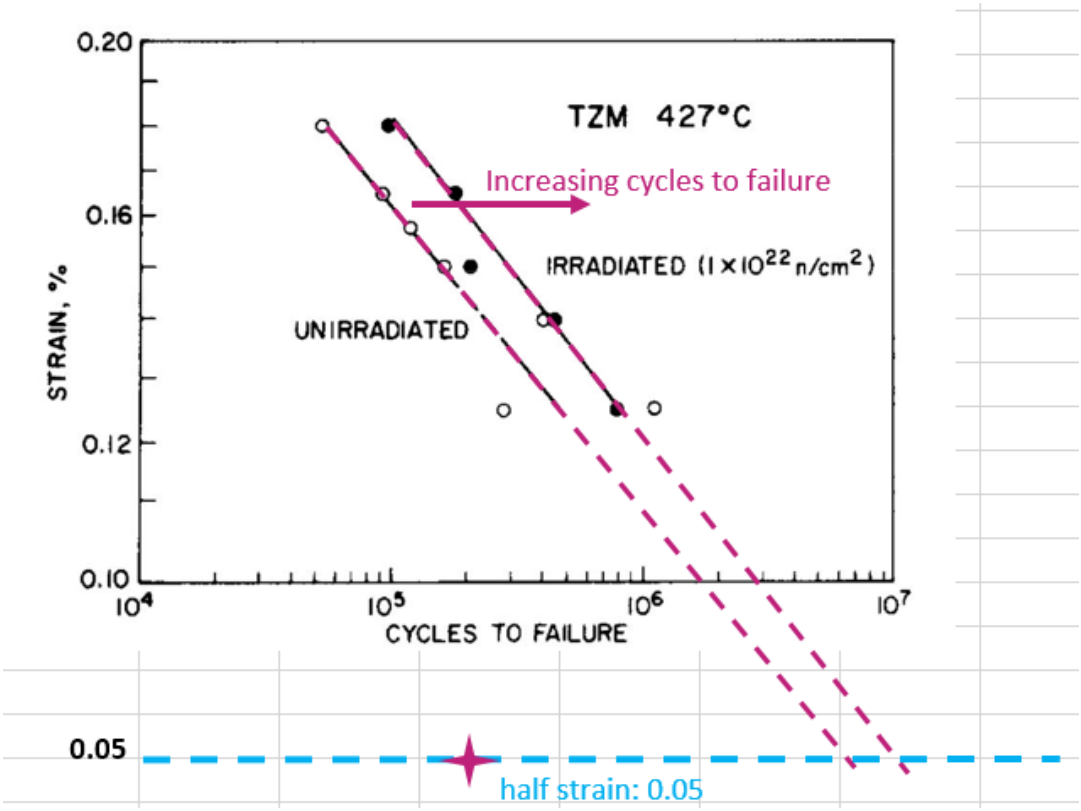

Figure 56: The figure shows the effect of irradiation on TZM fatigue at 427 °C as a function of half strain %. The trend of the data for lower strains shows that for the SHiP target case, the fatigue occurs at more than 10^6 cycles for both irradiated and unirradiated state [19].

For the testing conditions applied by Smith and Michel [19] and based on an extrapolation from fatigue data for the above-irradiated alloy, a level of total strain per half cycle in the order of $0.7 \cdot 10^{-3}$ might be withstood by irradiated TZM with a crack extension within 1 mm. The strain rates due to the thermo-mechanical cycling of the target (estimated in the order of 10^{-3} s^{-1}) should not exacerbate the brittleness of this alloy.

1.4.2 W and W-alloys

Pure W is available in different product forms including rolled plates (thickness usually up to 20 mm), billets and forgings that are relevant forms for our application. Rolled plates can feature a fully dense microstructure but the microstructure is layered hence strongly anisotropic. Flat grains parallel to the rolled surface affect the mechanical properties and result in a potential risk of delamination [20]. Double-forged (radially then axially) W blanks feature a more isotropic microstructure than unidirectional forged shapes. It is considered by the fusion community that double-forged W "should act as a reference grade for establishing a reliable materials database for finite element calculations" [20].

Relevant data in the literature on mechanical properties of neutron-irradiated tungsten are limited. The effect of irradiation (neutron fluence up to $0.9 \cdot 10^{22}$ n/cm^2 with E > 0.1 MeV) on static tensile properties is an increase of yield strength (up to 1100 MPa at 400 °C) but at the expenses of elongation, particularly for the low T range [18]. These results have been assessed on small diameter (6.3 mm) stress relieved rods. Information on the thermal fatigue resistance of W components "is limited to the experience obtained in two irradiation campaigns for ITER" (neutron doses of 0.15 dpa and 0.6 dpa at 200 °C, respectively). The results obtained indicate that, at the above neutron doses, the material changes occurring in W "do not have any significant influence on the component's performance" [20].

Despite these positive results, "the use of tungsten in any highly stressed component at low temperatures < 500 °C" is considered "to be avoided" [21].

Additional studies on pure W (and Mo) with a 120 keV hydrogen beam have been carried out at the Neutral Beam Test Stand (NBTS) at IPP, Nagoya University utilizing hydrogen ion beams as an energy source to heat samples (75 A ion source producing heat flux up to 20 kW/cm^2 for 1 s) [22]. The W in this case was obtained by powder metallurgy and forging. Thermal shocks were applied. The resulting thermal cyclings were such that the upper temperature did not exceed the recrystallization temperature of tungsten and the lower temperature was below its DBTT. Micro cracking was observed, eventually evolving into cracking. Cracks induced by residual stresses are also a concern with W. Ductility is one of the most important factors in determining the thermal fatigue lives. Ductile–brittle transition temperature (DBTT) should always be exceeded.

Concerning W alloys, W-Re alloys have the advantage of featuring higher recrystallization T and lower DBTT compared to pure W and preserve ductility after recrystallization [23]. The effect of additions is significant above 3 %. Addition of Re towards the lower end (W–3–5% Re) provides a favourable effect on the ductility in the non-irradiated state, but under neutron irradiation it "results in more rapid and severe embrittlement than it is observed for pure W" [20]. High Re activation is also expected under neutron irradiation [24].

Particle strengthened W alloys (e.g., W–1% La_2O_3) were submitted as plasma-facing materials to 1000 "cyclic steady state heat loads" at power densities up to 18 MW*m^{-2}. "Less mechanical strength and an increased loss of ductility compared to pure W was found for particle strengthened W alloys" such as W–1% La_2O_3 "when tested up to 700 °C" [20].

An exception cited "among all explored tungsten alloys" is mechanically alloyed W–TiC "that showed no irradiation hardening as measured by Vickers hardness at 600 °C", "better machinability and improved ductility compared to pure W" [20] (for the latter, limited machinability and ductility are a major concern). The addition of TiC allows for an isotropic and fine grain structure that is maintained even in the recrystallized condition. Moreover, "after recrystallization, the finer dispersoids of TiC particles improve the low temperature impact toughness of refractory alloys following low-dose

neutron irradiation". This alloy is mentioned as more expensive than pure W [20]. Ultra-fine grained W–TiC is currently developed for use in irradiation environments (additions in the range 0.25–0.8 wt% TiC) [25]. Preliminary investigations indicate that W-TiC is not yet available on industrial scale.

1.4.3 Conclusions

In conclusion, for Mo-based components the use of a Mo-alloy should be preferentially considered with respect to pure Mo. TZM is a promising candidate. Nevertheless, the most available fatigue data for this alloy are for reverse bend cycles or tensile, not for pure compression; moreover DBTT might be unfavourably affected by our low T irradiation conditions. As previously mentioned TZM is therefore chosen as baseline material for the first half of the SHiP target.

For W components, from fusion literature for plasma facing applications, use of W at low temperatures < 500 °C is considered as to be avoided. Our conditions are probably much less critical in terms of T gradients, strain rates, flux heat factor… but the machinability of W is critical, and the embrittlement by residual stresses might be an issue. Selected W alloys such W–TiC could be considered and tested, pending availability.

An extensive and dedicated testing campaign based on relevant irradiation and thermal fatigue conditions is in any case recommended to confirm the feasibility of the spallation target with the above materials and proceed towards and Technical Design. Based on the above considerations, two candidates that could be preferentially tested are stress-relieved TZM and W–TiC, respectively, in as received and irradiated conditions. For comparison, stress-relieved pure Mo and pure W should be added to the testing matrix.

Fabricability of the refractory metal blocks to the required shape should also be addressed (forgeability or formability, achievable dimensions/shape, machinability…).

The mechanical testing suite should at least include:

- Tensile and compression curves for irradiated and non-irradiated conditions in the relevant T range
- Fatigue (Wöhler-type curves in compression and wherever necessary in tension for the surface portion of the target disks mainly solicited in tension), as above
- In case, fracture mechanics tests (FCGR, KIC), as above
- Impact toughness to assess the DBTT, as above

Moreover, coatings against possible corrosion/erosion should be considered (refractory metals do generally feature limited resistance to erosion-corrosion in cooling waters), considering the high flow rates and laminar velocities expected in the gaps between the target plates. The feasibility of a Ta-based or an equivalent anti-corrosion coating on disks of relevant geometry for the application should be addressed through dedicated

order to companies. The coatings should then be the object of micro optical inspections and characterisations at CERN.

The effect of irradiation, fatigue and tensile stresses on the coatings and their adherence to the TZM or pure W substrate should also be addressed.

An erosion corrosion test in a loop and in conditions as close as possible to the ones of the application should be carried out on representative coated samples, either at CERN or with the help of a partner laboratory. The test should be followed by microstructural characterizations in order to check and quantify possible corrosion events; electrochemical tests should also complement the above campaign.

2. Considerations for the SHiP target complex

2.1 Introduction

This chapter describes the conceptual design of the SHiP target complex.

The main characteristics of the proposed target station are briefly discussed, including the target bunker and its helium enclosure, the inner target area and associated supports as well as its water-cooled proximity shielding. The various alcoves and underground areas supporting the operation of the complex are described.

A specific section is dedicated to remote handling aspects of the target assembly and of the proximity shielding, due to the very high residual dose rate expected for these equipment.

2.2 Design of the target complex

2.2.1 Introduction

Due to the specificities of the physics case, the SHiP experiment will require the realization of a new dedicated target complex in the Prevessin area. The envisaged complex has been designed in order to be a multipurpose one, i.e. to be able to exchange target and shielding configuration around the target in the case future experiments would require so.

The SHiP target complex design has profited from the work performed in the framework of the CENF Neutrino Facility (CENF) target facility. The design is adapted for shallow target installation, and is based on a multi-compartment solution in which volumes are well subdivided (from the ventilation point of view) and are constituted by underground areas accessible from a surface target hall.

2.2.2 Target complex conceptual design

The SHiP target hall is designed as a surface (or semi-underground) building roughly 40 meters long and 30 meters wide, for a height of ~15 meters. The target building includes also the first part of the active muon shield (15 meters long). Figure 57 shows a top view of the SHiP target hall, with a view of the various underground areas foreseen for the operation of the experiment, which will be accessed from the target hall.

The SHiP production target is located underground, on the bottom of a shielded bunker, assumed 10 meters long and 8.5 meters wide, for a total depth of about 12 meters with respect to the surface of the target hall. An underground cast-iron hadron absorber encloses the production target, with the double objective of absorbing the remaining hadrons emerging from the target and the non-colliding protons and to significantly reduce the radiation exposure of the muon shield, which separates the target bunker from the experimental hall.

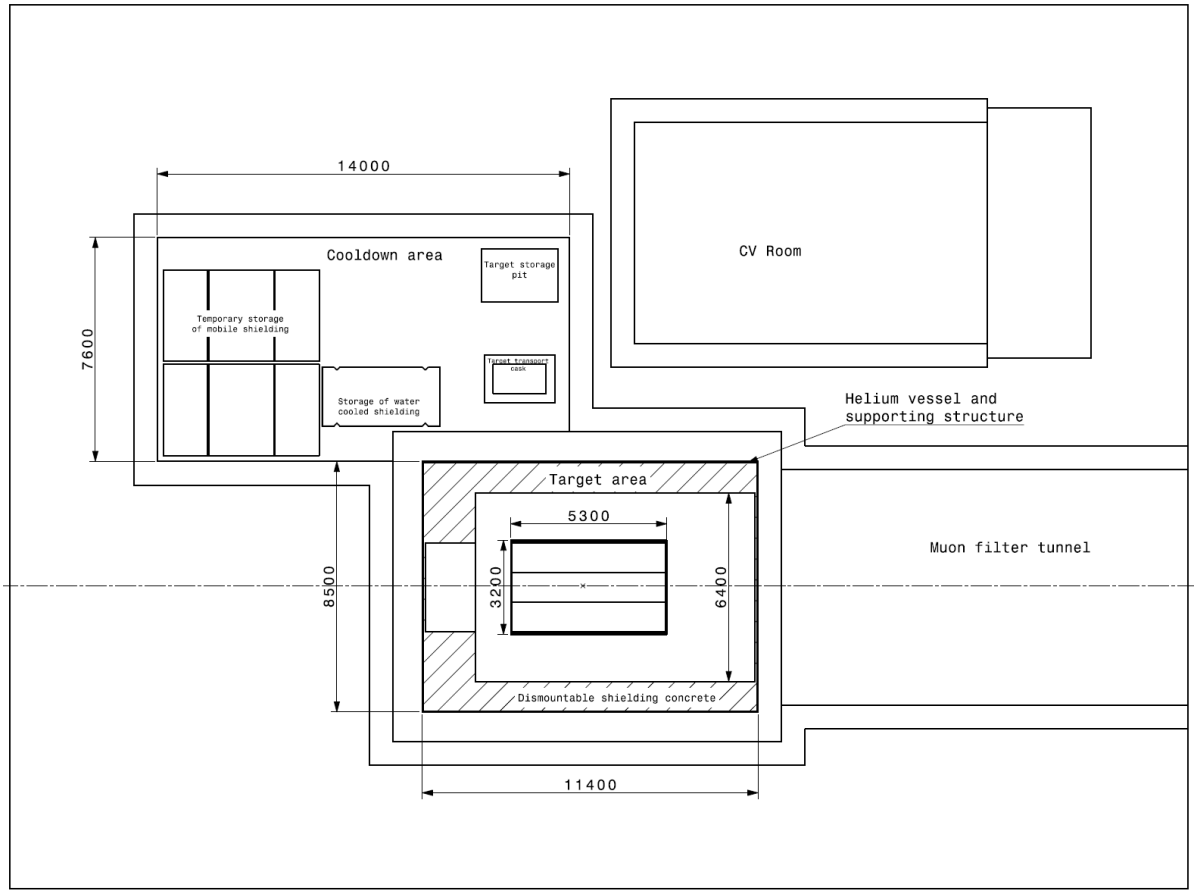

Figure 57: The figure shows a top of view of the SHiP target hall with the configuration and dimensions of the various underground areas.

A cool-down area, roughly at 5.6 meters below the floor of the target hall is foreseen to allow the temporary storage of radioactive equipment needed for the opening of the target bunker in case of failure of either the SHiP target or the proximity shielding. Similarly, a shielded underground area is foreseen for the installation of the target and proximity water cooling systems as well as for the helium circulation and purification circuit (see Section 2.3.3).

A helium-vessel containing high purity helium gas (>99%) at atmospheric pressure encloses the SHiP production target and the iron shielding, with the double objective of protecting the equipment from radiation-accelerated corrosion as well as to avoid the production of high-mass activation products.

In order to minimize the radiation streaming towards the primary beam line, the primary beam opening must be kept as small as possible, but still of the same order of magnitude as the target transversal dimensions. A TAN-like system, installed in the primary area, will have to be designed to reduce the activation of the primary tunnel equipment due to neutral radiation (essentially neutrons and photons) travelling backwards from the target to the primary beam pipe. A fixed collimator will be foreseen in the first part of the target bunker shielding, in order to protect the fixed and water-cooled cast iron as well as the target against uncontrolled primary beam.

The envisaged shielding configuration is such as to avoid radiation activation of the concrete fixed civil engineering structures, which would allow for a much easier change of scope of the installation (i.e. for new experiments) as well as for the dismantling phase.

The SHiP target complex ventilation system will be designed taking inspiration from the ISO17873:2004 norm [26] and will be validated by the CERN's HSE unit, according to the Ventilation Working Group (VWG) recommendations [27]. A pressure cascade between the various compartments, from -60 Pa (with respect to the outside environment) of the target hall to roughly -200 Pa for the most exposed zones shall be foreseen, at least during beam operation. A recirculation system for the most radioactive zones (areas contiguous to the helium-vessel) should be foreseen to allow for the decay of short-lived isotopes before release into the environment. The air-tightness of the various areas will be a central part of the target station design and will be interlocked with beam operation. It is worth noticing however, that with the present helium environment around the production target, the issue of air activation will be significantly relaxed with respect to the CENF design, despite the higher beam power.

The civil engineering design is described more in detail in Ref. [28].

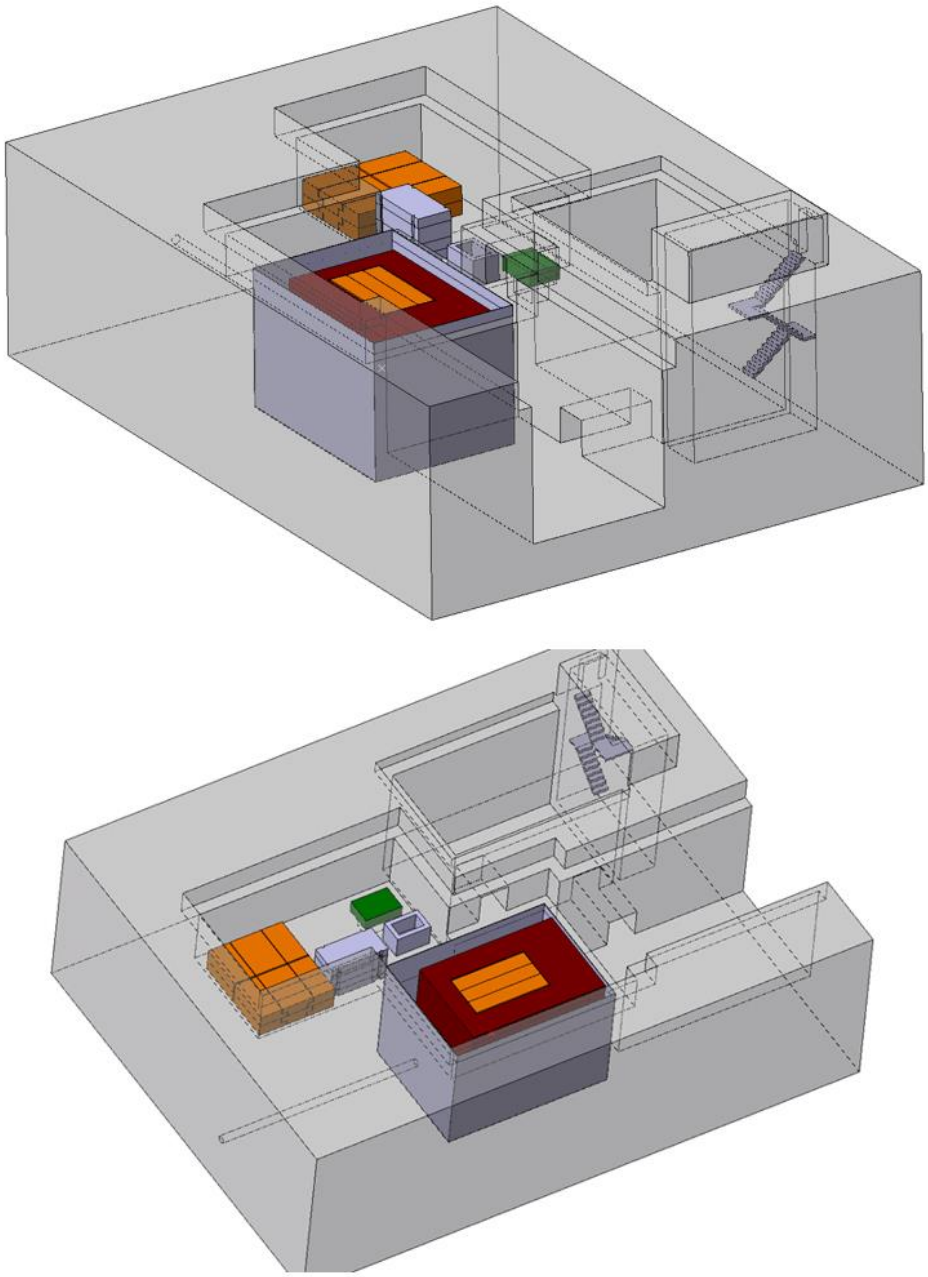

Figure 58: Isometric views of the proposed design of the SHiP target complex. In dark red the fixed cast iron blocks, in orange the specially designed blocks for material access the production target zone. The green shielding block protects the spent target storage zone. The storage area allows for the storage of a spare/spent proximity shielding assembly, for the storage of the removable blocks as well as for the storage of the spent target cask, employed to move the spent target away from the target hall.

2.2.3 Design of the underground target bunker shielding

The design of the target bunker has been the subject of extensive discussions and iterations, in order to optimize it for what concerns costs, radiation protection considerations, handling and feasibility taking into account external constraints.

Figure 59 and Figure 60 show, respectively, a longitudinal and transverse view of the area around the target bunker.

The shielding around the production target is composed by a water-cooled cast iron layer (so called "proximity shielding", see Section 2.2.4) and a fixed cast iron part. Considering the high residual dose rate that will be reached due to beam operation, the design of the former has been optimized in order to minimize the number of blocks and to have the easiest possible remote handling system (see Section 2.4). The entire shielding is 60 cm thick, 400 cm long and 280 meters high and is divided in four blocks.

The latter is on the contrary composed by "standard" passive cast-iron blocks, piled in order to constitute a 200 cm shielding towards the side, for a total length of 1120 cm and a height of 760 cm. A reduced amount of iron shielding is present upstream the target (see Figure 59). Figure 61 shows an isometric view of the fixed cast iron bunker.

In order to guarantee easy access to the target, a removable mobile shielding – optimized for radiation protection considerations) is present on top of the water-cooled blocks (see Figure 62). Their configuration is such as to reduce radiation streaming to the top of the target bunker and therefore minimise prompt dose rate on the top of the target hall.

The remaining gap between the shielding and the He-vessel structure will be filled by removable concrete blocks.

The present shielding design is adapted to the beam power foreseen for the SHiP experiment (see Table 1). However, it presents some margins that – if exploited (i.e. exchange of the mobile concrete blocks to iron blocks) – would possibly allow the increase of power delivered to the SHiP target complex shall the SPS allow for an increase of beam intensity/power. The shielding will probably have to be reviewed and in any case confirmed by dedicated calculations of the radiation protection group.

Discussions with the CERN's radiation protection group indicate that it would be important to study the possibility to reuse the radioactive blocks presently in storage at CERN, which come from the dismantling of facilities and other target areas (i.e. T1, T8, T9, WANF dump, etc.). No significant advantage in terms of costs are to be envisaged in the short term with respect to new blocks (decontamination, repainting, fitting of handling tools, etc.), but it should be considered as a long-term capital and strategic investment and would avoid the creation of an increased amount of activated shielding blocks.

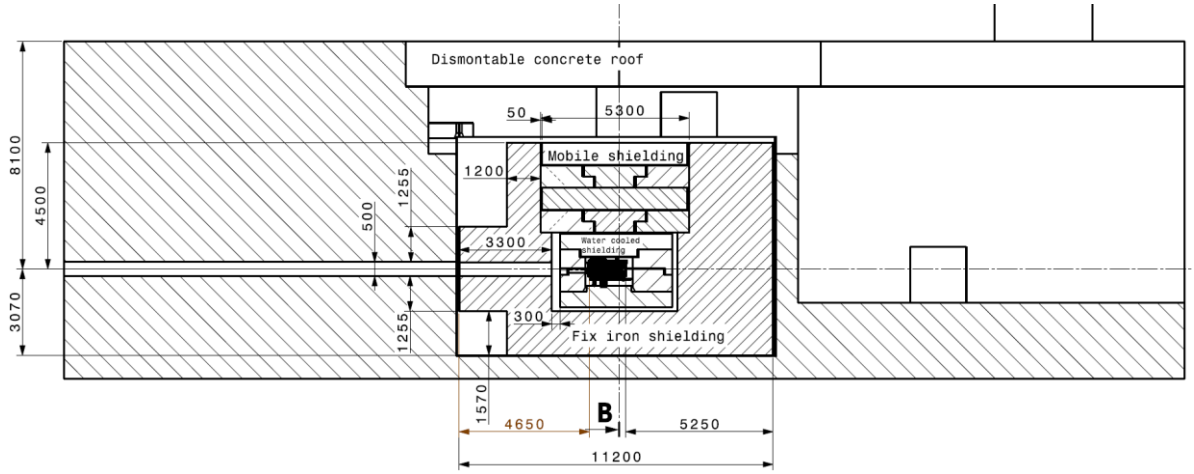

Figure 59: Longitudinal view of the target complex underground areas at the level of the beam axis.

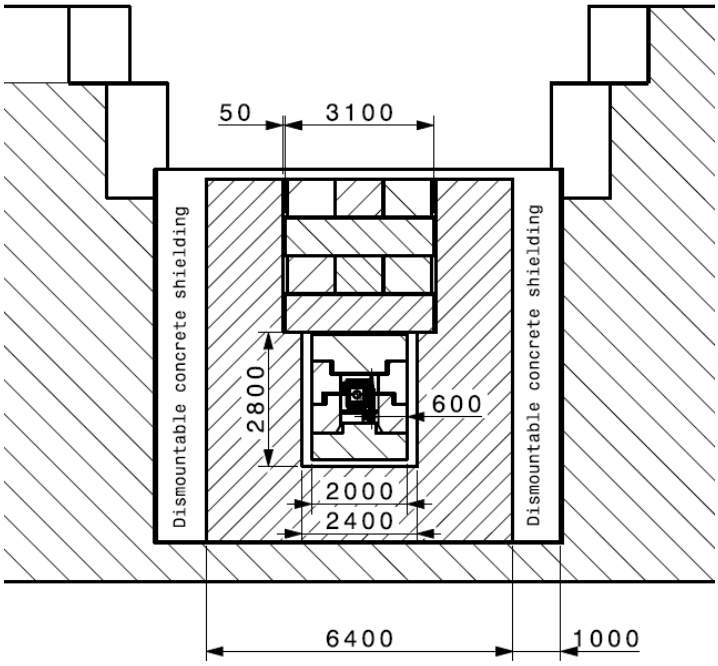

Figure 60: Transversal cut of the target bunker at a longitudinal position corresponding to the production target.

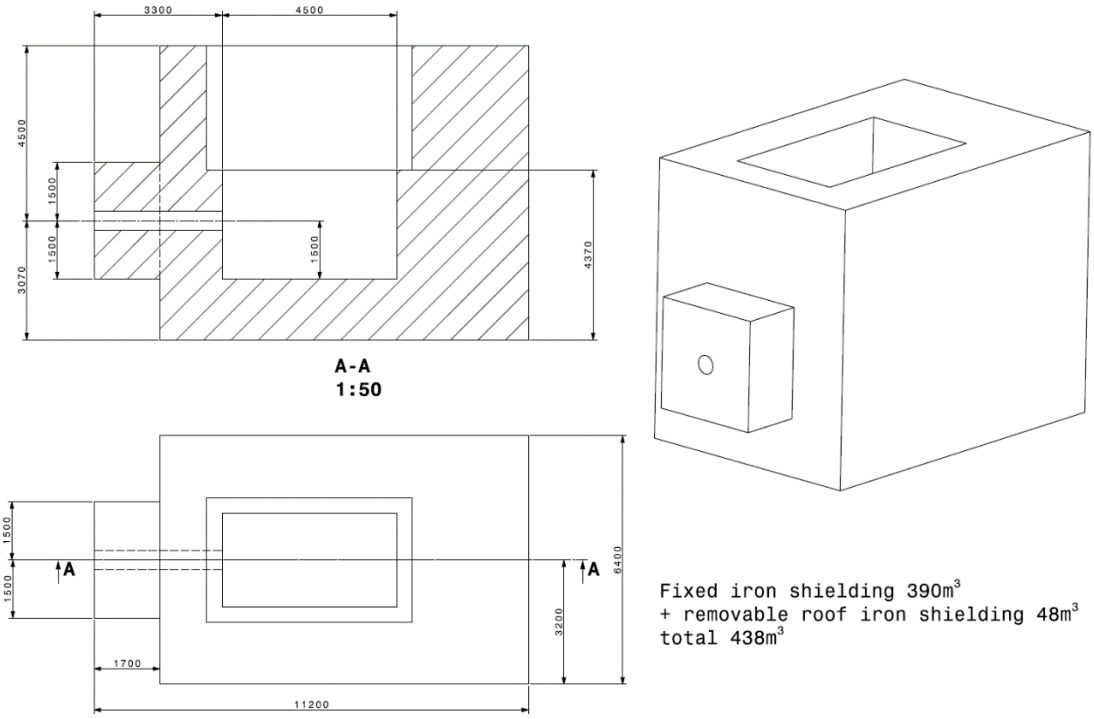

Figure 61: Isometric view of the global volume cast-iron shielding around the SHiP production target (390 m^3, corresponding to roughly 2810 tons).

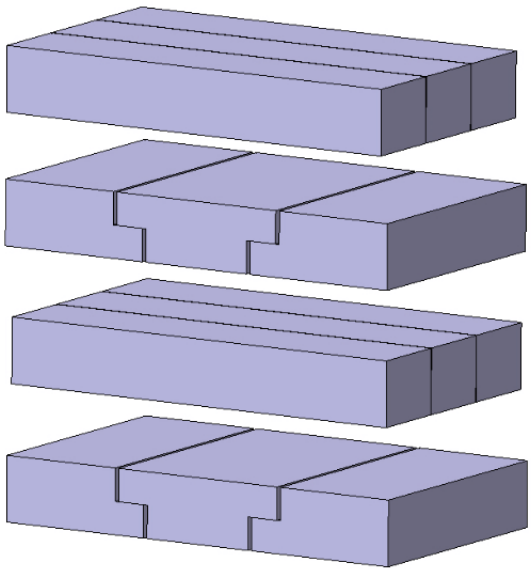

Figure 62: Design of the mobile cast-iron blocks on top of the proximity shielding (total volume of 48 m^3, roughly 346 tons). Its shape is compatible with full remote handling as well as optimised in terms of radiation protection aspects (reduction of streaming towards the surface).

The thickness of the fixed concrete around the target bunker and the distance from the raw soil will be defined at a later stage of the project and dependent of the foundations

design, but it is estimated to be in the order of 2-3 meters. The minimum concrete thickness from a radiation protection point of view amounts to 1.5 meters [29].

2.2.4 SHiP target proximity shielding

The underground proximity shielding, which surrounds the SHiP target, is the most exposed element in terms of energy deposition and radiation after the production target. Dedicated energy deposition and thermo-mechanical calculations have been performed in order to validate the design and the configuration. Results indicate that a water cooling system will be needed for removing the heat deposited by secondaries produced in the SHiP production target.

The design of the proximity shielding has been optimised in order to reduce the number of blocks while maximizing the weight (36 tons maximum) to be compatible with the crane of the target area (see Section 2.4.3). Four cast iron blocks are foreseen, one piling on top of the others with guiding supports on the side and conical fittings for final positioning. The total size of the shielding is 2 x 2.6 x 4 m^3, for a total volume of roughly 18 m^3. Those blocks will be equipped – as for the SHiP target – with a series of plugin systems, in order to pass the water in between each block.

Figure 63 shows the present design of the four proximity-shielding blocks, while Figure 64 represents the operating configuration with the SHiP target installed in the centre. According to the present design, the distance between the end of the SHiP production target and the proximity shielding is 250 mm, as dictated by handling requirements.

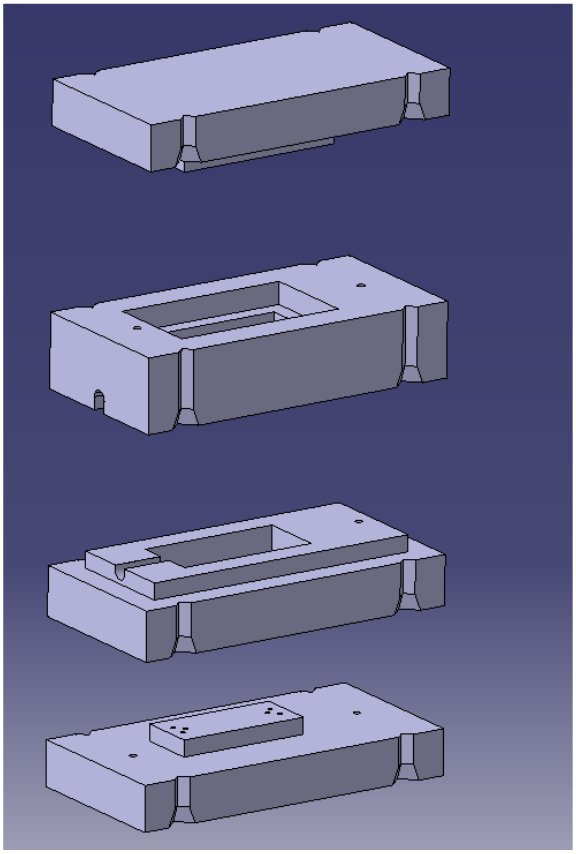

Figure 63: The figure shows an exploded view of the four proximity shielding blocks, piling one on top of the other. The bottommost block supports the SHiP target and will also provide the required services (cooling medium and electrical connections).

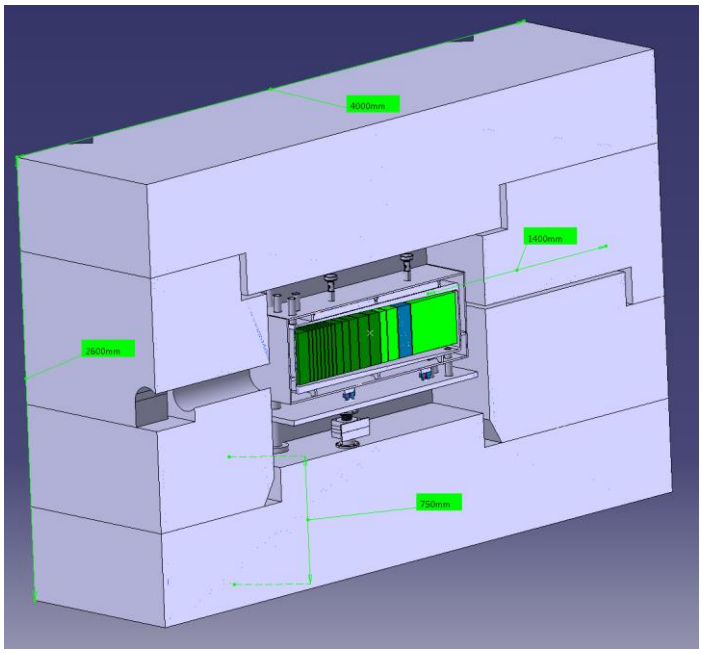

Figure 64: The model represents the SHiP proximity shielding blocks in place with the SHiP target located in the middle.

2.2.4.1 Energy deposition

FLUKA Monte Carlo [6] [7] calculations have been performed in order to evaluate the total energy deposited on the proximity shielding blocks.

Results indicate that the total deposited energy is 183.7 kJ/pulse, with 28.2 kJ/pulse deposited on the bottom block, 73.8 kJ/pulse in the bottom-middle block, 47.4 kJ/pulse in the top-middle block and 34.3 kJ/pulse in the top block.

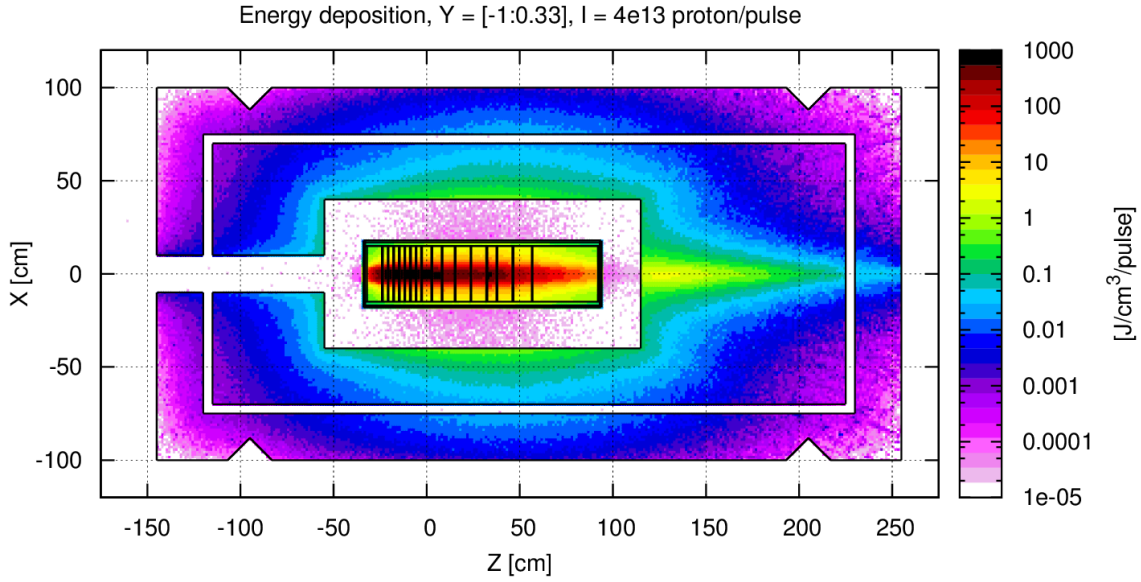

Figure 65: Top view of the energy deposited per pulse (in J/cm^3) in the proximity cast iron shielding, averaged around the beam axis on the vertical plane.

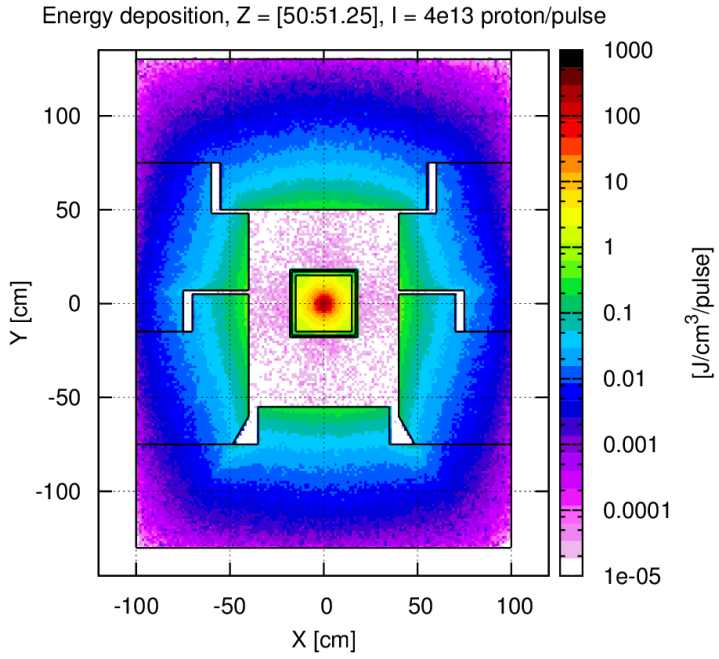

Figure 66: Transversal cut of the energy deposited per pulse (in J/cm^3) in the proximity cast iron shielding, averaged around 50 cm on the longitudinal direction.

2.2.4.2 Thermo-mechanical analysis and design of cooling circuit

Considering the energy deposited on the proximity shielding blocks and the supercycle-average power of 25 kW, the blocks need to be actively cooled. A solution based on water pipes embedded in the cast iron has been envisaged.

The piping systems are composed by horizontal serpentines of 2 cm diameter for each of the four blocks, with inlets and outlets on the same side of the shielding.

During the assembly phase, the pipes will be connected together by some "fast connections" in the way that there will be just one common inlet and outlet for the whole water system. The geometry used for the simulation is shown in Figure 67.

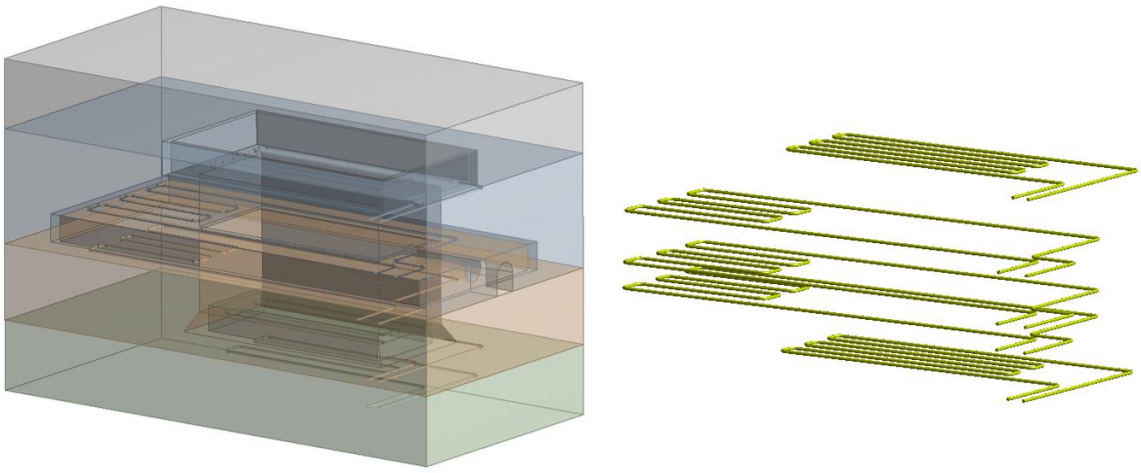

Figure 67: Shielding blocks and water piping system geometry for the ANSYS model (left) and water serpentines (right)

The total power deposited on the blocks is of 25 kW. Considering the thermal inertia of the system, in the present simulation scenario only the steady-state case is taken into account. The heat transfer coefficient used for the pipes surfaces has been assumed to be 1500 W/(m^2*K) and with inlet water temperature of 25 °C. These values are typical for a flow of water at atmospheric pressure and velocity around 0.25 m/s. The total flow required is hence 23 l/min (i.e. ~1.5 m^3/h) for the whole piping system.

The resulting temperatures are shown in Figure 68, with a maximum temperature of 65 °C, reached in proximity of the beam line downstream to the target. The maximum temperature reached in the bulk material other than in this specific area is in the order of 40 °C.

In conclusion, the proximity shielding seems to work in good thermal condition with the proposed piping system reaching a maximum temperature of 65 °C, well below the maximum service temperature of cast iron.

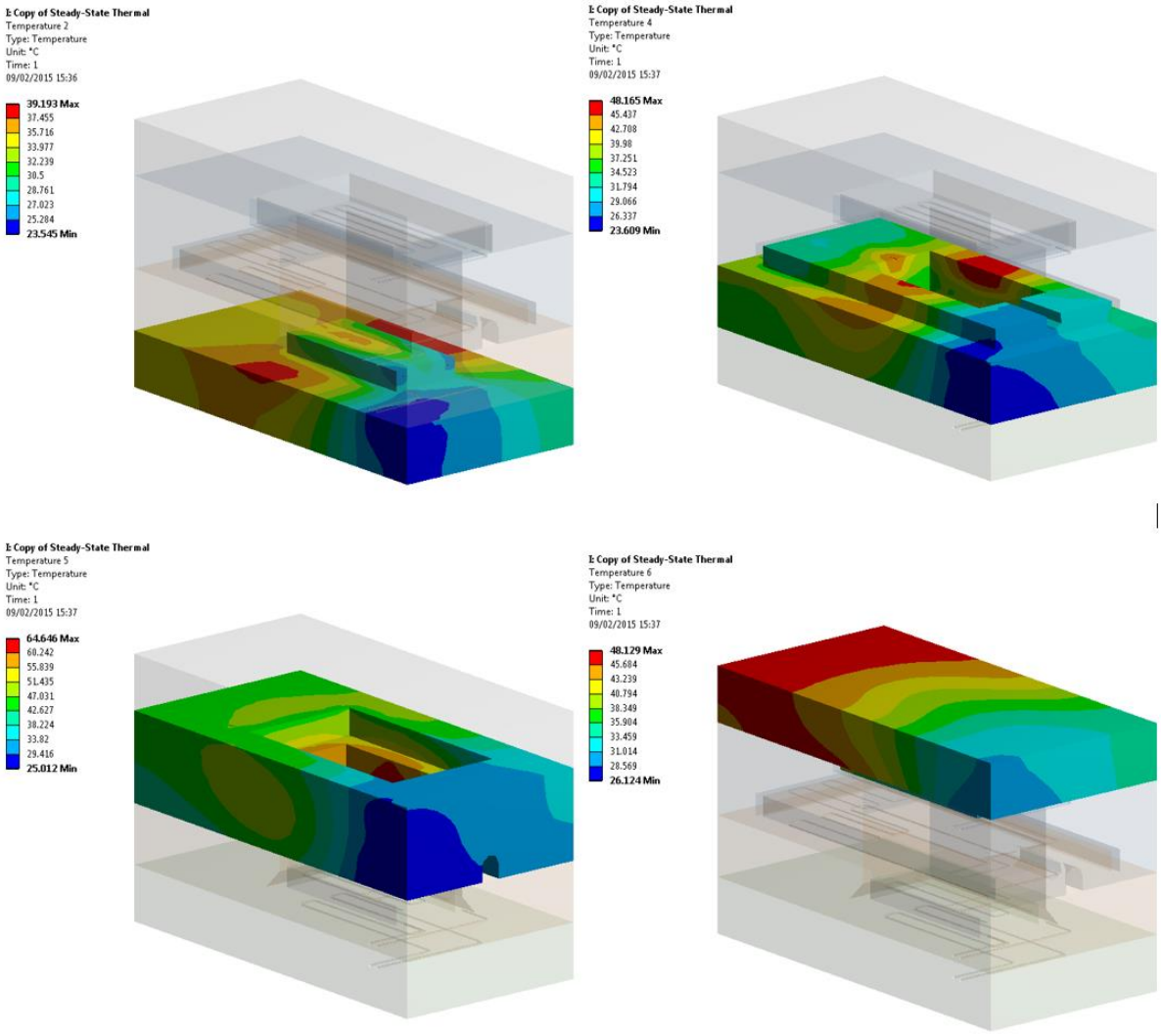

Figure 68: The figure shows the temperature distribution in the various blocks constituting the proximity shielding.

2.2.4.3 Feasibility of the proximity shielding blocks

Two solutions have been investigated for the water-cooled iron shielding blocks.

A full stainless steel (SS) cast solution for the shielding blocks might either involve embedded pipes or cast-in cooling channels. Based on discussions with two companies specialised in SS casting, the present splitting in four blocks results in excessive weight of the individual castings (both companies have limitations for SS castings, the first one is limited to 12 t, the second to 25 t).

A solution with embedded SS pipes, owing a liquidus T in the range of the cast matrix, does not look easily feasible. A solution avoiding embedded tubes is also not straightforward (risk of metallization of the hollow channels, impossible to repair in case).

An alternative solution to explore is a cast iron matrix with embedded stainless steel tubes. This solution is also challenging, due to the little margin between casting T and the solidus/liquidus of the stainless steel: pipes can suffer liquation during casting. Although for cast iron the weight limitations are less severe, the feasibility of a solution with embedded pipes might depend on the mass of the single blocks and would at a first view work better for blocks of limited mass. Indeed, over temperatures are required during casting (T of casting up to 1400 °C) in order to guarantee sufficient fluidity. It is suggested in case to foresee over thickness of the pipe walls. Issues of magnetism should be addressed for the latter solution. A confirmation of the feasibility of the shielding blocks with an embedded piping for the cooled shielding should go through a prototype order. At this stage, we consider the cast iron matrix with embedded stainless steel tubes as the baseline solution.

2.3 Helium loop and water cooling stations

The SHiP target complex will be equipped with two water-cooling systems (for the production target and for the proximity shielding) and a dedicated helium purification and recirculation system for the He-vessel.

Taking into account the beam average power, the design of the various water cooling circuits will need special attention with respect to radiation protection and radiation safety aspects.

The water system will guarantee the heat removal from the target and the shielding. The helium system will also remove the residual heat coming from the shielding structure and will guarantee the inertisation of the volume.

2.3.1 SHiP Target cooling

The primary proton beam will deposit on the target a maximum power of roughly 2.3 MW during the course of the 1 second spill. The supercycle-averaged power will be of about 350 kW. A dedicated pressurised water-cooling circuit will be installed to extract this power.

The water speed on the walls of the target block shall be kept high enough to let the water be far enough from the boiling point. A high water speed will allow a high heat transfer coefficient that will limit the temperature difference between the target walls and the water bulk.

As described in Section 1.2.6 the first preliminary design justifies a water-cooling system managing about 50 l/s (=180 m^3/h). This will generate an average temperature difference of 1.5 K between the inlet and outlet conditions. Special precautions will be taken in order not to generate risks of erosions in the cooling circuit.

An intermediate circuit will divide the primary cooling circuit to the target one. This will avoid the risk of contamination of the primary water of the cooling towers in case of failure of the heat exchanger of the target cooling circuit. For that reason, the lowest reasonable inlet temperature of the cooling circuit will be around 30°C.

2.3.2 Proximity shielding cooling

The interaction between the secondary beam and the shielding structure will generate about 26 kW of heat on the proximity shielding cast iron blocks. A dedicated cooling circuit will be installed in the CV service room to remove this heat.

This system will exchange with the same intermediate circuit that provides cooling power to the target cooling circuit. For the same reasons the inlet temperature will be about 30°C. Allowing a temperature difference of 10 K, a water flow-rate of 1.5 m^3/h shall be guaranteed (see Section 2.2.4.2).

This small system will be installed on the same skid of the target cooling system.

2.3.2.1 Water system estimates

The estimated dimensions of this water-cooling skid for the target and the shielding cooling are about 8 x 5 m^2. The cooling tower will require an additional surface of 3 x 2 m^2 outside of the SHiP target complex. The external area shall also take into account the presence of the pipeworks.

2.3.3 SHiP bunker helium containment and circulation system

The atmosphere of the target bunker vessel shall be controlled to reduce as much as possible the water content and avoid tritium production. A similar installation in Japan adopted the solution to put the target chamber under vacuum before filling it with helium gas. This had a relevant impact on the design of the mechanical structure of the target vessel. The SHiP installation has been designed to work in helium atmosphere starting from air at atmospheric pressure: in agreement with the HSE environmental service requirements and the available technological solutions, it has been decided to design a system able to control the purity of the helium and limit its impurities to 0.1 % of air content. A detailed design available for the CENF facility is available in Ref. [30].

The air-helium replacement process has been designed to be repeated for a maximum of two times per year, following the need to access the inner elements. To reduce the dimensions and cost of the helium system it has been decided to allow about one week to perform the entire process going from a 100% air situation to a 99.9% helium one.

To remove the air from the vessel and replace it with helium two phases will be used, a flushing phase first, followed by a purification step afterwards.

2.3.3.1 Flushing process

During a technical stop or a winter shutdown period, the vessel can be opened to perform operation or maintenance actions on the internal devices, if required. Once this operation will be over, the steel cap of the vessel will be placed again over a rubber gasket to obtain a good air-tightness.

During the first phase of the air-helium replacement process, helium will be injected from the top of the vessel. The difference of density between the two gases allows their stratification; the helium cumulates on the top of the vessel and using a piston effect it

forces the air to escape from the bottom of the vessel, where a dedicated outlet will be installed. When the helium fills the volume, its concentration at the outlet of the vessel starts increasing.

Considering the cost of the helium (about 10 CHF/m^3) and the number of years foreseen for SHiP operation it has not been considered convenient to reach the requested purity level with just a flushing method. A cryogenic purification system has been studied in collaboration with Air Liquide (see Ref. [30]) to reduce the quantity of helium used for each air-helium replacement process.

The air concentration at the outlet of the vessel during the flushing phase will decrease; under a certain level of concentration, the flushing phase will be stopped and a closed cycle of gas mixture purification process shall start. The air quantity threshold shall be defined on technological and economical bases to allow the purification process working efficiently and reduce the overall consumption of gas helium during the flushing phase.

2.3.3.2 Purification process

In order to use cryogenic purification, the air concentration shall be below 25% (above this limit air will liquefy in the cryogenic system). A small margin of 5 K is taken to ensure that no liquefaction will occur in the vessel. Consequently, the maximum air concentration before entering the purification system is about 15%.

When the air content will be reduced to 15% the purification cycle will be activated and the flush of pure helium will be limited to the compensation quantity needed to maintain the pressure of the vessel while the air is removed. The vessel will be kept at about 100 Pa of overpressure to limit the air intakes from the rubber gaskets. The helium gas leaks from the rubber airtight gasket where the vessel cap seats. A continuous consumption of about 1 Nm^3/day of helium is estimated.

The purification system designed by Air Liquide for the CENF project consists in a "simplified purifier system". This system is able to purify the helium to 0.1% of air content. Some additional regeneration/purification cycles can be performed if a much lower purity level is required.

Once the adsorber is saturated, the helium circulation is stopped; the adsorber heated up to ambient temperature and flushed with gas nitrogen. This regeneration process allows the system to be ready for a new purification process again.

The purification process involves about 2 g/s of gas mixture; the gas mixture passes in the purification circuit coping with about 1.5 bar of pressure drop. For this cycle a low flow rate helium compressor at high pressure is required.

Once the purification process is over the control system will open the interlock to the beam and the physics run is allowed. A "safe beam limit" will be defined as to allow operation of the facility.

2.3.3.3 Cooling (and purification) process

The secondary beam interaction with the iron shielding internal to the vessel deposits heat on the shielding structures. The proximity shielding structures are water-cooled but it has been estimated that about 2 kW will be released on the helium atmosphere. The gas helium circulating inside the vessel removes this heat.

The gas helium is compressed by the compressor, and cooled down to about 11 °C using the chilled water circuit. It is injected on the bottom of the inside the vessel where it removes the heat generated by the secondary beam on the iron shield. After having passed through the gaps of the iron shielding the helium is collected and exits from the top of the vessel. The maximum helium temperature at the exit shall be lower than 45°C.

During the experimental run the helium circulates continuously to remove the heat. The air content is continuously measured online and, in case of an increase of the air content above the required threshold, the purification cycle is automatically activated to control impurities.

2.3.3.4 Helium system layout estimate

The compressor and purifier equipment will be delivered in two separated skids. The compressor one has an estimate of dimensions of about 3.5 x 2.0 x 2.5(H) m^2. The purification one has an estimate of dimensions of about 2.5 x 2.0 x 3.8(H) m. They would both be installed in the CV service room lateral to the target bunker.

2.4 Remote handling of target and proximity shielding

According the preliminary study of the SHiP target complex the following design guidelines have been taken in consideration for the design of the handling system.

The overhead travelling crane will handle all the equipment of the target facility: the equipment that will become the most radioactive – production target, proximity shielding and fixed cast iron blocks – will have to be designed in such way to respect the ALARA principle.

The target and the water-cooled proximity-shielding block shall be fully plug-in (for cooling, control, alignment, and handling). For those systems, similar designs exist already at CERN and in some other facility. However, the present facility poses challenges in terms of radiation levels as well as water flow, pressure, precision of positioning: the existing solutions (i.e. the plug-in systems for the LHC collimator) will have to be re-evaluated in order to check their compatibility and their reliability with the expected design.

In order to reach the correct positioning of the different system a series of prepositioning and positioning mechanical guides would have to be implemented in the design.

2.4.1 Design of the facility

In order to optimize the handling in terms of dose taken by the personnel during the overall life of the facility an intermediate level is foreseen in the target pit, in order to minimize the possible direct exposition of the workers in the target hall during the different handling phases.

The design of the shielding surrounding of the target bunker will allow an easy access of the target for all the maintenance tasks. Only part of the shielding would have to be removed when access to the target and proximity shielding will be needed (orange part in Figure 69 and Figure 70). 160 cm thick concrete beams are foreseen to cover the whole area above the target bunker and the intermediate storage zone: as shown in Figure 69, the design is such as to present a small chicane in order to avoid direct streaming of radiation towards the target hall.

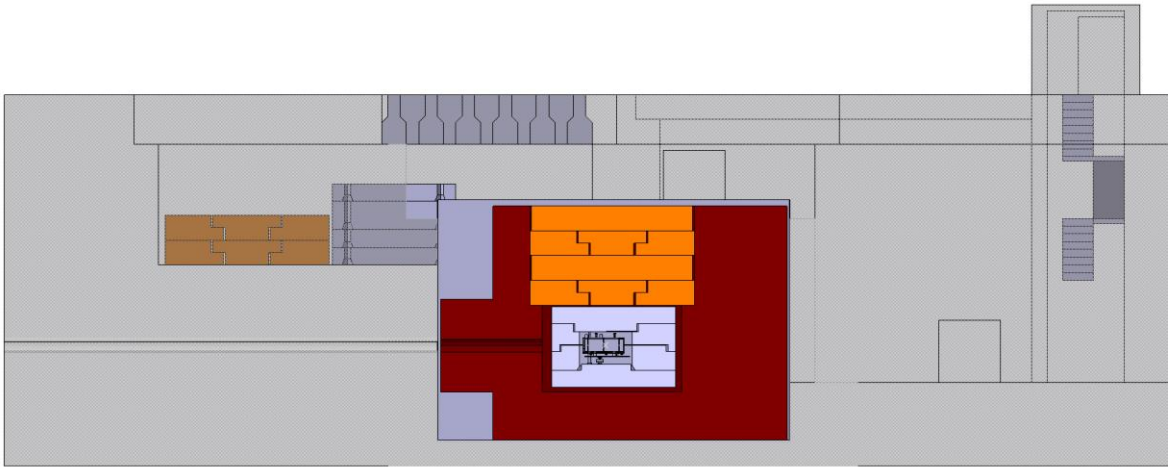

Figure 69: Longitudinal view of the SHiP target complex underground areas.

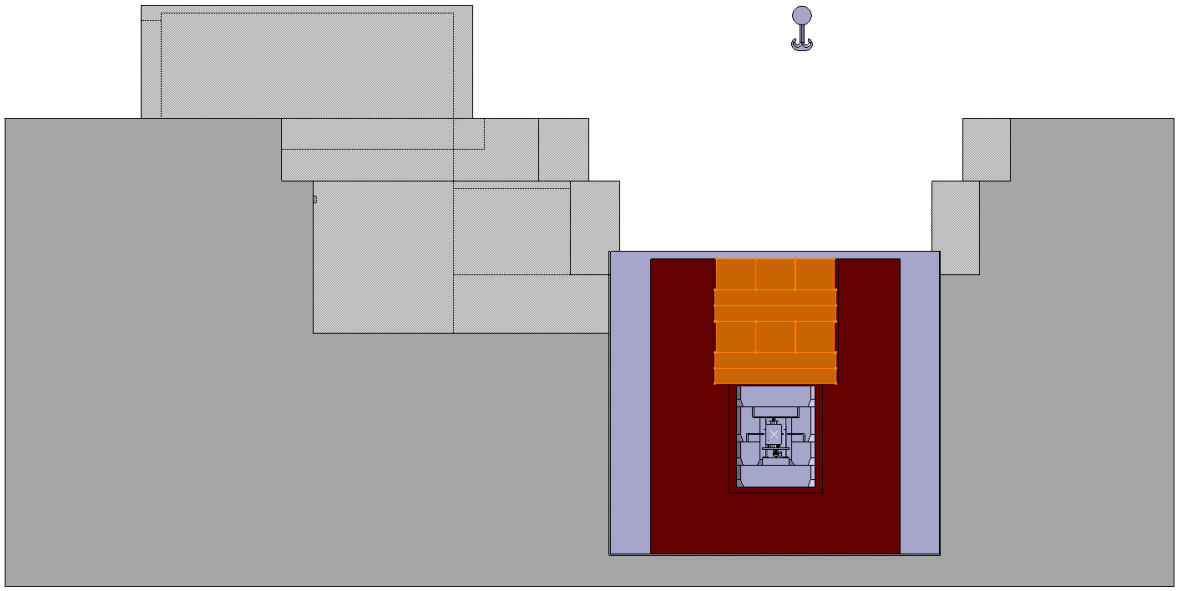

Figure 70: Transversal view of the SHiP target complex underground areas, showing the target bunker, the He-vessel and the intermediate storage zone.

2.4.1.1 Access and service building

The SHiP target hall will have an annex building with three dedicated extensions with the following functions:

- Access for the delivery of the heavy equipment
  - An access SAS will permit the access of an articulated truck in order to get inside of the target hall without breaking the ventilation condition of the main hall (keeping the ΔP condition required according to the ISO17873 norm). This part of the building will be used during installation and during the transfer of a spent target or proximity shielding blocks to storage or to a post mortem analysis in a dedicated hot cell.
- Personnel access
  - The area shall also include a PAD/MAD and a changing room in order to get an access to the main target hall such as at the ISOLDE target area or the 867 radioactive workshop following radioprotection requirements.
- Control room for fully remote operation
  - Considering the significant residual dose rate of the SHiP target equipment (O(Sv/h)), all handling operations in the target hall (movement of shielding blocks and target) will be performed fully remote from a dedicated area in the service building. It will therefore be linked with all the different equipment used for the remote handling operations (cameras, control of overhead crane) and all the communication technology used for that kind of operation. The cubicle of the crane (see Section 2.4.3) will also be installed in this building. A dedicated control

room shall be implemented in order to have a team of at least of 4 people (equipment owner, 2 operators and a radioprotection technician).

In addition to the above-mentioned equipment, the building will also house the radiation protection monitoring control systems, intermediate heat exchangers for the target and shielding cooling unit, the target hall ventilation system as well as ancillary systems such as UPS, control racks for the access and safety systems. The target hall or the service building will also house all the electrical cabinets, control PLCs as well as all the electronics sensitive to radiation that cannot be placed in the underground areas.

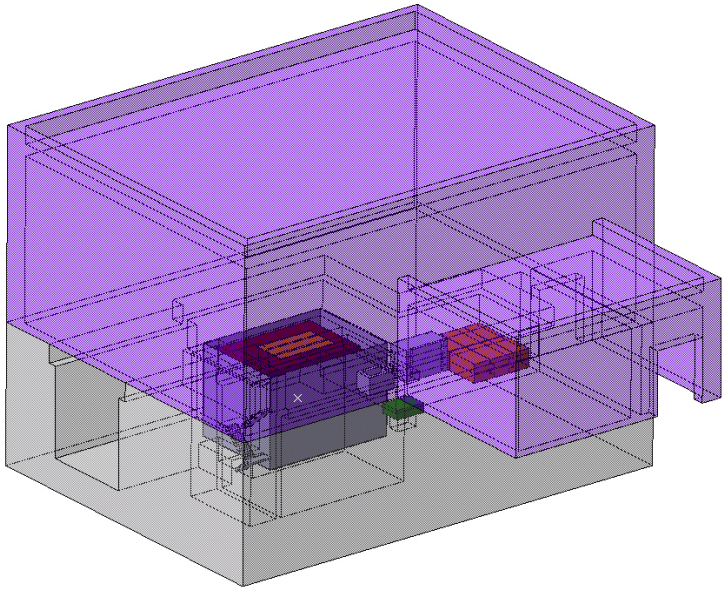

Figure 71: The figure shows an isometric view of the SHiP target complex, showing also the surface building as well as the annex on the right part.

2.4.2 Handling need for the SHiP target facility operation

2.4.2.1 Production target handling

In case of the SHiP production target replacement (due to a break down or to an optimization of the facility), a dedicated storage bunker is foreseen in the storage area (see Figure 57 and Figure 58).

According to the present conceptual design, the following steps should be followed in order to remove the production target from it beam position:

1. Removal of the concrete beams separating the target hall from the top of the target bunker (i.e. the top of the helium vessel);
2. Partial opening of the roof of the helium vessel (storage on the surface of the target hall);
3. Removal of the 4 layers of the iron shielding (orange blocks in Figure 69 and Figure 70) and storage in the intermediate shielding zone;

4. Opening of the top block of the water cooled proximity shielding;
5. Removal of the target;
6. Storage of the target in the dedicated bunker in the intermediate shielding zone;

The target shall be equipped with lifting points for full remote handling (see Figure 72).

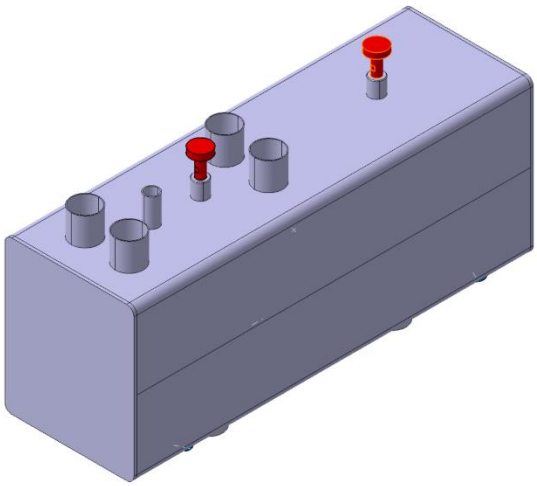

Figure 72: Isometric view of the SHiP target with transport lifting points (red in the figure).

In order to transport the target outside the SHiP target facility (for final storage or to conduct a post-irradiation experiment) a dedicated transport shielded cask compatible with transport standard is foreseen and to be located in the shielding storage area. The shielding thickness of such a transport cask is estimated to be ~26 cm of iron or ~16 cm of Pb [29].

2.4.2.2 Water-cooled proximity shielding

In case of a failure of the water-cooled proximity shielding blocks a dedicated cool down area is foreseen in the facility for the complete shielding assembly. In order to minimize the space and contain the radiation during the cool down period it is foreseen to rebuild the shielding in the storage place as installed.

All those items shall be equipped with lifting points, which would allow full remote handling. The size and shape of the blocks have been optimized with the objective of fitting the crane capacity, in such way as to minimize the number of connections (see Figure 63).

2.4.2.3 Fixed iron and concrete shielding in the target zone

In order to ensure an efficient decommissioning of the SHiP target facility the fixed iron shielding will be equipped with lifting points compatible with full remote connections (such as CERN standard lifting point, or twist lock lifting point).

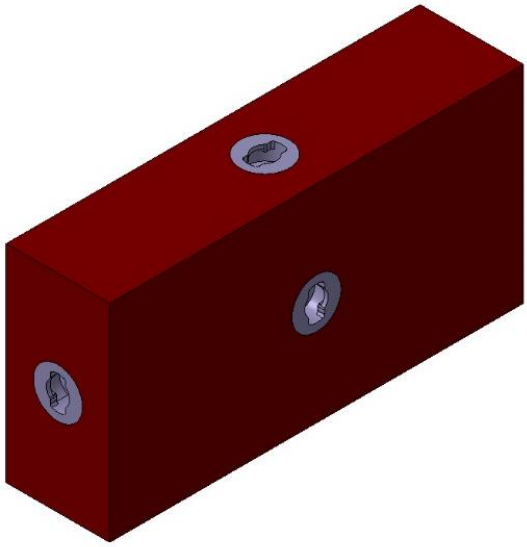

Figure 73: Isometric view of a fixed iron block with dedicated lifting points to allow full remote operation.

The size of the shielding block would have to be optimized in order to minimize the number of operations and would have to be compatible with the radiological conditions and with the overhead crane.

2.4.2.4 Safety

For the handling aspects, experience is drawn from the operational record of similar facilities such as n_TOF target, ISOLDE, North Area TCC2 and HiRadMat. A detailed study of the different possible failure scenarios and their recovery methods during the handling phase shall be performed, including all lifting equipment such as the crane, the lifting spreaders. The study shall include all the associated risks regarding the possible damage of the equipment handled and their surroundings.

2.4.3 Crane design and constraints

A double-girder overhead crane will be used to perform all handling activities in the SHiP target hall and in the area of the muon shield; its 40 tons capacity will guarantee handling of the heaviest and most sensible items such as the target and the bunker iron shielding blocks.

Table 9 summarizes the crane's main parameters.

Table 9: The table summarized the characteristics of the SHiP target complex crane.

Span [m]	28
Capacity [tonnes]	40
Lifting speed [m/min]	0.25 – 5

Cross travel speed [m/min]		0.4 - 8
Long travel speed [m/min]		0.4 - 8
Maximum lifting / braking acceleration [m/s^2]		1
Hook size (according to DIN 15402)		20
FEM (European Federation of Material Handling) classification	Structures	A4
	Mechanisms	M4

The conceptual design considers that the crane will not be used frequently during its whole lifetime and not always at its full capacity (light-medium duty crane).

The hoist shall be conceived so that the hook will be lifted or lowered without any horizontal drift (pure vertical lifting); a motorized hook will allow rotation of the items during handling.

Electrical motors shall be driven by frequency converters to obtain smooth accelerations thus limiting the stress in the components; the crane will have a precision of positioning in the three directions of 1 mm.

The crane will be equipped with a positioning system in order to track the position of the different equipment during the different steps of the installation or maintenance in the SHiP target complex.

By means of PLCs it will be possible to define multiple areas where access of the hook is forbidden thus avoiding risk of crash with sensible objects.

Figure 74 shows the operating area covered by the hook inside the target hall.

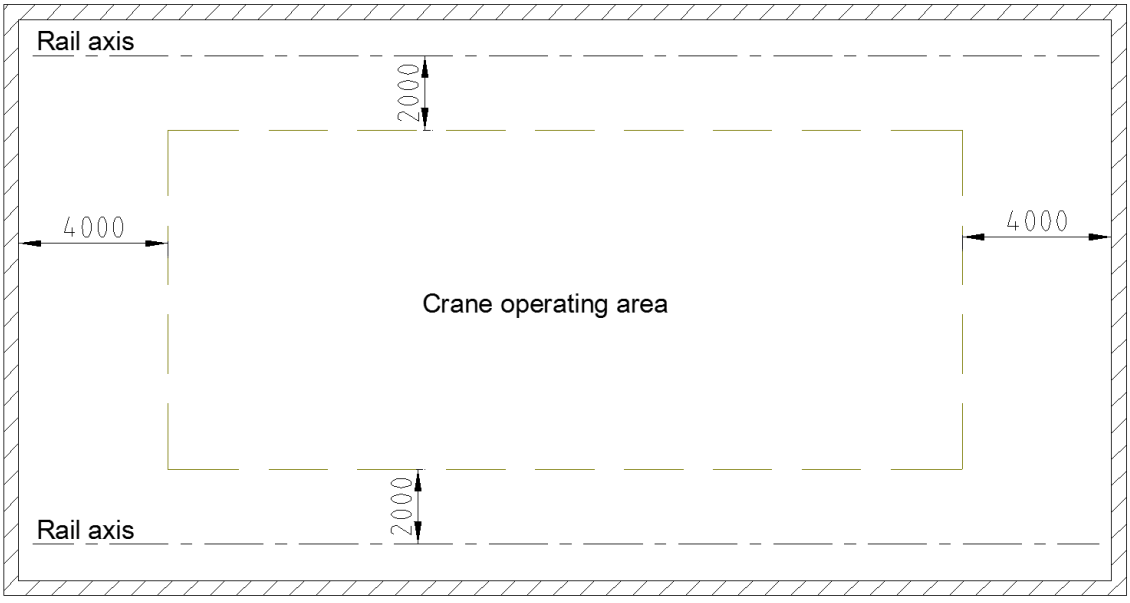

Figure 74: SHiP target area crane operating area.

The minimum distance between the hook and the rail axis (hook side approach) will be bigger than what can be usually be obtained with a standard crane of the same capacity, the reason being a more complex hoist (see Figure 75) and therefore an overall increase of the crane size. Consequently, the crane supporting frames shall be designed to guarantee the requested operating area.

2.4.3.1 Additional features for operation in a radioactive environment

In case of target maintenance or replacement, during or at the end of the facility lifetime, the crane will handle highly radio-activated objects; to reduce people exposure to radiation, the following features will therefore be included in the crane design.

1. Remote operability

   Personnel will operate the crane through joysticks installed on a remote desk in a control room away from the target hall; cameras will provide images of the whole operating area as well as close-ups on the interactions between the hook, the spreader and the objects being handled.

   The crane will be equipped with appropriate instruments (lasers, encoders) giving the possibility to measure the position of the hook along the three directions and the rotation of the hook.

2. Redundancy

   In case of breakdown of a crane component, it will still be possible to lay down the load and move the crane in a safe position without personnel intervention. This will be possible thanks to the following technical solutions:

   - All wheels will be motorized so that, in case of fault of any of the four motors or gearboxes, the other motors will still be able to move the crane;
   - Double-hoist: lifting of the hook will be assured by simultaneous rotation of two identical hoists (see Figure 75);

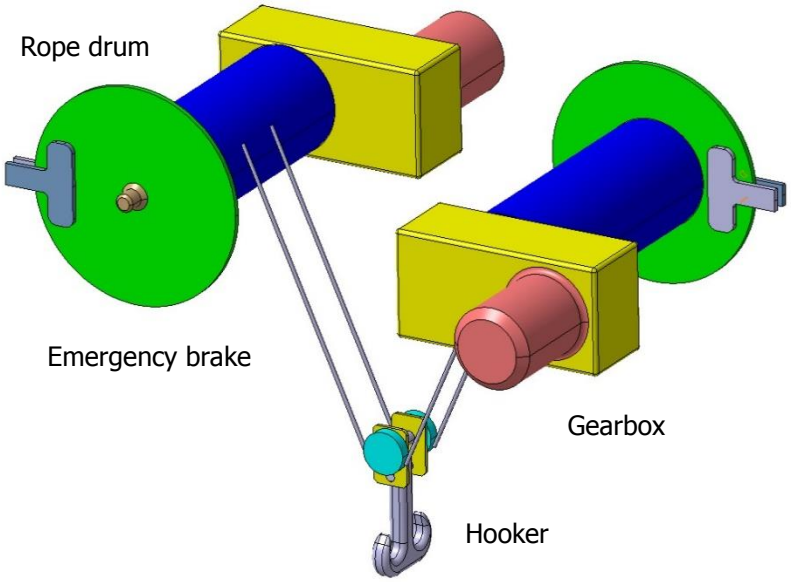

Figure 75: The figure shows the SHiP target complex crane double-hoist configuration.

- In case of mechanical failure of any component, drop of the load is avoided by the intervention of the emergency brake. Operations can nevertheless be completed with the second hoist.
- Table 10 shows an assessment of the possible mechanical faults that could occur to the hoist and their consequences on the operations: in any case, the double-hoist configuration will guarantee the possibility to lay down the load and complete the operation without need of intervention in the breakdown position.
- Electrical cubicles will be located off of the crane so that in case of fault of components, no access of personnel in the hall will be required, reducing the exposure in case handling of highly radioactive objects will be required;
- Spare wires will be left inside the control and powering cables so that intervention time in case of defect on wiring will be limited.

Table 10: The table provides an assessment of hoist faults.

Fault	Probability	Effect	Intervention		Duration of intervention on crane *
			Breakdown position	Parking zone	
Main motor - short-circuit between phases	Medium	The handling operation is completed by the second hoist at half speed.	-	motor replacement	4 hours
Gearbox – fracture of shaft, gear or key	Very low (1 case at CERN due to intensive use at a load exceeding capacity)	Drop of load is avoided by means of an emergency brake; load slips ~40 cm before being stopped with a deceleration of 1 m/s^2. The operation is completed by the second hoist at half speed.	-	gearbox repair	4 days
Gearbox/ Rope drum– seized bearing	Very low (never happened at CERN)	One hoist is stuck; handling operation completed by the second hoist at half speed.	-	gearbox repair	4 days
Service brake	Low	The drop of the load is avoided by emergency brake; load slips ~40 cm before being stopped with a deceleration of 1 m/s^2. The handling operation is completed by the second hoist at half speed.	-	brake replacement	4 hours
Rope drum - shaft	Very low (1 case in HE history due to assembly fault)	The drop of load is avoided by emergency brake; load slips ~40 cm before being stopped with a deceleration of 1 m/s^2. The handling operation is completed by the second hoist at half speed.	-	rope drum repair	5 days
Rope	Low	The entire load is sustained by the second rope (swaying); the load can be safely laid on the ground	-	rope replacement	1 day

2.4.3.2 Remote handling practices

More sophisticated lifting equipment, provision of camera systems and careful design of loads and the infrastructure shall be taken into account at the design stage to allow remote operation of cranes.

Guidelines on remote handling will be taken from the ITER Remote Handling Code of Practice (RHCoP) which was made available to CERN under licence from the ITER Organisation.

Some of the main RHCoP recommendations are:

- The final positioning of parts follows a purely vertical trajectory for easy lowering by the crane;
- Staged guidance of the blocks as they are lowered into position: to guarantee a correct positioning during remote handling, the six degrees of freedom of each item are progressively constrained during their lowering;
- Use of cone-type surfaces to guide the object positioning (for the SHiP production target and the proximity shielding blocks);
- Use of standardized attachment points.

3. Conclusions and R&D activities

The documents present the conceptual design of the SHiP production target as well as of the SHiP target complex.

The study shows that the SHiP production target – according to the present knowledge – is feasible, despite several unknowns and critical issues associated with the evolution of material properties with radiation and to the high thermal fatigue expected for the SHiP operational scenarios.

The SHiP target complex design takes advantage of the studies performed for the CENF Neutrino Facility and adapts it to fit to a different production target design and a different physics reach. It further includes the radiation protection considerations in order to respect the applicable CERN radiation protection legislation regarding doses to personnel as well as the environmental impact. The results of the radiological assessment for the design of the SHiP facility are presented in [29].

Following the concepts developed in the present design, some critical R&D items have been identified; those shall be addressed in order to proceed towards a technical design of the whole installation. The program should include:

1. A detailed analysis of the assembly, configuration and fabricability of the cladded refractory metal blocks in collaboration with specialized companies. Prototypes shall be foreseen to analyse different production methods and the cladding/coating resistance to corrosion/erosion effects;
2. Material irradiation R&D on the refractory metals including TZM, pure Mo, W and W-TiC, followed by detailed PIE and mechanical testing;
3. Study the feasibility of water-cooled cast iron blocks with embedded stainless steel pipes;
4. Investigate and develop, together with specialized companies, fully metal, high flow rate-compatible and high pressure plugin systems for remote and fast connection/disconnection of water pipes;
5. Develop the design of an helium gas cooled SHiP production target, in collaboration with external companies for what concerns the circulation, cooling and purification loop;

4. Annex I: SHiP target drawings

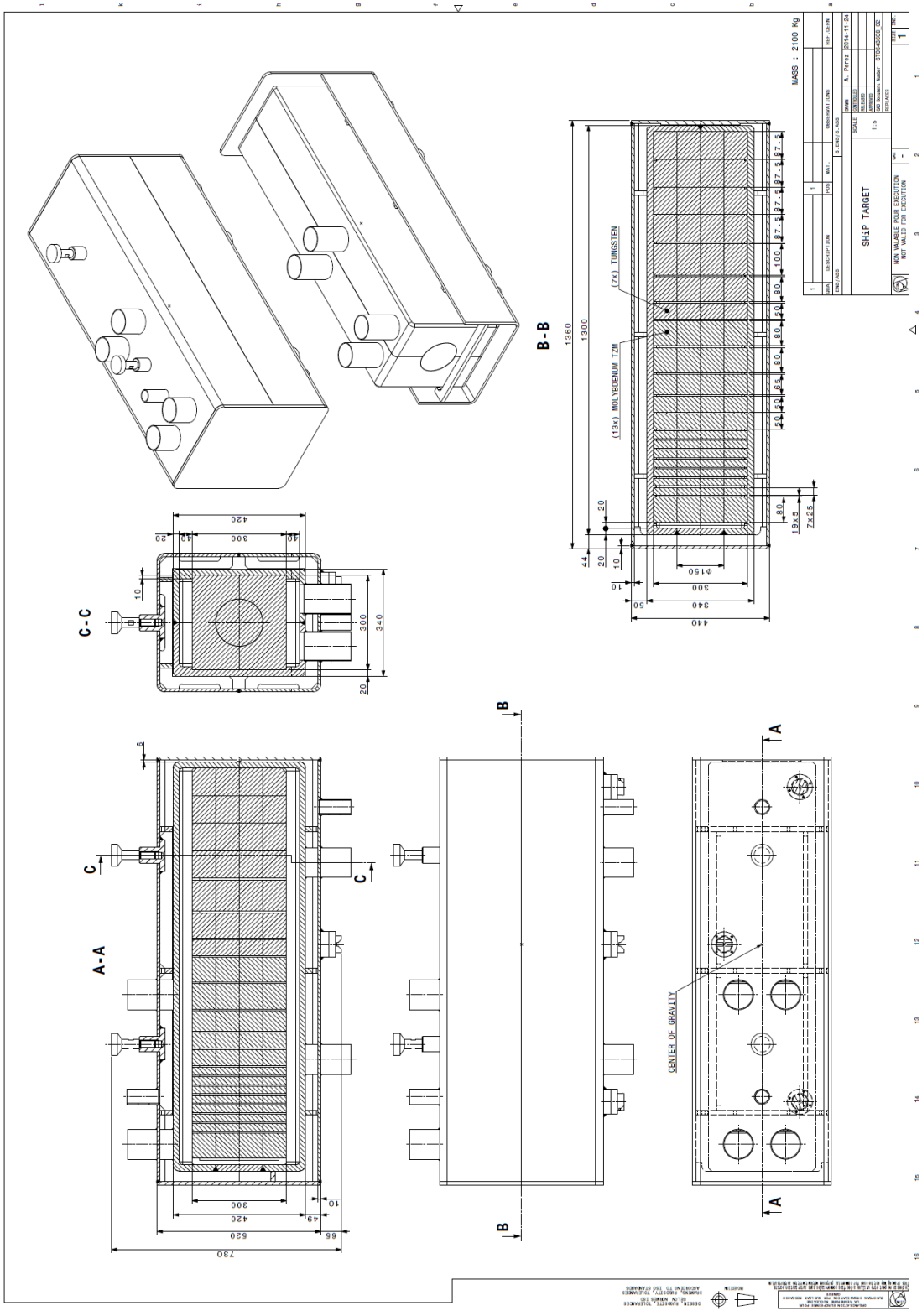

Figure 76: Isometric and cross-sectional views of the conceptual design of the SHiP production target (ST0643608_02).

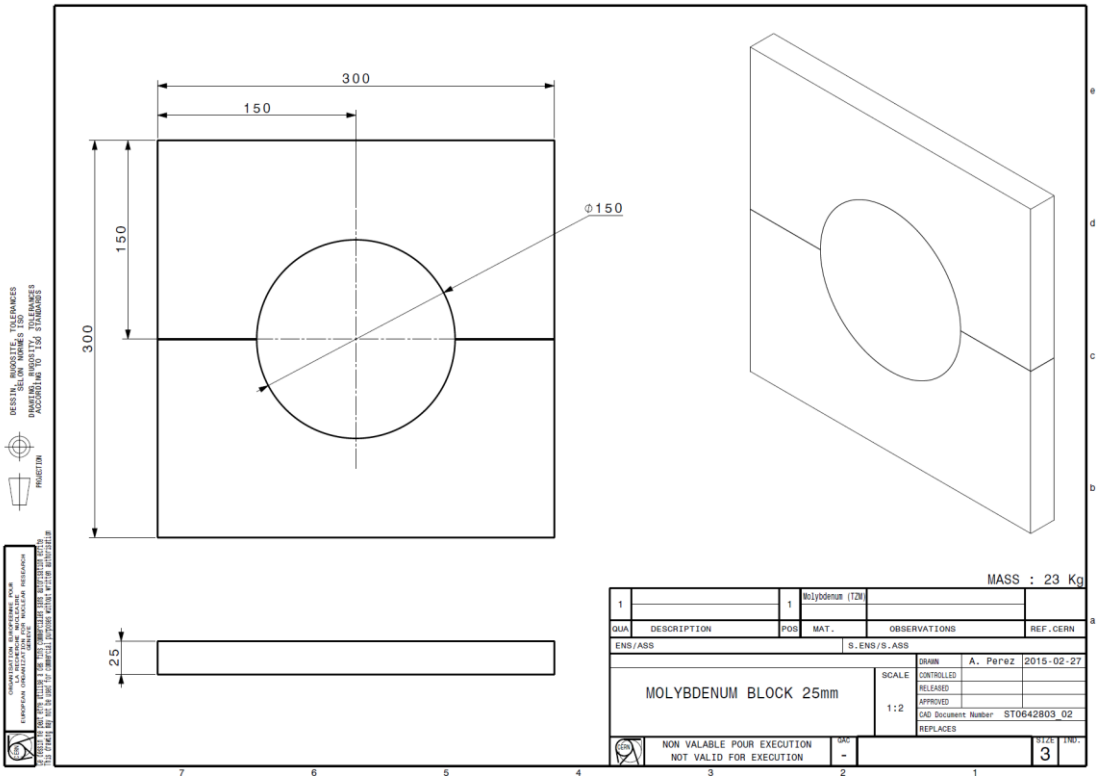

Figure 77: Isometric and cross-sectional view of the 25 mm TZM target block (ST0642803_02).

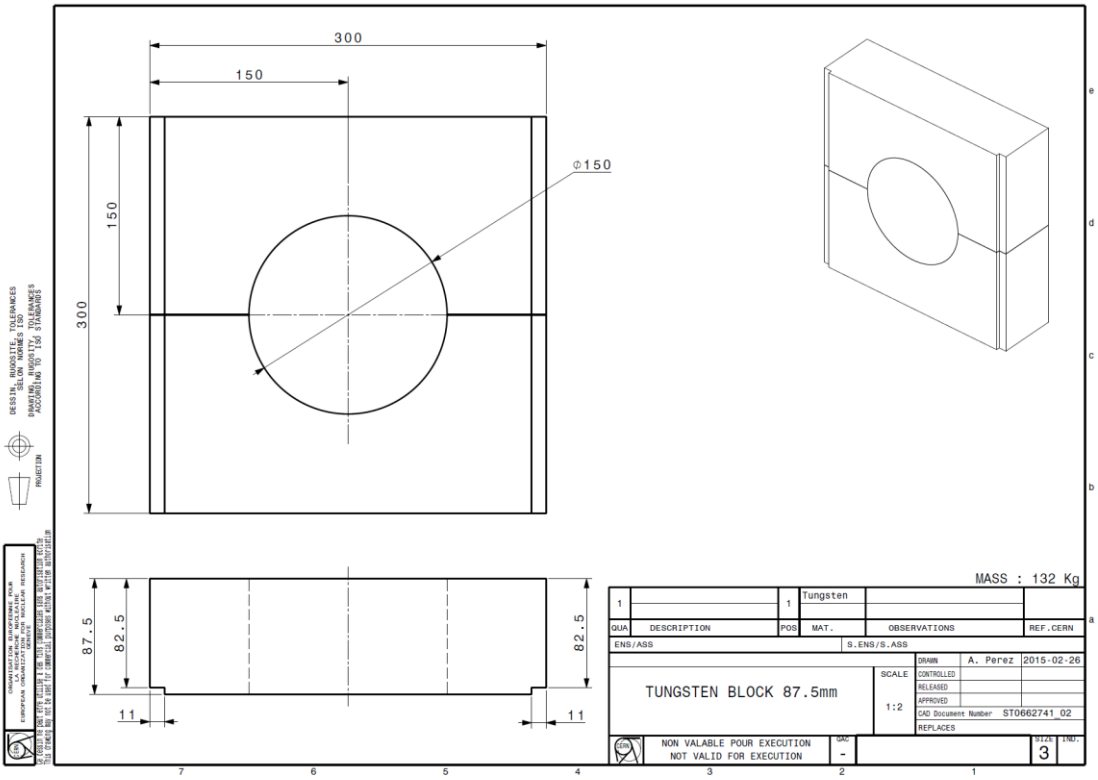

Figure 78: Isometric and cross-sectional view of the 87.5 mm long pure tungsten block (ST0662741_02).

5. Annex II: SHiP Target Complex drawings

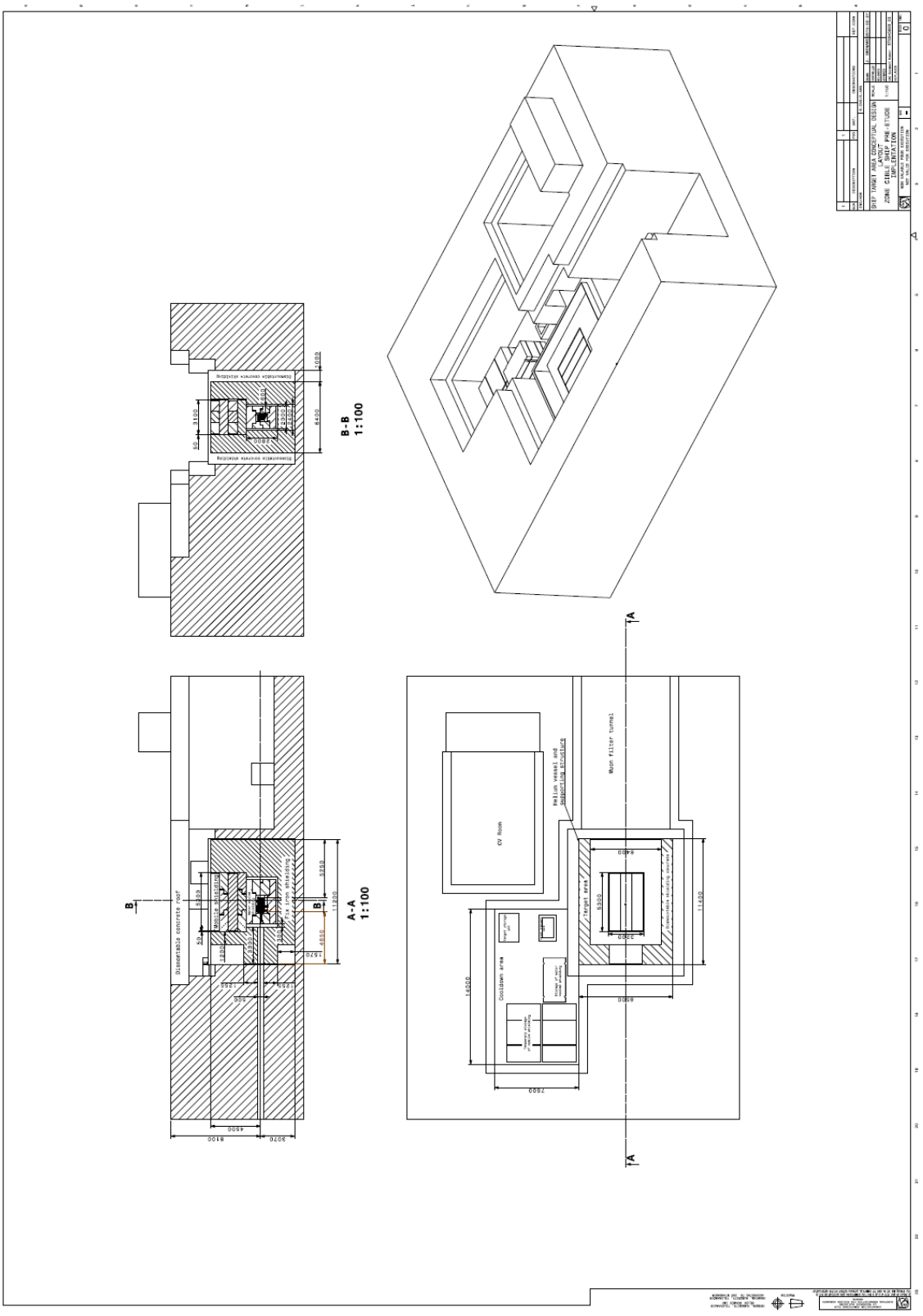

Figure 79: Isometric and cross-sectional views of the SHiP target complex (ST0643908_03).

6. Annex III: SHiP Target Complex equipment cost and manpower estimate

Table 11 presents an updated table with a cost estimate for various equipment of the SHiP target station, including a summary of the staff (in FTE) required as well as with fellows. Fellows are listed for information, but their cost is included in the first column.

The table excludes the contribution for general infrastructure equipment such as the crane and handling systems, access & safety systems, electrical infrastructure, radiation protection monitors, cooling and ventilation plants, which are assumed to be costed elsewhere.

Table 11: Cost and manpower estimate for the SHiP target and target complex.

SHiP Target Complex cost and manpower estimate

	MCHF	***Staff (FTE)***	***Fellows (MCHF)***
Target unit (+spare)	***4.6***	***35***	***0.6***
Iron shielding (active + passive)	***12.6***		***0.6***
Helium enclosure of target bunker[3]	***2.7***		***0.4***
Concrete shielding[4]	***1.2***		***-***
Controls	***0.9***		***0.4***
Prototypes, testing and R&D	***1.5***		***0.6***
Integration & design support	***0.5***		***-***
Total	***24.0***	***35***	***2.6***

[3] Includes helium vessel structure and He circulation and purification system.

[4] Includes all mobile concrete shielding blocks for the target bunker and the concrete beams separating the underground areas from the target hall.

7. Acknowledgments

MC would like to warmly thank the T2K team at J-PARC – and in particular Y. Yamada, T. Ishida, Y. Fujii, M. Tada, T. Sekiguchi, T. Nakadaira and Y. Oyama – for all the technical details associated with the design of the T2K target station as well as for the hospitality during our visits. The design of the SHiP target station has profited from those discussions.

A special thanks to A. Karatepe, A. Rasmussen and A.-M. Lambert for the proofreading.

8. References

[1] The SHiP Collaboration, "A Facility to Search for Hidden Particles (SHiP) at the SPS," CERN (SHiP-TP-2015) - CERN-SPSC-2015-016 - SPSC-P-350, Geneva, 2015.

[2] G. Arduini et al., "The SPS beam parameters, the operational cycle and proton sharing with the SHiP facility," CERN - EDMS 1498984 (SHiP-TP-2015-A2), Geneva, 2015.

[3] F. Bergsma, "Prompt lepton production in a proton beam dump experiment," CERN (http://cds.cern.ch/record/205527/files/CM-P00068733.pdf?version=1), Geneva, 1990.

[4] G. Arduini, M. Calviani, K. Cornelis, L. Gatignon, B. Goddard, A. Golutvin, R. Jacobsson, J. Osborne, S. Roesler, T. Ruf, H. Vincke, H. Vincke, "A new Experiment to Search for Hidden Particles (SHiP) at the SPS North Area - Preliminary Project and Cost Estimate," CERN - EDMS 1369559 - EN-DH-2014-007 (SHiP-TP-2015-A1), Geneva, 2014.

[5] B. Goddard, M. Fraser, "Extraction and beam transfer for the SHiP facility," CERN - EDMS 1495859 (SHiP-TP-2015-A3), Geneva, 2015.

[6] A. Ferrari, P.R. Sala, A. Fasso' and J. Ranft, "FLUKA: a multi-particle transport code," CERN 2005-10 (2005), INFN/TC_05/11, SLAC-R-773, 2005.

[7] T.T. Böhlen, F. Cerutti, M.P.W. Chin, A. Fassò, A. Ferrari, P.G. Ortega, A. Mairani, P.R. Sala, G. Smirnov and V. Vlachoudis, "The FLUKA Code: Developments and Challenges for High Energy and Medical Applications," *Nuclear Data Sheets,* no. 120, pp. 211-214, 2014.

[8] M.R. Gilbert, S.L. Dudarev, S. Zheng, L.W. Packer and J.-Ch. Sublet, "An integrated model for materials in a fusion power plant: transmutation, gas production and helium embrittlement under neutron irradiation," *Nucl. Fusion,* vol. 52, p. 083019, 2012.

[9] "Proposal to Search for Heavy Neutral Leptons at the SPS," CERN-SPSC-2013-024, SPSC-EOI-010, arXiv:1310.1762, 2013.

[10] CERN Safety Code D 2 Rev. 2, "Safety code for pressure vessels and pressurized pipelines," CERN (https://edms.cern.ch/document/110434/1), Geneva, 1998.

[11] J. Galambos et al., "High power beam dump and target / Accelerator interface procedures," in *AccApp2013*, Bruges, Belgium, 2013.

[12] T. J. Shea et al., "Status of beam imaging developments for the SNS target," in *DIPAC09*, Basel, Switzerland, 2009.

[13] C. Bal et al., "A large scintillating screen for the LHC dump line," in *DIPAC07 - CERN-AB-2007-023 BI*, Geneva, Switzerland, 2007.

[14] ASM handbook, 9th edition, Metals Park, Ohio: American Society for Metals, 1980.

[15] "Molybdenum, Materials Properties and Applications," Plansee, Reutte (A) .

[16] Goynin, I. V. et al., "Effects of neutron irradiation on properties of refractory metals," *Journal of Nuclear Materials,* no. 191-194, pp. 421-425, 1992.

[17] H.-J. Shi, C. Korn, G. Pluvinage, "High temperature isothermal and thermomechanical fatigue on molybdenum-based alloy," *Materials Science and Engineering,* vol. A247, pp. 180-186, 1988.

[18] J. M. Steichen, "Tensile properties of neutron irradiated TZM and tungsten," *Journal of Nuclear Materials,* vol. 60, pp. 13-19, 1976.

[19] H. H. Smith and D. J. Michel, "The effect of irradiation on the fatigue and flow behavior of TZM alloy," *Journal of Nuclear Materials,* vol. 66, pp. 125-142, 1977.

[20] G. Pintsuk, "Tungsten as a plasma-facing material," in *Comprehensive Nuclear Materials*, Elsevier, Ed., Amsterdam, Netherlands: Elsevier, 2012, pp. 551-581.

[21] V. Barabash, G. Federici, R. Matera, A. R. Raffray, *Phys. Scripta,* vol. T81, pp. 74-83, 1999.

[22] M. Shibui, J. Ohmori and Y. Sawada, "Thermal shock test of tungsten by H+- beam bombardment," *Fusion Engineering and Design,* vol. 5, pp. 197-203, 1987.

[23] "Wolfram-Tungsten- Tungstene," Plansee, Reutte (A).

[24] V. Barabash, M. Akiba, I. Mazul, M. Ulrickson, G. J. Vieider, *Nucl. Mater.,* Vols. 233-237, pp. 233-237, 718-723, 1996.

[25] H. Kurishita, S. Kobayashi, K. Nakai, H. Arakawa, S. Matsuo, T. Takida, K. Takebe, M. Kawai, "Current status of ultra-fine grained W-TiC development for use in irradiation environments," vol. T128, pp. 76-80, 2007.

[26] ISO Standard, "Nuclear facilities -- Criteria for the design and operation of ventilation systems for nuclear installations other than nuclear reactors," ISO (also available at http://cds.cern.ch/record/1035354?ln=en), 2004.

[27] D. Forkel-Wirth, A. Henriques, for the Ventilation Working Group, "Ventilation Working Group Report," CERN EDMS 1226988, Geneva, 2014.

[28] J. Osborne, M. Manfredi, "Civil engineering for the SHiP facility," CERN - EDMS 1499253 (SHiP-TP-2015-A6), Geneva, 2015.

[29] C. Strabel, H. Vincke, "Radiation protection studies for the SHiP facility," CERN - EDMS 1490910 (SHiP-TP-2015-A5), Geneva, 2015.

[30] M. Battistin, M. Calviani, "Air Liquide CENF Helium system design study," 2014. [Online]. Available: https://edms.cern.ch/document/1484536/1.

9. List of figures

10. List of tables